Utrecht University

Masterthesis

Effects of nanoconfinement on the ion conduction properties of solid state Li-based electrolytes

Written by:
Matt Peerlings

Supervised by:
Laura de Kort, M.Sc.
Dr. Peter Ngene

November 2018 - January 2020

Inorganic Chemistry and Catalysis
Debye Institute for Nanomaterials Science
Utrecht University
The Netherlands

Abstract for laymen

Lithium-ion batteries have many applications, including mobile phones and electric vehicles. They consist of a positive and negative electrode, separated by an electrolyte. During charging and discharging lithium ions travel through this electrolyte, which currently contains an organic liquid. However, this organic liquid is flammable and causes safety issues. Replacing it with a solid electrolyte will improve the safety of lithium-ion batteries, but the lithium ions typically cannot travel through a solid as fast as through a liquid. In this work, we investigate a method called melt infiltration to improve the mobility of lithium ions in two solid electrolytes, $LiNO_3$ and $LiNH_2$. With this method, the solid is first molten into a porous material, after which the mixture is cooled down. This results in the formation of a new solid structure in which the electrolyte and porous material are in close contact. We demonstrate that this method is successful for both $LiNO_3$ and $LiNH_2$, two very different electrolytes, using a wide variety of porous materials. Therefore, melt infiltration is a suitable method for the improvement of solid electrolytes for safer lithium-ion batteries.

Abstract

Lithium-ion batteries are widely applied in many devices, ranging from mobile phones and electric vehicles to sustainable energy storage. However, they suffer from safety issues and limited energy densities. These features can be improved when the liquid electrolyte is replaced by a solid one. One of the problems that has to be overcome, is that many solid electrolytes suffer from low Li^+ ionic conductivities. Nanoconfinement via melt infiltration is an effective and straightforward method for increasing the Li^+ ionic conductivity of $LiBH_4$, but its effect on other lithium salts has not yet been examined. In this work, the effects of nanoconfinement on the ion conduction properties of $LiNH_2$ and $LiNO_3$ are investigated. This is done by infiltration in a wide range of porous metal oxide scaffolds. The resulting nanocomposites were characterized in terms of pore filling and infiltrate stability with DRIFTS, DSC and XRD, which demonstrated that the interaction of the lithium salts with the scaffold surfaces are key for successful melt infiltrations. These interactions are affected by the chemical nature of the scaffolds, including the presence of surface groups and acid sites, as determined with pyridine FT-IR and NH_3-TPD. By tuning these interface interactions, substantial conductivity increases of more than a factor 1000 were obtained upon measuring the nanocomposite conductivities with EIS. As such, this work demonstrates that melt infiltration is a widely applicable and well-suited method for improving the ionic conductivity of solid electrolytes for all-solid-state battery applications.

Contents

Contents

List of abbreviations

APTES	(3-Aminopropyl)triethoxysilane
ASSB	All-solid-state battery
BAS	Brønsted acid sites
BET	Brunauer, Emmett and Teller
BJH	Barrett, Joyner, and Halenda
BM	Ball milling
CA	Chronoamperometry
CBMM	Companhia Brasileira de Metalurgia e Mineração
CTAB	Hexadecyl trimethyl ammonium bromide
CV	Cyclic voltammetry
DRIFTS	Diffuse reflectance infrared fourier transform spectroscopy
DSC	Differential scanning calorimetry
EIS	Electrochemical impedance spectroscopy
FT-IR	Fourier-transform infrared spectroscopy
FWHM	Full width at half maximum
HT phase	High temperature phase
LAS	Lewis acid sites
LIB	Lithium-ion battery
LT phase	Low temperature phase
MCM-41	Mobil Composition of Matter No. 41
MI	Melt infiltration
NC	Nanoconfinement
NMR	Nuclear magnetic resonance
PF	Pore filling
PSD	Pore size distribution
PZC	Point of zero charge
RT	Room temperature
SBA-15	Santa Barbara Amorphous-15
SSE	Solid-state electrolyte
STP	Standard temperature and pressure
TCD	Thermal conductivity detector
TEOS	Tetraethyl orthosilicate
TMAOH	Tetramethyl ammonium hydroxide
TPD	Temperature programmed desorption
XRD	X-ray diffraction

List of Figures

List of Tables

1   Introduction

Conventional Li-ion batteries

The transition from fossil fuels to renewable energy resources is one of the greatest challenges that our society currently faces. Due to the intermittent nature of renewable energy resources like solar and wind energy, it is required that this energy can be stored efficiently and on large scales. Currently, several methods are employed for energy storage, all with their own advantages and limitations. One of the most efficient and reliable energy storage solutions are rechargeable lithium-ion batteries, which are predicted to play an important role in energy storage in the future.[1]

Rechargeable lithium-ion batteries are not only vital for energy storage in the future. They are already used in numerous other applications, including portable devices like smart phones, as well as laptops and electric vehicles. To acknowledge the large impact of lithium-ion batteries on modern society, John B. Goodenough, M. Stanley Whittingham and Akira Yoshino have even been awarded the Nobel Prize for Chemistry 2019 for their contributions to the development of these excellent storage devices.[2]

The current lithium-ion batteries are made of an anode and cathode component, which are separated by an electrolyte, as shown schematically in figure 1A. The electrolyte facilitates Li^+ ionic transport during charging and discharging cycles, whereas electrons travel through an external circuit where they deliver work. The electrolyte currently used contains an organic liquid, which has a high Li^+ ionic conductivity and high contact area with both electrodes, minimizing resistances and energy losses in the battery.[3]

The organic liquid electrolyte however has several drawbacks that affect the battery performance. First of all, it is flammable and thermally unstable, which can cause mobile phones to burst into flames or lead to safety issues when extinguishing fires in electric vehicles. More safety issues arise due to possible leakage problems and formation of lithium dendrites, which can grow during battery cycling and penetrate into the electrolyte. When they come into contact with both electrodes, short-circuits will occur, causing a decrease in battery lifetime and capacity loss, not to mention serious safety hazards. Another drawback of the current organic liquid-containing electrolytes is that they are unstable in combination with metallic Li, requiring the intercalation of Li in graphite at the anode. This decreases both the volumetric and gravimetric energy
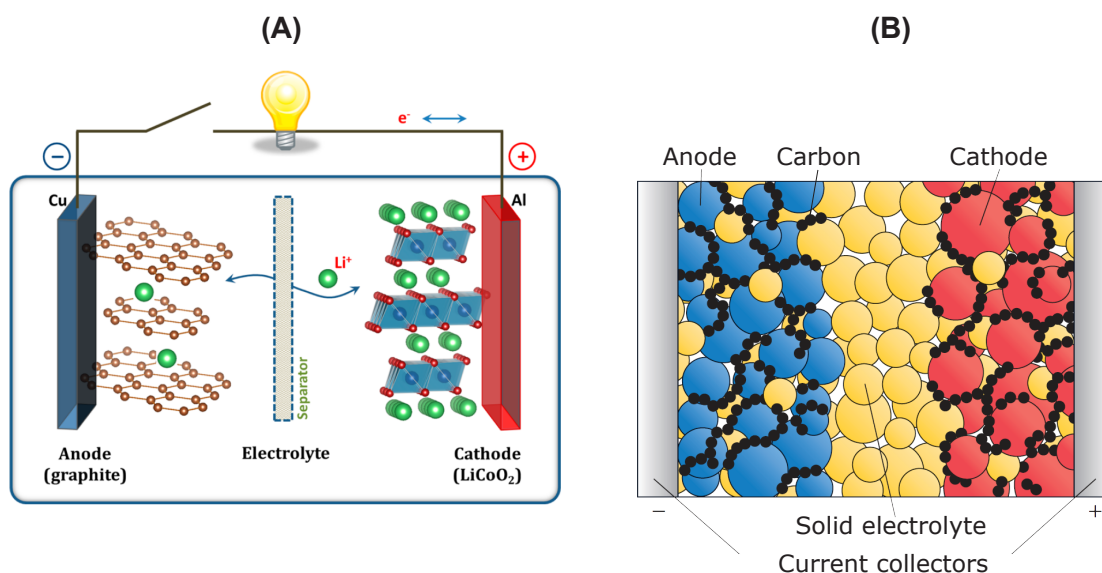
Figure 1: (A) Schematic of the conventional lithium-ion battery, containing an anode with metallic lithium intercalated in graphite, a cathode with lithium ions chemically intercalated in cobalt oxide ($LiCoO_2$) and an electrolyte, typically containing an organic liquid. Image taken from Goodenough and Park [3]. (B) Schematic of an all-solid state battery, containing a solid electrolyte. Black dots represent carbon, which is added to improve electric contact between the electrolyte and the anode and cathode components. Reproduced from Hu [4].

density of the battery.[5–9] A solution for improvement of the safety and energy density of lithium-ion batteries is to replace the organic liquid electrolyte by a solid one.[4,6,10,11]

Solid-state electrolytes

The use of solid-state electrolytes as shown in figure 1B is expected to overcome many of the problems associated with the current liquid electrolytes. They are less flammable, have higher mechanical and thermal stability, and no leakage is possible. This significantly reduces the safety risks associated with the current batteries.[6,10] Furthermore, the formation of lithium dendrites is suppressed, allowing the space between the electrodes and the risk of short-circuits to be reduced.[4] Moreover, most solid electrolytes do not react with metallic lithium, allowing its use as an anode material and removing the need for intercalation in graphite. Lastly, all-solid-state batteries can be stacked in a more compact way. These characteristics all contribute to a reduction in battery weight and volume, allowing higher energy densities to be obtained.[4,6,9,10]

Even though the implementation of solid electrolytes offers many advantages over the use of liquid electrolytes, all-solid-state batteries are not yet applied. Two issues are the main cause for this. The first is related to the interface between the electrolyte and the electrodes. Since it is difficult to establish a high contact area between two solids, high interfacial resistances occur, causing energy losses. The second is related to the mobility of Li^+ ions through the electrolyte, which is often lower in solid electrolytes. To overcome these issues, solid materials with sufficiently high Li^+ ionic conductivity at room temperature are required. Furthermore, this material should be compatible with metallic lithium or other high energy density electodes, have negligible electronic conductivity and be stable over a wide electrochemical potential window.[4,6–11]

A wide variety of solid-state ion conductors have been investigated for implementation in all-solid-state batteries, including sulfide, oxide and hydride materials. Each of these materials have their own advantages and disadvantages.[8,9,12,13] Complex hydrides are a relatively new class of ion conductors, previously investigated mainly for hydrogen storage purposes.[14] They generally consist of a metal cation (Li^+ or Na^+) and a complex anion composed of a central atom coordinated by hydrogen atoms (BH_4^- or NH_2^-). Up until now, research has been performed mainly on the complex hydride $LiBH_4$, a soft and compressible material which is not very conductive at room temperature, but becomes conductive after a phase transition at 110℃.[15,16] For this compound, a strong increase in conductivity was found after nanoconfinement by using melt infiltration.[6,17–19]

Aim of this research

While current research has focussed mainly on $LiBH_4$, little is known on the impact of nanoconfinement on the conductivity of other lithium salts. In this thesis the effects of melt infiltration on the ion conduction properties of lithium salts other than $LiBH_4$ will be investigated to add to the current scientific knowledge. As such, $LiNH_2$ was used because its chemical properties are similar to those of $LiBH_4$: both compounds are complex metal hydrides and reducing agents. Therefore, a similar behaviour can be expected. Furthermore, research has already been performed on the conductivity of $LiNH_2$ as a pure compound, and a strong increase in conductivity is demonstrated upon formation of a solid solution with $LiBH_4$.[20] Beside $LiNH_2$, $LiNO_3$ will be studied in this thesis. The motivations for this material are its low cost and thermal stability. Because this compound has chemical properties different from those of the complex metal hydrides, being for example oxidizing instead of reducing, different behaviour upon nanoconfinement is expected.

A wide range of metal oxide scaffolds like SiO_2, Al_2O_3, TiO_2, Nb_2O_5 and MgO will be used. Their structural properties will be characterized with N_2-physisorption, whereas pyridine FT-IR and NH_3-TPD will be employed to obtain information on their surface groups. Scaffold pore filling and thermal stability of the infiltrate will be studied with DSC, DRIFTS and XRD. The conductivities of the resulting nanocomposites will be measured with EIS. By investigation of a wide variety of chemical and structural properties of both the $LiNH_2$ and $LiNO_3$ infiltrates and the porous metal oxide scaffolds, the aim of this project is to obtain more insight on the effects of nanoconfinement on the ion conduction properties of Li-based solid electrolytes.

2 Theory

In this work, nanoconfinement of $LiNH_2$ and $LiNO_3$ were performed in porous metal oxide scaffolds to increase their conductivity. In this theory section, first more information on the different scaffolds that were used for melt infiltration in this work and their different properties will be provided in section 2.3. Thereafter, more background information on nanoconfinement and melt infiltration will be provided in section 2.2. Lastly, section 2.4 will provide a theoretical background on the various characterization techniques used in this work.

2.1 Impact of nanoconfinement on conductivity

As was mentioned in the introduction, previous research on the effects of nanoconfinement on electrolyte conductivities has focussed mainly on the compound $LiBH_4$. Research showed that although this compound is not very conductive at room temperature, it becomes conductive after a phase transition at 110℃. This phase transition involves a change in its crystal structure, from an orthorhombic low temperature (LT) phase to a hexagonal high temperature (HT) phase.[15,16] Nanoconfinement was performed in an effort to stabilize the more conductive HT phase at ambient temperatures. The motivation for this approach was the fact that changing the interface and dimensions of a material by confinement in a nanoporous scaffold are known to lower its phase transition temperatures. Indeed, the phase transition temperature of $LiBH_4$ was lowered to 90℃ using this approach. However, in conductivity measurements no transition temperature was observed. Therefore, a more conductive phase unrelated to the HT phase was found to persist to temperatures as low as room temperature.[6] The conductivities of both pure $LiBH_4$ and nanoconfined $LiBH_4$ are shown in figure 2A.

An explanation for this increased conductivity is the presence of a phase with highly mobile ions at the interface between $LiBH_4$ and the scaffold surface, shown in figure 2B. Through detailed analysis and $LiBH_4$ confinement in a range of pore sizes, the layer thickness corresponding to this interfacial layer with highly mobile ions could be determined.[18] Its layer thickness depends on the pore sizes, as well as the chemical nature of the scaffolds. For example, in silica a larger layer thickness was established than in carbon.[18] Further research on the influence of scaffold surface groups was performed by systematically varying the nature and
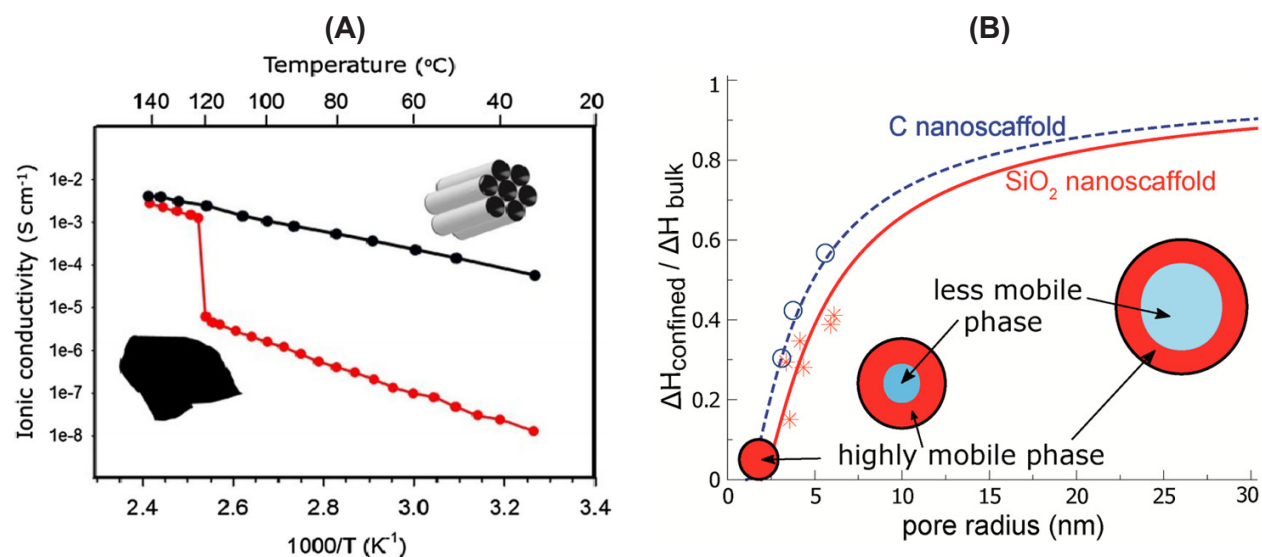
Figure 2: (A) Graph showing the conductivity of $LiBH_4$ (red) as a function of reciprocal temperature, giving an Arrhenius-like plot where the slope of the graph corresponds to the activation energy related to Li^+ ions hopping through the lattice. A phase transition at 110℃ significantly increases its conductivity. This HT phase is stabilized down to room temperature in nanoconfined $LiBH_4$ (black). Duplicated from Jongh et al. [17]. (B) A highly mobile phase is present at the interface between $LiBH_4$ and the scaffold surface. This effect is more pronounced at smaller pore radii. Duplicated from Suwarno et al. [18].

density of SiO_2 surface groups. This research showed that the SiO_2 should be dried at sufficiently high temperatures $(200 - 300$ °C$)$ to remove physisorbed water and reactive vicinal silanol groups. However, drying at higher temperatures resulted in a loss of isolated silanol densities, which in turn decreased the nanocomposite conductivity. Furthermore, replacing the free silanol groups with hydrophobic trimethylsilyl ones led to a conductivity decrease as well.[19] More information on the types of silanol and other surface groups can be found in theory section 2.3.

Preparation methods other than nanoconfinement via melt infiltration have been used for enhancing ionic conductivities in composite systems. An example is ball milling, in which two solids are thoroughly grinded together in a planetary mill by for example tungsten carbide balls.[21] Both preparation methods of nanocrystalline materials have in common that smaller average grain sizes are obtained. As such, large surfaces areas are created, which increase the volume fractions of solid-solid interfacial regions.[22] These solid-solid interfacial regions are reported to have high defect densities and low diffusion barriers due to effects like space charge regions and structural disorder or strain.[17,22] These defects increase the number of mobile charge carriers and hence the conductivity of a material. Regions with low diffusion barriers are desirable, since they provide enhanced hopping rates and decreased energy barriers.[23] By use of these concepts, Breuer et al. [22] were for example able to increase the ionic conductivity of LiF by 2 orders of magnitude after ball milling, and 3 orders of magnitude upon mixing with γ-Al_2O_3. This increase of 3 orders of magnitude is similar to what was found after melt infiltration of $LiBH_4$.[6] Both examples demonstrate the importance of solid-solid interface engineering for obtaining increased Li^+ ionic conductivities.

2.2   Melt infiltration

Melt infiltration is a method for synthesis of nanostructured materials. With this method, first an infiltrate and porous material are mixed together. The porous material provides structural stability, and is referred to in literature as a matrix, scaffold or support. Throughout this work, the term scaffold is opted, since pore fillings higher than 100% are used, where the porous material acts as a template for the resulting nanostructured material. In contrast, the term support is more suitable when individual nanoparticles are supported on the pore walls of a porous material. After mixing together the infiltrate and scaffold, the mixture is heated above the melting point of the infiltrate. The molten infiltrate will then enter the pores of the scaffold due to capillary forces. Once cooled down, a compact solid nanostructure is formed where the infiltrate and porous material are in close contact. Such a structure is called a nanocomposite.[24] The process of melt infiltration is shown schematically in figure 3.

Capillary forces draw the molten infiltrate inside the scaffold pores when a favourable interaction is present between the two. Such an interaction can be characterized by the contact angle θ of a liquid droplet on the scaffold surface, shown in figure 4A. This contact angle depends on the surface energy of the solid γ_{sv}, the surface tension of the liquid γ_{lv} and the solid-liquid interface energy γ_{sl}, as given by Young's equation:[24]

$$\cos\theta = \frac{\gamma_{sv} - \gamma_{sl}}{\gamma_{lv}} \tag{1}$$

Where the subscripts s, l and v indicate interfaces between the solid, liquid and vapour phases, respectively. In the case of favourable interactions and wetting, the contact angle $\theta < 90°$. In the opposite case of non-wetting, $\theta > 90°$. The resulting capillary pressure Δp, required to draw the molten infiltrate inside the scaffold pores, depends on the scaffold pore radius as well. In the case of cylindrical pores with radius r_p, shown in figure 4B, the resulting capillary pressure is given by the Laplace equation:[24]

$$\Delta p = \frac{2\gamma_{lv}\cos\theta}{r_p} = \frac{2(\gamma_{sv} - \gamma_{sl})}{r_p} \tag{2}$$

This equation demonstrates the need for a favourable interaction between the solid scaffold and liquid infiltrate for good melting and successful melt infiltration, as characterized by γ_{sl}. Furthermore, the surface energy of the solid scaffold γ_{sv} is important. The values of for example SiO_2 and Al_2O_3 scaffolds are known from literature,[25,26] as given in table 1. Since the surface energy of SiO_2 is lower, it can be expected that a favourable interaction with the infiltrate will be less likely to occur. If wetting does not occur, surface functionalization or application of an external pressure might be used to induce capillary infiltration.[24]

Melt infiltration has several advantages over other preparation methods like solution impregnation and deposition precipitation. No solvents are involved, and therefore nanostructured materials can be prepared for compounds that would react with or are insoluble in solvents. Furthermore, high degrees of pore filling can be achieved, up to the point where all porous volume is filled. This is ideal for electrolyte purposes, where compact nanocomposites with more than 100% pore filling are desired so that the insulating scaffold is fully covered by a layer of conductive electrolyte.[24] Furthermore, melt infiltration ensures a high contact
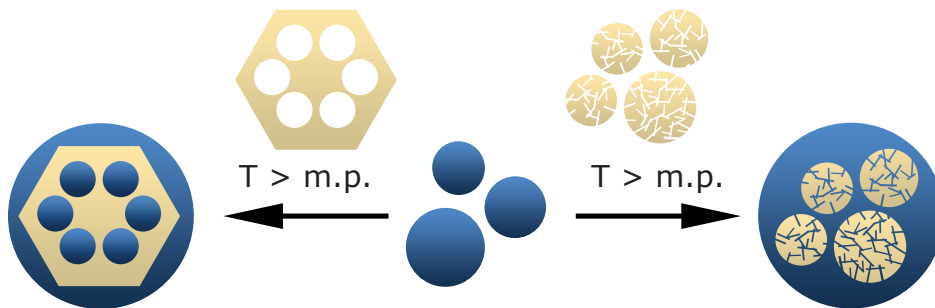
Figure 3: General principle of melt infiltration, where the infiltrate (blue) enters the porous scaffolds (yellow) at temperatures above its melting point.
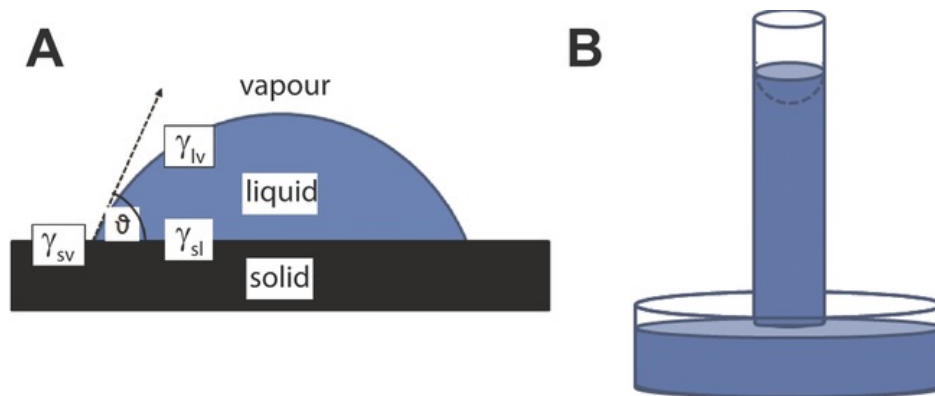
Figure 4: (A) Schematic of a liquid droplet on a flat solid substrate. Wetting is characterized by the contact angle θ and depends on the interfacial energies γ between the solid, liquid and vapour phases. Duplicated from Jongh and Eggenhuisen [24].

area between the electrolyte and scaffold and a uniform distribution of infiltrate throughout the porous network.[23,24]

OH — Si — isolated

HO OH — Si — geminal

H·····H O O — Si — Si — vicinal (H-bonded)

OH — Al — linear (basic)

H O — Al — Al — bridged (acidic)

H O — Al — Al — Al — bridged (acidic)

O⊖ — Al⊕ — O — Al — Lewis acid site   Base site
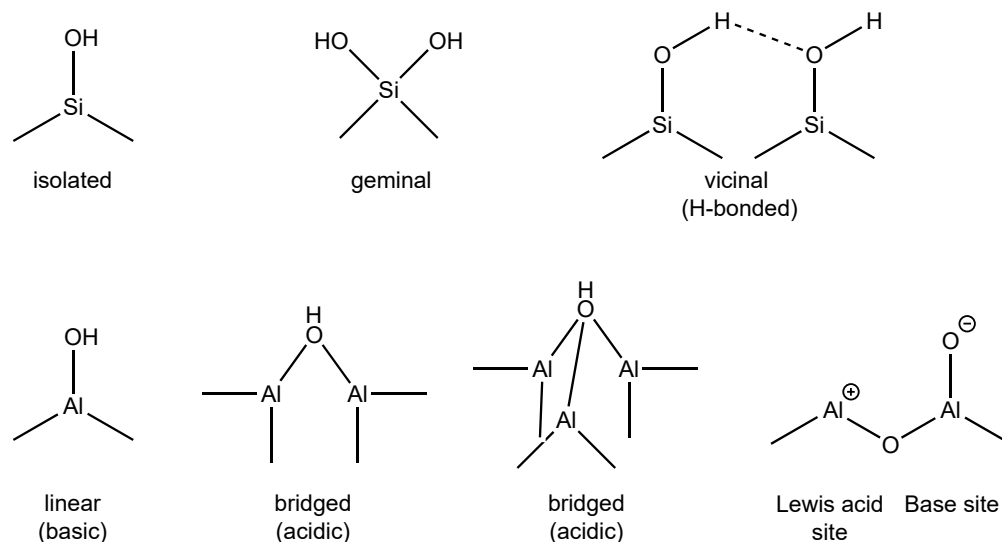
Figure 5: Examples of surface hydroxyl groups on silica and alumina. Alumina also contains Lewis acid sites. Reproduced from Chorkendorff and Niemantsverdriet [36].

2.3 Scaffolds

Both the surface energy of the scaffold and the interaction between the infiltrate and the scaffold have an effect on wetting and successful pore infiltration. Each of these two quantities is affected by the nature of the scaffold surfaces. In general, creating a surface requires chemical bonds to be broken. To minimize the energy cost related to this process, often water molecules are adsorbed at the surface. This results in the formation of surface hydroxyl ($-$OH) groups, which are shown in figure 5 for silica and alumina. In the case of silica, these hydroxyl groups are all weakly Brønsted acidic and have similar chemistries. In the case of alumina however, significant differences are present between the various hydroxyl groups. Whereas the linear hydroxyl groups have a Brønsted basic character, the bridged hydroxyl groups have a Brønsted acidic character. The effect of the Brønsted basic groups is more pronounced, as the point of zero charge (PZC) of alumina is typically above 7. This PZC value provides the pH at which the scaffold is overall neutrally charged.[36] A second difference between SiO_2 and Al_2O_3 is the presence of electron withdrawing Lewis acid and electron donating Lewis base sites on Al_2O_3, which are formed upon dehydration at sufficiently high temperatures.[37,38]

A large variety of scaffolds were used to confine $LiNH_2$ and $LiNO_3$ in this work. As SiO_2 scaffold, Santa Barbara Amorphous-15 (SBA-15) was synthesized via a sol-gel precipitation route.[36] As is shown in figure 6, this scaffold has highly ordered mesoporosity, containing long, cylindrical rod-like pores. Furthermore,

	Surface energy ($\mathrm{J\,m^{-2}}$)	Reducible?	PZC	OH density (molecules $\mathrm{nm^{-2}}$)
SBA-15	0.26[25]	No	4 - 5[27]	7.7[28]
SBA-15-NH_2	-	No	8 - 9[27]	2.6[28]
γ-Al_2O_3	1.52[26]	No	7 - 9[29]	11.5[28]
γ-AlO(OH)	-	No	7 - 8[30]	-
TiO_2 P90	~ 1[31]	Yes	5 - 6[32]	10.2[28]
Nb_2O_5	-	Yes	< 7[33]	-
$Nb_3(PO_4)_5$	-	Yes	< 7[33]	-
MgO	~ 1[34]	No	12 - 13[35]	16.9[28]

Table 1: Table of all scaffolds used in this work and some of their relevant properties.

SBA-15 contains uni-dimensional pore sizes, with high specific surface areas and pore volumes. Depending on the synthesis procedure, these properties can be tuned over a certain range.[39,40] This allows one to systematically study the effect of the structural properties of the scaffold in a certain system of interest. An added benefit is the possibility to change its chemical properties as well, by use of surface modification. In this project, the surface was grafted with (3-Aminopropyl)triethoxysilane molecules. In this way, the acidic surface hydroxyl groups are replaced by basic propylamine ligands, as is shown schematically in figure 7.[41–44] The resulting scaffold will be referred to as SBA-15-NH_2 throughout this thesis.
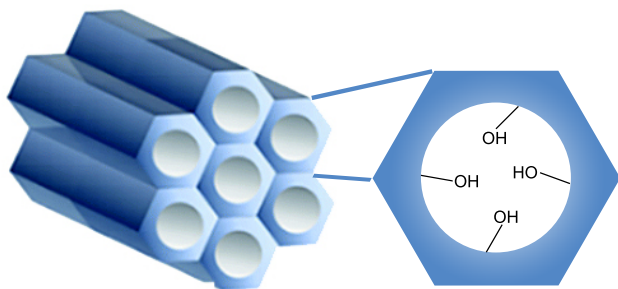
Figure 6: Three-dimensional structure of mesoporous SBA-15 scaffolds, containing long, cylindrical pores that are highly ordered in a hexagonal array. Reproduced from Wu et al. [45].
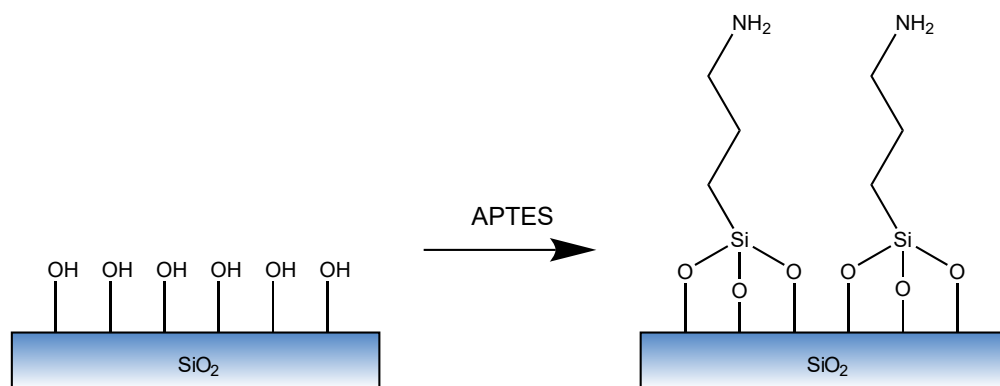
Figure 7: Schematic showing the chemical reaction that occurs with the surface hydroxyl groups of SiO_2 when grafting this compound with APTES. Three surface hydroxyl groups are involved per APTES molecule.[41]

Alumina is the most widely applied scaffold in catalysis, having a higher thermal and mechanical stability than silica. A variety of structures exists, including for example α-, γ-, η- and θ-Al_2O_3. Of these structures, γ-Al_2O_3 is most often used in catalysis because it has the highest porosity. For this reason, it is used in this work as well. It is commercially prepared by thermal dehydration of porous γ-AlO(OH) (boehmite), which will be used in this work to investigate the effect of its higher abundance of surface hydroxyl groups.[36]

A reducible metal oxide which is commonly used in for example photocatalysis is TiO_2. It is commercially available mainly in rutile and anatase crystal structures, and in a mix between the two. An example of such a mixture is TiO_2 P90, which contains a high porosity because it is commercially prepared via a flame hydrolysis route.[46] This scaffold contains many surface hydroxyl groups, is slightly acidic, and contains Lewis acid sites as well.[28,32,46] Another acidic scaffold used in this work is porous Nb_2O_5, which is synthesized by dehydration of amorphous niobic acid ($Nb_2O_5 \cdot nH_2O$).[47] Niobium oxide can be made even more acidic by modification with phosphate groups, forming $Nb_3(PO_4)_5$. Both scaffolds are known to possess both Brønsted and Lewis acid sites.[33] To investigate basicity, MgO is used in this work.[35]

An overview of these scaffolds and some of their relevant properties are given in table 1. It should be noted that these values found in literature were not measured on the scaffolds used in this work, and might therefore deviate depending on for example the supplier, drying temperature, and synthesis procedure.

The surface energies are important for successful melt infiltrations and wetting, as described previously. Most metal oxide scaffolds have surface energies roughly between $0.2 - 2 \; \mathrm{J\,m^{-2}}$.[36] As such, SiO_2 has a relatively low surface energy, whereas Al_2O_3 has a relatively high surface energy. Reducibility indicates whether a the scaffold can be reduced by a reducing agent like $LiNH_2$. If this happens, the scaffold will become a semiconducting material with electronic conductivity, which is undesired for solid electrolyte applications. The point of zero charge (PZC) of a scaffold indicates whether it is mainly acidic (PZC < 7) or basic (PZC > 7) in nature. Lastly, the OH density provides an indication on the density of surface groups present on the scaffold surfaces. These values were reported by Tamura et al. [28] for SiO_2, Al_2O_3, TiO_2 and MgO. It is assumed that the amount of surface groups on SBA-15-NH$_2$ is one third of that for SBA-15, since three hydroxyl groups are replaced by one APTES molecule in the case of a complete grafting reaction. Although this value is denoted OH density, it is important to note that the chemical nature of the aminopropyl surface groups in the case of SBA-15-NH$_2$ is different from hydroxyl groups.

2.4   Characterization techniques

In this work, many techniques were employed for characterization of the as-synthesized electrolytes. This section will describe each of these techniques and their theoretical backgrounds. For practical information on these techniques, the reader is referred to section 3.4.

2.4.1   Electrochemical Impedance Spectroscopy (EIS)

For characterization of electrochemical systems and especially for electrolytes, an important characteristic is the conductivity σ. This conductivity is related to the resistance R of a material according to:

$$\sigma = \frac{d}{AR} \tag{3}$$

in which d represents the distance between the two electrodes and A the surface area of the sample under investigation.

Direct potential

One way to measure this resistance is by application of a direct potential U and measurement of the current I that starts to flow. The resistance will then be given by Ohm's law:

$$R = U/I \tag{4}$$

This approach however is only valid in the case of an ideal resistor. In practice, upon application of a direct potential, immediately ions present in the electrolyte will start to move towards the oppositely charged electrodes. As a result, the electrode potential will be partially screened and the current will rapidly decrease. The applied voltage then no longer resides in the electrolyte bulk, but in the formed electric double layers at the electrode/electrolyte interfaces. In this case, the electrolyte is no longer described as an ideal resistor, but as an ideal resistor (bulk electrolyte) connected in series with two capacitors (charged electrode/electrolyte interfaces).[48–50]

Alternating potential

In practice, systems exhibit more complex behaviour than an ideal resistor, and Ohm's law does not apply. The resistance of a system can be determined with much higher sensitivity and accuracy if measurements are performed in the frequency domain instead of the time domain. This involves application of an alternating potential $U(t)$ and measurement of the resulting alternating current $I(t)$. Instead of the real-valued resistance R, a complex-valued impedance Z is measured. This method is called electrochemical impedance spectroscopy (EIS).[48–52]

An important benefit of this approach is that the applied signal can be varied over a wide range of frequencies, allowing for the possibility to measure and separate resistive and capacitive effects that occur on different time scales. The alternating potential $U(t)$ that is applied generally has a small amplitude. Another benefit is that this keeps the system in its (quasi-)equilibrium state and allows measurements to be performed without large disturbances to the system under investigation, allowing undesired effects like electrode polarization and electrochemical reactions to be minimized.[49,52]

To understand how the electrolyte conductivity can be obtained from EIS, some formulae are required. The applied alternating potential can be expressed in terms of its amplitude U_0 and its frequency ω, as given in equation 5:

$$U(t) = U_0 \cos(\omega t) \tag{5}$$

The measured alternating current generally contains some phase delay ϕ with respect to the applied alternating potential and can be expressed in terms of its amplitude I_0 and frequency ω as well. This is shown in equation 6:[49,50]

$$I(t) = I_0 \cos(\omega t - \phi) \tag{6}$$
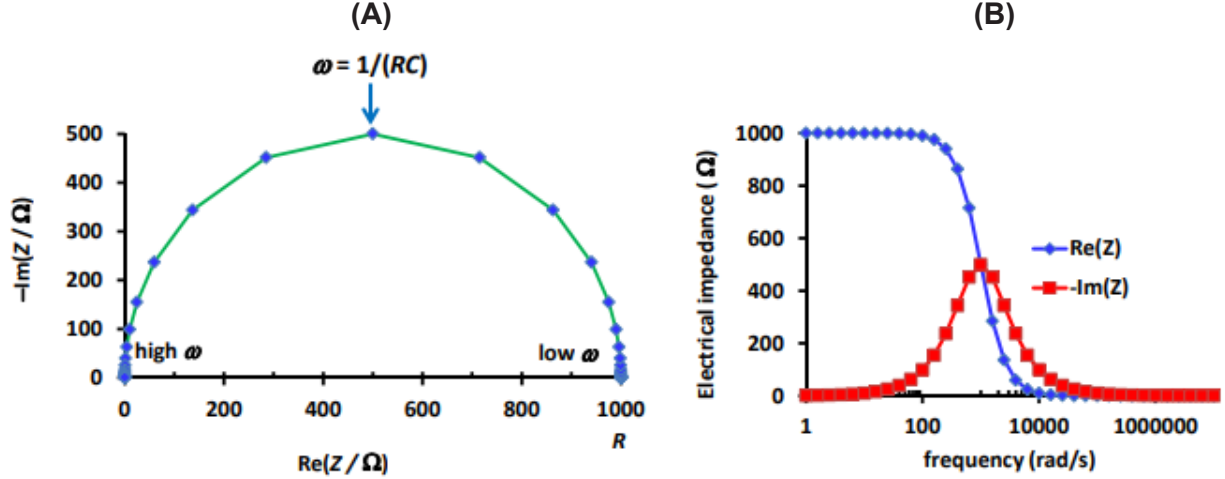
Figure 8: Impedance spectra of a resistor of 1000 Ω, connected in parallel to a capacitor of 1 μF.(A) A Nyquist plot, showing the negative imaginary component of the complex impedance as a function of the positive real one. The resistance follows from the intercept with real axis at low ω. B) Bode plot, showing the real and imaginary components of the complex impedance as a function of frequency ω. Duplicated from Erné [50].

The electrical impedance is given by the ratio between the alternating potential and alternating current:[49]

$$Z(t) = U(t)/I(t) = \frac{U_0 \cos(\omega t)}{I_0 \cos(\omega t - \phi)} \tag{7}$$

Two limiting cases can be distinguished. The first one is where $\phi = 0$. In this case, the alternating current and potential are in phase and the impedance is equal to the real-valued resistance: $Z = R$. This is equivalent to the case of an ideal resistor, as given by Ohm's law in equation 4.[49,50] In the other limiting case, $\phi = \pi/2$ and the alternating current is out of phase with the applied alternating potential. The system then behaves as an ideal capacitor with a characteristic capacitance C. For a capacitor, it is the change in potential which causes a current to flow:[49,50]

$$I = C\frac{dU}{dt} \tag{8}$$

The complex-valued impedance of a capacitor is given by equation 9:[49,50]

$$Z = \frac{1}{i\omega C} \tag{9}$$

With ω the frequency of the alternating current, C the capacitance of the capacitor and $i^2 = -1$. In typical EIS measurements, the real system is fitted with an equivalent electrical circuit analog. In a simple case, the sample is assumed to consist of a resistor and a capacitor, connected in parallel, as shown in figure 9A.[6,48,49] This gives an expression for the impedance, formulated in a real and an imaginary part, as given by equation 10:[49,50]

$$Z = \frac{1}{\frac{1}{R} + i\omega C} = \frac{R}{1 + (\omega RC)^2} - i\frac{\omega R^2 C}{1 + (\omega RC)^2} = Re(Z) + Im(Z) \tag{10}$$

A common way to visualize these results is by a so-called Nyquist plot, in which the negative of the imaginary part of the impedance is plotted versus the real one. For a system that can be modelled as the equivalent circuit in figure 9A, this results in a semicircle. An example of such a Nyquist-plot is shown in figure 8A. The intercept with the x-axis at low ω (high Z_{Re}) in this ideal case gives the resistance, from which the conductivity σ can be calculated via equation 3.[49,50]
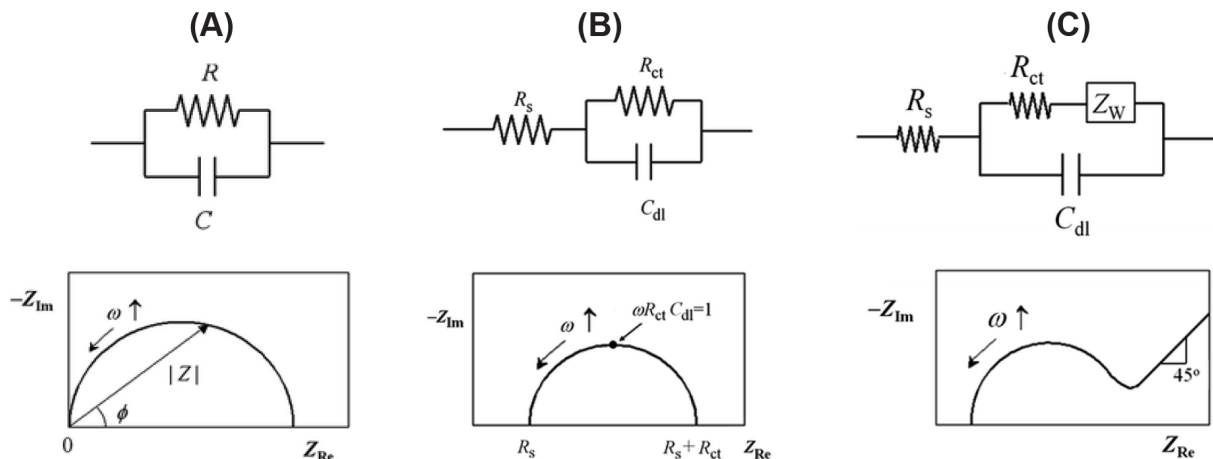
Figure 9: Three different equivalent circuit analogues and their corresponding Nyquist plots. (A) Simplest case of a resistor and capacitor connected in parallel. (B) An additional resistance is present in the electrochemical system. (C) Electrode polarization occurs at low frequencies, causing a straight line in the Nyquist plot. Reproduced from Pyun et al. [49].

Furthermore, the maximum of the Nyquist plot provides the capacitance C and characteristic frequency ω of a system via equation 11:[49,50]

$$\omega = \frac{1}{RC} \tag{11}$$

The value for ω yields information on for example the characteristic time scales at which conduction or ionic diffusion through the material takes place.[49] A drawback of the Nyquist plot is however that is does not specifically show the frequency corresponding to a certain impedance value. For this purpose, sometimes the Bode plot is used, as shown in figure 8B.[48,50]

Deviations from this ideal behaviour might occur, yielding Nyquist plots that do not show a perfect semicircle. An example is the presence of an additional resistance in the electrochemical system, which causes the semicircle to be displaced to higher real impedance values, as shown in figure 9B. Another example is electrode polarization, which causes the occurrence of a straight line at low ω values. This is shown in figure 9C. A proper choice for an equivalent circuit analog is therefore important, depending on the system of interest.[49,51]

Activation energy

Analysis of the Nyquist plots and corresponding equivalent circuit analogues yield the electrolyte resistance and conductivity via equation 3. In a typical analysis, these conductivities are measured in a certain temperature range where Arrhenius behaviour can be observed, as described by equation 12:

$$\sigma = \sigma_0 e^{-E_A/k_B T} \tag{12}$$

By visualizing the logarithmic conductivities as a function of reciprocal temperature in an Arrhenius plot, the activation energy related to the main conduction mechanism in the electrolyte is obtained from the slope of the graph. In the case of Li^+ ionic conduction in solid electrolytes, this activation energy corresponds to Li^+ ions hopping between crystal lattice sites. The lower the activation energy, the more facile Li^+ ions can diffuse though the electrolyte. The height of the conductivities in the Arrhenius plot is related to the number of mobile charge carriers.[6]

2.4.2   Differential Scanning Calorimetry (DSC)

Differential Scanning Calorimetry (DSC) is a thermo-analytical technique, which can be used to measure the calorimetric properties of materials. By using DSC, information be gained on any endothermic or exothermic
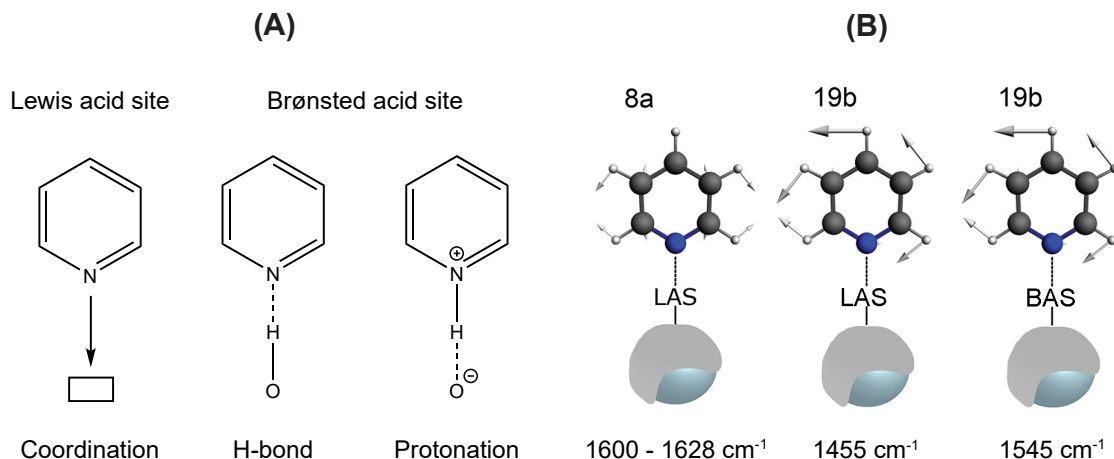
Figure 10: (A) Adsorption of pyridine can occur on both Lewis acid sites (coordination) and Brønsted acid sites. Depending on BAS strength, neutral hydrogen bonding or ionic bonding and protonation may occur. (B) Adsorption of pyridine onto an acid site influences the ν_{8a} and ν_{19b} aromatic ring vibrations, causing them to be visible at given wave numbers in an FT-IR spectrum. Image adapted from Velthoen et al. [55].

events in a material. In a typical measurement, the heat flow in and out of a sample are measured with respect to a reference sample. The temperature of the sample and reference sample are increased during a measurement, and the difference in heat required to increase their temperatures by the same amount are measured as a function of time or temperature. In this way, DSC can provide both qualitative and quantitative information on the calorimetric properties of a material.[53]

Firstly, endothermic and exothermic phase transitions in the material like melting and recrystallization can be monitored. When such a phase transition occurs, either more or less heat is required to maintain the sample at the same temperature as the reference, respectively. This allows for qualitative analysis, namely at which temperature the phase transition occurs. This is relevant for nanoconfinement, since nanoconfined materials exhibit phase transitions at lower temperatures than their bulk counterparts.[6,54]

Secondly, the stability of a compound during heat treatment can be checked. If the compound is stable, no significant differences should be visible upon comparing the results of several heating cycles.

Quantitative analysis of DSC data is possible as well. By integration of the peak area corresponding to a certain phase transition, and the known mass of a sample, the specific enthalpy of that phase transition can be calculated. In the case of melting and crystallization, these are referred to as the enthalpies of fusion and solidification, respectively. After measuring the bulk enthalpy of fusion, this value can be used to calculate the amount of compound present in other samples as well. This is important for nano-confined samples, where the specific melting enthalpy can be used to quantify the amount of extraporous material present. The amount of intraporous material follows from subtraction of the amount of extraporous material from the total amount of material added ($m_{intraporous} = m_{added} - m_{extraporous}$).[54]

2.4.3   Pyridine FT-IR

The presence of acid sites on a metal oxide scaffold surface often plays an important role in catalysis. In this work, the interaction of lithium salts with the scaffold surface is of interest, which might be affected by the presence of acid sites as well. To characterize the nature and abundance of these acid sites, FT-IR spectroscopy is widely employed in combination with basic probe molecules. For this purpose, pyridine is most often used. The nitrogen lone pair on pyridine makes this molecule a relatively strong base ($pK_b = 5.25$),[56] allowing it to adsorb on acid sites as shown in figure 10A. In the case of weak and strong Brønsted acid sites (BAS), hydrogen bonding (neutral) or ionic bonding (protonation) may occur, respectively. Furthermore, coordination to Lewis acid sites (LAS) is possible.[55,56]

Adsorption of pyridine on these different acid sites causes characteristic shifts of its vibrational modes. The infrared absorption spectrum of pyridine can roughly be divided into two parts. The first is related to

ν(CH) modes of the aromatic ring, causing vibrations in the $2700 - 3100$ cm^{-1} spectral region. Although literature suggests that this spectral region is more well-suited in distinguishing hydrogen bonded from weakly coordinated species, in this master thesis we will focus mainly on the other spectral region between $1400 - 1700$ cm^{-1}.[56]

In the range of $1400 - 1700$ cm^{-1}, aromatic ring vibrations can be studied. Four modes occur in this region, of which the ν_{8a} and ν_{19b} are of particular interest, shown in figure 10B. They provide information on the nature of the adsorption interaction, without overlapping with other vibrational modes. Once a pyridine molecule is protonated by a Brønsted acid site, its ν_{19b} vibration will shift to 1545 cm^{-1}. However, when the pyridine molecule is coordinated to a Lewis acid site, the ν_{19b} vibration will be present at around 1455 cm^{-1}. The position of this peak is relatively insensitive to the nature of the acid site. Coordination to a Lewis acid site is also characterized by a band related to the ν_{8b} vibration. This band occurs between about $1600 - 1628$ cm^{-1}, with larger wave numbers corresponding to stronger Lewis acid sites.[56,57]

Beside qualitative information, Pyridine FT-IR may provide quantitative information on the amount of Brønsted and Lewis acid sites present. This can be done by integration of the infrared absorption bands related to the ν_{19b} aromatic ring vibrations, being at 1545 cm^{-1} for BAS and around 1455 cm^{-1} for LAS. Thereafter, Lambert-Beer's law as given in equation 13 can be applied, assuming one adsorbed pyridine molecule per acid site:[55,58]

$$C = \frac{A}{\rho A_0} \tag{13}$$

Here, C equals the concentration of BAS or LAS on the scaffold surface (mmol g^{-1}). A represents the integrated absorbance, which can be determined through band integration of the absorbance peak. A_0 represents the apparent integral absorption coefficient (cm μmol^{-1}). Emeis [58] has determined its values to be 1.67 (at 1545 cm^{-1}) and 2.22 (at 1455 cm^{-1}) for pyridine adsorbed on Brønsted and Lewis acid sites, respectively. The effective cross-section ρ (mg cm^{-2}) can be calculated using the mass (mg) and area (cm^2) of the self-supporting wafer of sample used in the experiment.[55]

2.4.4   NH$_3$-Temperature Programmed Desorption (NH$_3$-TPD)

A second basic probe molecule for the characterization of acid sites on scaffold surfaces is NH$_3$. It is a very strong base, and therefore adsorbs strongly on a scaffold surface. This makes it less specific than for example pyridine. Furthermore, it is impossible to distinguish between Brønsted and Lewis acidity using NH$_3$. An advantage of using NH$_3$ however, is that it is especially well-suited for probing microporous channels, which are too small for the larger pyridine molecule to enter but are accessible for NH$_3$.[59]

Upon performing temperature programmed desorption measurements, an indication on the acid site strength is given by the temperature at which NH$_3$ desorbs. Although in an ideal case only one peak is present in a TPD-profile, often NH$_3$ can bind in more than one state to the surface, causing overlapping peaks that need to be deconvoluted.[60]

Quantitative information can be gained on the amount of acid sites present by looking at the NH$_3$ desorption as a function of time. Whereas pyridine generally provides an underestimation of the total amount of acid sites, because it cannot access or does not bind strong enough to some acid sites, NH$_3$-TPD generally gives an overestimation of the total amount of acid sites. This can be due to its strong and non-specific binding, but also effects like re-adsorption and diffusion in the porous framework play an important role.[10,59–61]

3 Experimental methods

This section will describe the experimental details and procedures of this work. First, all chemicals which were used are listed. Secondly, the preparation of scaffolds is elaborated on. Thereafter, the experimental procedures for melt infiltrations are given. Lastly, the practical aspects of all techniques in this work are given.

3.1 Chemicals

All chemicals were purchased from their supplier and used without further purification. They were stored and handled in a glovebox with inert Ar atmosphere (typical impurity levels of $O_2 \leq 0.1$ ppm, $H_2O \leq 0.1$ ppm).

γ-Al_2O_3 (Puralox SCCa-5/200, 98%) and boehmite (Catapal B alumina, γ-AlO(OH), 72%) were obtained from Sasol, SiO_2 (Aerosil380, $\geq$ 99.8% SiO_2 content) and TiO_2 (Aeroxide P90, $\geq$ 99.5%) from Evonik, MgO ($\geq$ 95%) and CaO (99.9%) nanopowders from Strem chemicals, and niobium oxide hydrate ($Nb_2O_5 \cdot nH_2O$, HY-340, AD/4465) and niobium phosphate ($Nb_3(PO_4)_5$, AD-210) from CBMM (Companhia Brasileira de Metalurgia e Mineração). Toluene (99.85%, extra dry over molecular sieve, AcroSeal) and KBr ($\geq$ 99%, for spectroscopy, IR grade) were purchased from Acros Organics, HCl (37 wt%, fuming) from Merck, and diethyl ether (99.5+%) from Chem-Lab NV.

All other compounds were purchased from Sigma-Aldrich, including poly(ethylene oxide)-block-poly(propylene oxide)-block-poly-(ethylene oxide) triblock copolymer ($EO_{20}PO_{70}EO_{20}$, Pluronic P-123, average $M_n \sim 5800$ Da), tetraethyl orthosilicate (TEOS, >99%), hexadecyl trimethyl ammonium bromide (CTAB, $\geq$ 96%), tetramethyl ammonium hydroxide (TMAOH, 25 wt% in H_2O), aminopropyl triethoxysilane (APTES, 99%), $LiNO_3$ (99.99%, trace metals basis), $LiNH_2$ (95%), $NaNH_2$ (98%), metallic Li ribbons (thickness 0.38 mm, width 23 mm, 99.9%, trace metals basis), $LiIO_3$ (97%), and anhydrous pyridine (99%, Sigma-Aldrich).

3.2 Scaffold synthesis

As ordered mesoporous silica scaffold, SBA-15 was synthesized. Furthermore, surface functionalization was applied to this scaffold as well. The synthesis procedures, as well as the drying procedures for other scaffolds are described in the following sections.

3.2.1 Synthesis of SBA-15

Synthesis of SBA-15 was based upon the procedure described by Lee et al. [40]. First, 23.58 g Pluronic P-123, 607.97 g deionized water and 146.60 g HCl were brought into a 1 L polypropylene bottle (cylindrical, height 19.7 cm, diameter 10.5 cm). The mixture was heated to 55 °C in an oil bath under vigorous stirring for 4 hours. Stirring was increased to 600 rpm, then 50.07 g TEOS was added. Heating and stirring were continued for 2 more minutes of hydrolysis time. Condensation was continued by heating the mixture to 55 °C for 24 hours in an oven, after which it was heated to 90 °C for another 24 hours. The SBA-15 was washed and filtered with deionized water. This was continued until the filtrate was at a pH of 5. The residue was brought into a mortar and dried at 60 °C for 3 days. A calcination step followed, in which the solid was heated (heating ramp of 1 °C/min) and kept at 550 °C for 6 hours in static air. A drying step followed before bringing the product into inert Ar atmosphere, by heating the product to 120 °C under vacuum (1 mbar) and magnetic stirring for 24 hours.

3.2.2 Grafting SBA-15 with APTES

SBA-15 was functionalized by grafting with APTES according to the procedure as described by Masoud et al. [41], in a similar manner as the procedures of Liu et al. [44], Chi, Lin, and Mou [42] and Munguía-Cortés et al. [43]. For this synthesis, 1.5 g dry SBA-15 was brought into a 100 mL round-bottomed flask and put under N_2 pressure, after which 50 mL dry toluene and 1.31 g APTES were added. The amount of APTES needed was calculated based on the BET surface area of the SBA-15, assuming 3 OH groups per nm^2.[41] The mixture was refluxed at 110 °C for 24 hours under vigorous stirring (750 rpm). After cooling down, the functionalized SBA-15 was filtered and washed with 80 mL toluene and 60 mL diethyl ether. The product

was dried for 24 hours under vacuum and magnetic stirring before storage under inert Ar atmosphere. The as-obtained aminopropyl-funtionalized SBA-15 will be denoted SBA-15-NH$_2$ throughout this thesis.

3.2.3 Preparation of other scaffolds

All scaffolds were dried before storage and use. γ-Al$_2$O$_3$ and γ-AlO(OH) were dried by heating (5 °C/min) the materials under a N$_2$ flow of 50 mL/min to 300 °C, and staying at this temperature for 4 hours. TiO$_2$ P90 was dried at 120 °C under vacuum (1 mbar) and magnetic stirring for 20 hours. Nb$_2$O$_5 \cdot$ nH$_2$O and Nb$_3$(PO$_4$)$_5$ were dried by heating the materials in 2 hours time (much water evaporated) to 200 °C under magnetic stirring and vacuum (1 mbar), and remaining at this temperature for 22 hours.

3.3 Melt infiltrations

Melt infiltrations were carried out using both LiNO$_3$ and LiNH$_2$. Before melting, the lithium salts and scaffolds were mixed thoroughly using a mortar and pestle to ensure close proximity. Added amounts were based on the desired degrees of pore filling, which were calculated using the pore volume of the scaffolds as determined by N$_2$ physisorption and the density of the lithium salts, being 2.38 g/cm^3 for LiNO$_3$ and 1.18 g/cm^3 for LiNH$_2$.

3.3.1 Melt infiltrations with LiNO$_3$

Melt infiltrations of LiNO$_3$ were carried out by heating the mixture in stainless steel or glass containers, which were placed in a Parr stainless steel autoclave with Teflon O-ring, equipped with pressure indicator. This autoclave is shown figure 11. Reaction conditions involved heating the sample to 275 °C (20 °C above melting point LiNO$_3$) with a ramp of 150 °C/h and maintaining this temperature for 30 minutes under 30 bar Ar pressure.

3.3.2 Melt infiltrations with LiNH$_2$

Due to the presence of the Teflon O-ring, which melts at temperatures above 300 °C, the aforementioned autoclaves were not suited for melt infiltrations of LiNH$_2$, which required temperatures above 390 °C. Therefore, melt infiltrations of LiNH$_2$ were carried out by heating the mixtures in ceramic reactors that were placed in tightly closed stainless steel reactors. A photograph of these reactors is shown in figure 12.

To prevent decomposition of LiNH$_2$, NH$_3$ pressure is required. This was generated *in-situ* by the thermal decomposition of NaNH$_2$.[62] For this purpose, a 1:1 wt% mixture of NaNH$_2$ and SiO$_2$ was placed at the

Figure 11: Picture of an autoclave, equipped with a pressure indicator, as used for LiNO$_3$ melt infiltrations. Image taken from https://www.parrinst.com/.

Figure 12: Photograph of reactor components used for carrying out melt infiltrations with LiNH$_2$, showing a white ceramic container, grey graphite foil and stainless steel reactors.
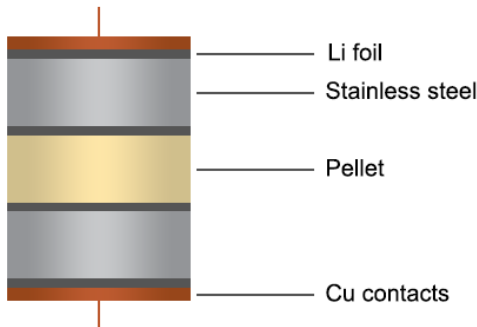
Figure 13: Schematic overview of a symmetrical pellet, as used for EIS measurements. The pellet is pressed between two stainless steel dies using 2 tonnes of force. Both sides of the dies are covered with Li foil to ensure good electrical contact.

bottom of the reactors, covered by a circle of graphite foil. SiO_2 was added to hinder the formation of volatile Na, which would contaminate the $LiNH_2$ samples, by reaction of Na and SiO_2 to form sodium silicates.[63] Heat treatment involved heating the sample to 410 °C (20 °C above melting point $LiNH_2$) with a ramp of 150 °C/h and maintaining this temperature for 30 minutes. After reaction, samples were crushed using a mortar and pestle.

3.4   Characterization techniques

3.4.1   Electrochemical Impedance Spectroscopy (EIS)

Before use, traces of metal oxide were removed from metallic lithium foil by scraping the surface. Circles ($\varnothing$12mm) were cut out and placed on hardened steel pellet dies ($\varnothing$13mm). In between two dies, about 80 to 150 mg or 150 to 250 mg of, respectively, $LiNH_2$ or $LiNO_3$ containing sample was placed. Metallic lithium foil ends faced towards the sample, ensuring good electrical contact. The samples were pressed into a pellet using 2 tonnes of force (pressure of $1.5 * 10^3$ bar). Typical values for pellet thickness involved 0.5 to 1 mm. Void fractions of the pellets were estimated based on the dimensions and weight of the pellets and bulk densities of the materials. For pure $LiNH_2$ and $LiNO_3$, void fractions of 14% and 16% were obtained, whereas for their nanocomposites void fractions between 30% - 50% were calculated.

The as-obtained pellets were put in a measurement cell with metallic copper contacts, again with lithium foil at the interfaces to ensure good electrical contact. This measurement cell was built in-house, based on a design of Danmarks Tekniske Universitet. A schematic of the as-prepared symmetrical pellet is shown in figure 13.

Measurements were performed using a Princeton Applied Research PARSTAT 2273 potentiostat, with applied frequencies ranging from 1 - 10^6 Hz in 120 logarithmically displaced steps. A thermocouple was located in between the two measurement cells to allow temperature-dependent measurements, with an ICP DAS I-7018P analog input module to handle communication between the thermocouple and computer. The measurement cell itself was located in a Büchi Glass Oven B-585 Drying, which was modified to allow use with a Watlow EZ-Zone PM PID temperature controller. Each sample was first heated at 5 °C/min to 130 °C, with measurements carried out every 10 °C once the temperature had stabilized. After heating, the sample was cooled down and measurements were taken every 20 °C, again once the temperature had stabilized. No deviations between conductivity data during heating and cooling were observed in the results presented in this thesis.

The results were fitted using an equivalent circuit consisting of a resistance and constant phase element connected in parallel. The results were visualized as Nyquist plots in Matlab. The intersection of the fitted semicircles with the real axis was assumed to provide the pellet resistance R only. This value was converted into a value for conductivity (σ) according to equation 14:

$$\sigma = \frac{d}{AR} \tag{14}$$

where d equals the pellet thickness as determined with a calliper and A equals the pellet cross-section of 1.33 cm^2.

3.4.2   Differential Scanning Calorimetry (DSC)

Differential Scanning Calorimety (DSC) measurements were performed on a high pressure HP DSC1 MultiSTAR apparatus from Mettler Toledo, equipped with an FRS5 sensor. About 5 - 10 mg of sample was placed in hermetically sealed aluminum pans of 40 µL. Calibrations were performed using certified In and Zn samples. An Ar pressure of 2 bar and an Ar flow of 10 mL/min were used for all measurements. LiNO$_3$ samples were measured from 30 - 300 °C and LiNH$_2$ samples were measured from 30 - 410 °C, with heating and cooling rates of 5 °C/min and three heating and cooling cycles in total. The pure LiNO$_3$ and LiNH$_2$ samples were used as a reference for measuring the bulk enthalpies of the melting transitions in the solids. The thermograms were analysed using STARe software.

3.4.3   X-Ray Diffraction (XRD)

Samples for XRD measurements were prepared by placing a layer of powder on a Bruker airtight specimen holder. After closing the holder tightly, the sample was transferred to the diffractometer. Measurements were performed at room temperature using a Bruker AXS Advance D8 diffractometer, equipped with Co Kα radiation ($\lambda = 1.78897$ Å). It was operated at 30 kV and 40 mA. XRD patterns were collected from 2θ = 15-90°, using a step size of $2\theta = 0.033$° and scan speed of 2.0 s.

3.4.4   N$_2$ physisorption

For N$_2$ physisorption measurements, samples were prepared in an airtight physisorption tube. Measurements were carried out at -196 °C on a Micromeritics TriStar II Plus Surface Area and Porosity Analyzer. The desorption branch of the physisorption isotherms was used to determine the Barrett, Joyner and Halenda (BJH) pore size distributions of the scaffolds. Total pore volume was assessed by the single point adsorption at p/p° = 0.995, whereas the t-plot micropore volume was calculated using a Harkins-Jura reference isotherm. Surface areas were calculated using the Brunauer-Emmett-Teller (BET) method.

3.4.5   Diffuse Reflectance Infrared Fourier Transform Spectroscopy (DRIFTS)

A few mg of sample was brought into a 40 µL aluminum pan and placed inside a home-made Harrick Praying Mantis airtight sample holder. Thereafter, DRIFTS measurements were performed at room temperature on a PerkinElmer Frontier FT-IR spectrometer with MCT detector. KBr background spectra were acquired before measuring any samples and subtracted from the sample spectra. Each spectrum was taken from 4500 to 400 cm^{-1} with a resolution of 4 cm^{-1} averaging over 16 scans.

3.4.6   Pyridine FT-IR

Sample preparation for pyridine FT-IR measurements involved pressing $4 - 16$ mg, the pressure and weight depending on the sample, into a self-supporting wafer ($\varnothing$7mm). This wafer was placed in a measurement cell, which allowed switching between high vacuum (10^{-5} bar) and pyridine vapour. FT-IR measurements were carried out in transmission mode on a PerkinElmer 2000 instrument with a DTGS detector. Each spectrum was taken from 4500 - 400 cm^{-1} with a resolution of 4 cm^{-1} averaging over 32 scans.
At room temperature, pyridine vapour (22-23 mbar) was dosed to the sample for at least 30 minutes until saturation. Subsequent vacuum desorption for 30 minutes ensured the removal of any physisorbed pyridine. A temperature programmed desorption followed, by heating the sample to 150 °C with a heating rate of 2.5 °C/min, then staying at this temperature for 30 minutes and finally heating the sample from 150 °C to 550 °C with a heating rate of 10 °C/min. Spectra were taken every 50 °C to follow the thermal pyridine desorption. Additionally, a spectrum was taken after 30 minutes at 150 °C, which was used for quantitative analysis. Band integration of the absorbance peaks was performed using the Spectrum program of PerkinElmer. Assuming one adsorbed pyridine molecule per acid site, these values yielded the number of acid sites through equation 15, as mentioned before in theory section 2.4.3.

$$C_{LAS} = \frac{A}{\rho A_0} \tag{15}$$

3.4.7 NH₃-Temperature Programmed Desorption (NH₃-TPD)

About 0.08 - 0.1 g of sample was prepared for NH$_3$-TPD measurements in a glass tube, covered on both sides with quartz wool. During transfer to the apparatus, brief exposure to air occurred. Measurements were carried out on a Micromeritics ASAP2920 apparatus equipped with a thermal conductivity detector (TCD), which had been calibrated for the intensity of ammonia using ammonia gas in a sample loop. The sample was first dried *in-situ* by heating the sample with a ramp of 10 °C/min to 200 °C under He flow of 50 cm^3 STP/min and remaining at that temperature for 10 minutes. The sample was then cooled to 100 °C. At this temperature, fifteen NH$_3$ pulses were dosed of 25 cm^3 STP/min to saturate the sample with NH$_3$. Subsequently, 60 minutes waiting time ensured the removal of any physisorbed NH$_3$. Thereafter, thermal NH$_3$ desorption was induced by heating the sample to 600 °C with a heating rate of 10 °C/min.

Quantification of the amount of acid sites was done by analysis in the Origin9.1 program and involved baseline subtraction and fitting the measured TCD concentrations versus time with two Gaussian peaks. One adsorbed NH$_3$ molecule per acid site was assumed. The measured TCD concentrations versus temperature were fitted in the same way to obtain information on acid site strengths.

4   Results and discussion: LiNO₃ nanocomposites

In this master thesis, the effect of nanoconfinement on the conductivity of two different lithium salts was tested: $LiNO_3$ and $LiNH_2$. In this chapter, the results obtained for the $LiNO_3$ compounds will be discussed.

4.1   Heat treatment of LiNO₃

Melt infiltration requires thermal stability of the infiltrate. To verify whether $LiNO_3$ is stable during heating, DSC was employed, followed by characterization of the heated product with DRIFTS and XRD. Furthermore, EIS measurements were performed to investigate the effect of melting and recrystallization on the conductivity of $LiNO_3$.

4.1.1   Stability of LiNO₃ under heat treatment

To investigate whether $LiNO_3$ is stable at temperatures up to 300 °C, DSC was employed. The results for pure $LiNO_3$ are shown in figure 14A. Up to 250 °C, the heating graphs represent a straight horizontal line, indicating that a constant amount of heat is required to increase the temperature of $LiNO_3$ by the same amount. Starting at around 251 °C however, a peak is observed that can be related to melting of $LiNO_3$. The onset temperatures are tabulated in table 2, and are in agreement with values found in literature for non-hydrated $LiNO_3$.[64]
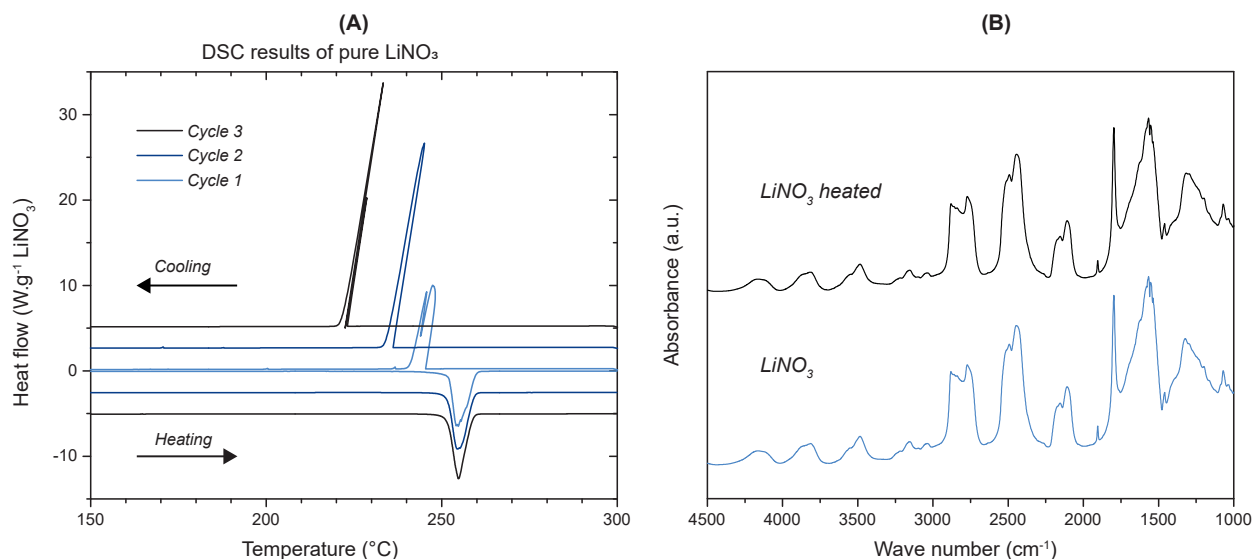
Figure 14: (A) DSC results for pure $LiNO_3$. The x-axis shows the temperature in °C in the relevant range, the y-axis shows the total heat flow normalized by the weight of $LiNO_3$ present in the sample $(W\,g^{-1})$. The three bottom and top graphs indicate heating and cooling, respectively. Inside to outside (light to dark) indicate three subsequent heating and cooling cycles, offset by $0\,W/gLiNO_3$, $2.5\,W/gLiNO_3$ and $5\,W/gLiNO_3$ for clarity. (B) Characterization of $LiNO_3$ before and after heat treatment as performed with DRIFTS, showing two identical spectra.

Cycle	Onset (°C)	Enthalpy $(J\,g^{-1})$
1	251.9	-383.8
2	251.4	-390.8
3	251.3	-386.7

Table 2: Tabulated results from DSC measurements on melting of pure $LiNO_3$
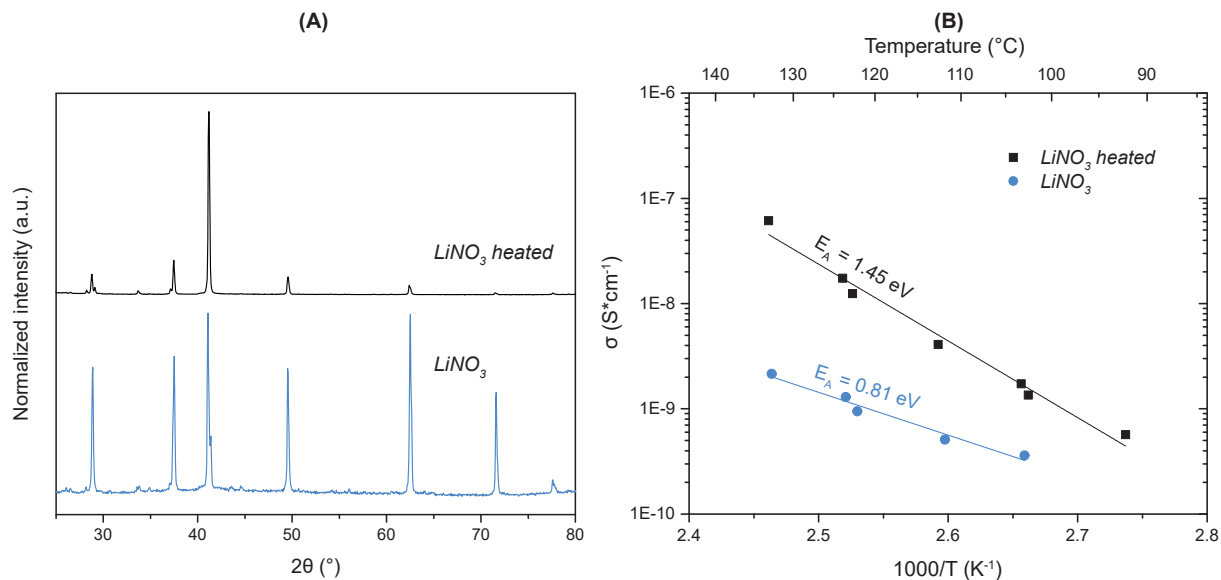
Figure 15: (A) Structural characterization of LiNO$_3$ before and after heat treatment as performed with XRD. (B) Results of EIS measurements on LiNO$_3$ before and after heating.

The cooling graphs show opposite results, each with a positive peak corresponding to the exothermic recrystallization of LiNO$_3$. The temperatures at which these phase transitions occur are lower than the ones obtained for melting of LiNO$_3$. The cause for this delay is not thermodynamic but kinetic in origin, because recrystallization first requires the (delayed) formation of critical nuclei. A heating rate smaller than the 5 °C min^{-1} used might have allowed for longer equilibration times, and thereby decrease the temperature difference that is visible here.

By integration of the peak area corresponding to an exo- or endothermic event, quantitative information can be gained. For this purpose, using the melting peak areas is more suitable, since these are not kinetically hindered. Integration of the three melting peaks yielded enthalpies as shown in table 2. These values are all three very similar, indicating that the total amount of material remains constant over all three cycles and the compound is stable under these conditions. The average enthalpy equals -387 J g^{-1} or -26.7 kJ mol^{-1}, which is in accordance with values found in literature.[65]

4.1.2   Characterization of heated LiNO₃

To corroborate the thermal stability of LiNO$_3$ found with DSC, the compound was characterized with both DRIFTS and XRD before and after heat treatment. The results are shown in figure 14B and 15A.

The DRIFTS spectra in figure 14B show vibration energies corresponding to stretching and bending of the three N−O bonds in the LiNO$_3$ molecule. No clear differences are present between the two spectra, indicating that the chemical bonds present in LiNO$_3$ do not change upon heat treatment, and the compound is thermally stable.

Figure 15A shows the XRD patterns of LiNO$_3$ before and after heat treatment. In these two diffraction patterns, peaks are visible at equal diffraction angles, in accordance with the reference pattern of Wu, Fronczek, and Butler [66]. However, the relative peak intensities for LiNO$_3$ before and after heating are different, with the heated LiNO$_3$ sample showing a higher intensity at $2\theta = 41°$ (hkl = 006) as compared to the other diffraction peaks. An explanation for this could be preferred orientation, in which the LiNO$_3$ crystals orient parallel with respect to each other. This effect distorts the relative peak intensities as compared to a random randomly oriented diffraction pattern.

Despite the differing intensities, the two peak patterns at equal diffraction angles indicate that the crystallographic structure of LiNO$_3$ is not affected by heating. Therefore, no chemical reaction has taken place. From DSC, DRIFTS and XRD we can therefore conclude that LiNO$_3$ is thermally stable.

4.1.3   Effect of heat treatment on conductivity LiNO₃

To investigate the effect of heat treatment on the conductivity of $LiNO_3$, EIS measurements were performed. The results are shown in figure 15B, in which the conductivity of the material is shown as function of reciprocal temperature. In this way, the slope of the graph represents the activation energy for hopping of the mobile species through the material. Practical considerations like pellet thickness and apparatus sensitivity make it impossible to determine conductivities below 10^{-9} S cm^{-1}.

Figure 15B shows that the conductivity of $LiNO_3$ is improved over this temperature range after heat treatment. On the other hand, the activation energy increases as well. Because the slope of $LiNO_3$ before heating is much lower, extrapolation of these data to room temperature shows that its conductivity is actually higher at room temperature ($4.8 \cdot 10^{-13}$ instead of $1.3 \cdot 10^{-14}$). However, these measurement points were taken in a low sensitivity region with much noise. Therefore, the determinations of activation energy and conductivity at room temperature are not accurate.

Nevertheless, it is striking that conductivity differences between $LiNO_3$ before and after heat treatment can be observed, since DSC, DRIFTS and XRD gave no indication on any significant chemical changes upon heat treatment. The only change was visible in the XRD patterns, where a preferred orientation in the hkl = 006 direction was observed. Perhaps the orientation of $LiNO_3$ crystals have an effect on their conductivity. On the other hand, melting and recrystallization of the material might also induce other structural changes which are not probed with these techniques. Perhaps the amount of defects or grain boundaries is affected, thereby affecting the amount of mobile charge carriers.[23] Performing quantitative XRD and more extensive analyses might provide more insight into this phenomenon.

4.2   Characterization of scaffolds used for LiNO₃ melt infiltrations

The scaffolds used for melt infiltrations with $LiNO_3$ were characterized using N_2-physisorption for their porous properties, and with pyridine-FTIR and NH_3-TPD to investigate the presence of acid sites on their surfaces. The results will be described in this section.

4.2.1   Porosity

The porous properties of the scaffolds used for melt infiltrations with $LiNO_3$ were characterized using N_2-physisorption. The resulting isotherms are shown in figure 16A, where the single point adsorption at $p/p° = 0.995$ gives the total pore volume of each scaffold. From this, it is clear that SBA-15 has the highest pore volume, followed by γ-Al_2O_3 and TiO_2 P90, which have similar pore volumes. Thereafter, $Nb_3(PO_4)_5$ and then Nb_2O_5 have the lowest pore volumes. The exact values, together with the BET surface areas and average pore diameters are provided in table 3.

Pore diameters of the scaffolds are given by the BJH pore size distributions, which are shown in figure 16B. It is clear that TiO_2 P90 contains the largest pores (> 20nm), with a large pore size distribution. All other scaffolds have smaller pores (< 20nm), in increasing order Nb_2O_5, $Nb_3(PO_4)_5$, SBA-15 and γ-Al_2O_3. A small pore size distribution is observed for SBA-15, which was expected due to its ordered mesoporosity. These pore size distributions were estimated with a Gaussian fit, providing the mean and standard deviation values shown in table 3.
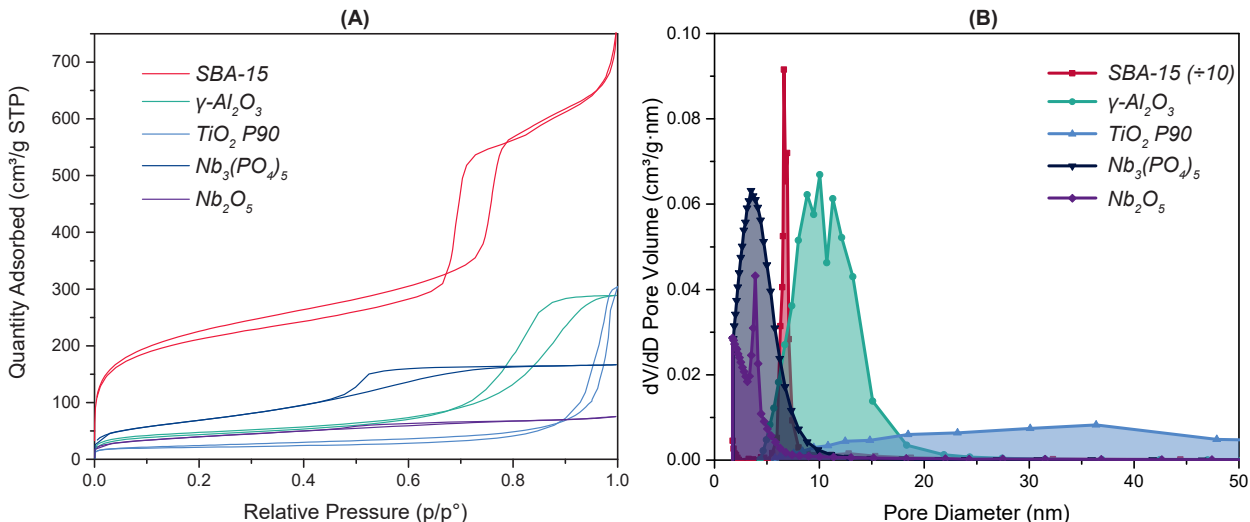
Figure 16: In (A), physisorption isotherms are shown for all scaffolds used for $LiNO_3$ melt infiltrations. Their BJH pore size distributions are shown in (B), with the values for SBA-15 divided by a factor 2 for clarity.

Scaffold	Pore diameter (nm)	BET surface area ($m^2\,g^{-1}$)	Pore volume ($cm^3\,g^{-1}$)
SBA-15	6.7 ± 0.3	787	1.14
γ-Al_2O_3	11.1 ± 2.8	172	0.45
TiO_2 P90	60.8 ± 32.4	87	0.47
$Nb_3(PO_4)_5$	4.1	255	0.26
Nb_2O_5	3.6 ± 1.2	143	0.12

Table 3: Tabuled physisorption data on various scaffolds used for $LiNO_3$ melt infiltrations

Scaffold	PZC	Pyridine FT-IR		NH$_3$-TPD		
		BAS (µmol/g)	LAS (µmol/g)	BAS+LAS (µmol/g)	T$_1$ (°C)	T$_2$ (°C)
SBA-15	4 - 5[27]	-	-	86	330 ± 23	435 ± 74
γ-Al$_2$O$_3$	7 - 9[29]	-	49	624	174 ± 23	350 ± 86
TiO$_2$ (P90)	5 - 6[32]	-	120	644	196 ± 46	436 ± 77
Nb$_3$(PO$_4$)$_5$	< 7[33]	126	99	1820	213 ± 52	341 ± 61
Nb$_2$O$_5$	< 7[33]	55	108	729	180 ± 31	308 ± 73

Table 4: Quantitative results for amounts of Brønsted and Lewis acid sites (BAS and LAS) on various scaffold surfaces as determined with pyridine FT-IR and NH$_3$-TPD, together with mean desorption temperatures and their standard deviations as obtained from NH$_3$-TPD. Furthermore, scaffold PZC values from literature are listed to provide information on overall acidity or basicity of the scaffolds.

4.2.2   Presence of acid sites

These scaffolds are not only different in terms of their porosities, but also in terms of their chemical nature. An important characteristic in this respect is the presence of Brønsted and/or Lewis acid sites on the scaffold. From literature, it is known that γ-Al$_2$O$_3$ contains strong Lewis acid sites, TiO$_2$ P90 contains weaker Lewis acid sites,[37] and Nb$_2$O$_5$ and Nb$_3$(PO$_4$)$_5$ contain both strong Brønsted and Lewis acid sites.[33,47,67] To obtain more information on the effect of these acid sites on the LiNO$_3$ nanocomposite conductivities, they were investigated using pyridine FTIR and NH$_3$-TPD. Both techniques can probe the amount and strength of acid sites on the scaffolds. However, unlike NH$_3$-TPD, pyridine FT-IR can distinguish between Lewis and Brønsted acid sites.

Although the focus of this work is on the presence of acid sites, it is important to keep in mind that these scaffolds also contain Lewis or Brønsted basic sites. An important parameter in this respect is the point of zero charge (PZC) of a material, which gives an indication on whether a scaffold is primarily acidic or basic in nature. The PZC values found in literature for the scaffolds are summarized in table 4. To probe the basic sites of the scaffolds, other techniques like CO$_2$ FT-IR could be used.[68]

Investigation of acid sites with Pyridine FT-IR

To probe the Lewis and Brønsted acid sites of the scaffolds, pyridine FT-IR was performed. The results are shown in figure 17A for wave numbers ranging from $1350 - 1700$ cm^{-1}. As described in the theory section, three spectral regions are of main interest.

The first region of interest is the one around 1545 cm^{-1}. If pyridine is protonated by Brønsted acid sites, its ring vibrations will give rise to absorption at these wave numbers. From figure 17A, it is clear that SBA-15, γ-Al$_2$O$_3$ and TiO$_2$ P90 have no peak here, and therefore these scaffolds do not contain any Brønsted acidity. On the other hand, Nb$_3$(PO$_4$)$_5$ and Nb$_2$O$_5$ do have a peak in this region, with the one of Nb$_3$(PO$_4$)$_5$ being more pronounced. These two peaks were integrated, giving an indication on the amount of Brønsted acid sites present on both scaffolds. The results are given in table 4.

The second spectral region, ranging from about $1600 - 1628$ cm^{-1}, can be related to pyridine molecules coordinated to a Lewis acid site. A larger Lewis acid site strength corresponds to larger wave numbers. Since SBA-15 does not show a peak in this region, it does not have any Lewis acid sites. γ-Al$_2$O$_3$ shows a double degenerate peak at the highest wave number (1619 cm^{-1}), indicating the presence of two Lewis acid sites that differ in chemical environment and strength. The other scaffolds display peaks at similar wave numbers (~ 1608 cm^{-1}), indicating no clear differences in LAS strength.

Lastly, the spectral peak around 1455 cm^{-1} provides a quantitative estimate on the amount of Lewis acid sites present on the scaffold surface. Again, SBA-15 does not show a peak in this region, indicating the absence of any Lewis acid sites on this scaffold. The other scaffolds do show peaks in this region. These peaks were integrated, providing quantitative results on the amount of Lewis acid sites present on the scaffold surfaces, as given in table 4.
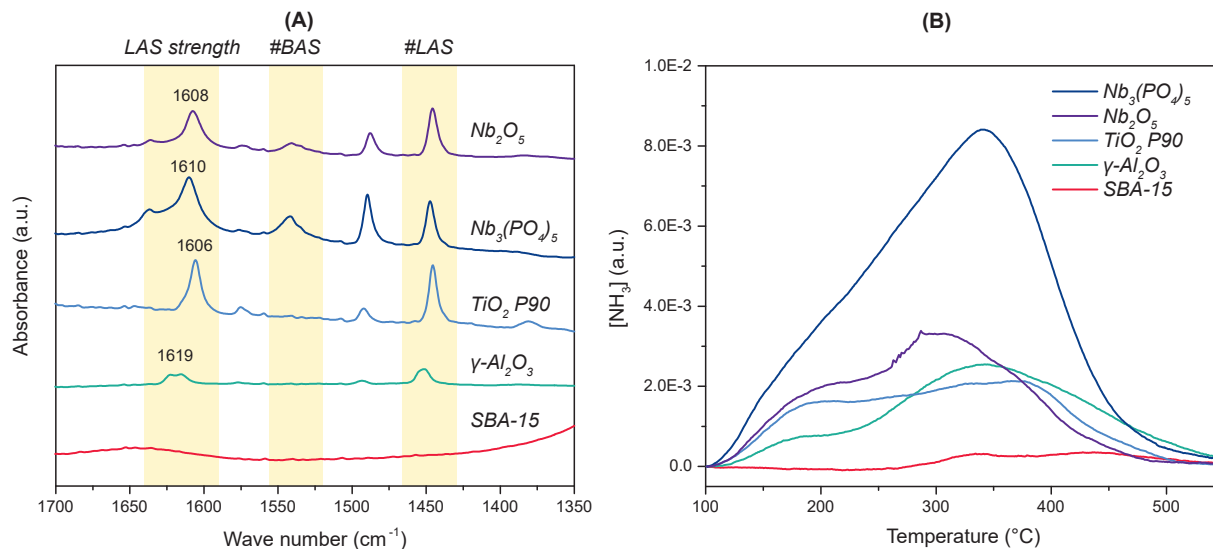
Figure 17: (A) Pyridine FT-IR spectra ranging from $1350 - 1700$ cm^{-1} of various metal oxide scaffolds. Absorbance values are corrected for the weight (mg) of sample in each wafer. (B) Results from NH$_3$-TPD measurements on various metal oxide scaffolds. The amount of adsorbed NH$_3$ is corrected for the weight of sample (mg) after a baseline subtraction.

Investigation of acid sites with NH$_3$-TPD

As a second measure for the presence of acid sites on the scaffolds, NH$_3$-TPD was performed. Although this technique does not distinguish between Brønsted and Lewis acid sites, it does provide quantitative data on the amount of acid sites, as well as providing an indication on their strength.

Information on acid site strength can be inferred from the desorption temperatures, shown in figure 17B and given in table 4. These values indicate that SBA-15 has the strongest acid sites, followed by TiO$_2$ P90, Nb$_3$(PO$_4$)$_5$, γ-Al$_2$O$_3$ and Nb$_2$O$_5$. This result for SBA-15 can be questioned due to its low signal. Furthermore, this trend is different from the one found with pyridine FT-IR. In literature, these results are explained by the weak acidic character of the silica surface hydroxyl groups, causing them to be often mischaracterized as being non-acidic. Apparently, only the NH$_3$ molecule coordinates to these groups, whereas the pyridine molecule does not.[69]

Quantitative data were obtained from deconvolution of the measured TCD concentration versus time (graph not shown here). The results are summarized in table 4. When compared to the results of pyridine FT-IR, it is clear that the NH$_3$-TPD measured values are all much higher. This can partly be explained by the smaller size of NH$_3$ as compared to pyridine, allowing it to better access any acid sites present in the scaffold micropores. Furthermore, this allows multiple NH$_3$ molecules to bind to closely located acid sites, whereas the pyridine molecule might be too large to make this distinction. Furthermore, it might be possible that some diffusion or re-adsorption effects, or small measurement errors cause an overestimation for NH$_3$-TPD results. Naturally, measurements errors might be present in the pyridine FT-IR results as well. Nevertheless, the quantitative results from NH$_3$-TPD and pyridine FT-IR are in general agreement in the sense that they show the same trend from least to most acid sites: SBA-15, γ-Al$_2$O$_3$, TiO$_2$ P90, Nb$_2$O$_5$, Nb$_3$(PO$_4$)$_5$.

4.3   LiNO₃ nanocomposites

Melt infiltration of LiNO$_3$ was performed in the five scaffolds that were characterized in the previous section. This section will describe the results obtained for characterization of the nanocomposites, in terms of pore infiltration, stability of LiNO$_3$ and nanocomposite conductivity. The techniques used for this purpose were DRIFTS, DSC, XRD and EIS, the results of which will be discussed in the following sections.

4.3.1   Investigation of pore filling and LiNO₃ stability with DRIFTS

As a first indication on whether the melt infiltrations of LiNO$_3$ had been successful, DRIFTS was employed. The DRIFTS results of the bare scaffolds, pure LiNO$_3$ and the nanocomposites at 130% pore filling are shown in figure 18.

The characteristic LiNO$_3$ bond vibrations between $2000 - 3000$ cm^{-1} provide information on the stability of LiNO$_3$ during melt infiltration. Since these vibrations are still present in all nanocomposites, there is no indication on any chemical conversion. Furthermore, no vibrations can be observed in the nanocomposite spectra which were not present in those of the pure compounds. This indicates that LiNO$_3$ was stable during all melt infiltrations and no chemical reactions took place. These results are in line with the results for heat treatment of LiNO$_3$ in the absence of any scaffolds.

The intensity of the characteristic LiNO$_3$ bond vibrations between $2000 - 3000$ cm^{-1} decreases with respect to that of pure LiNO$_3$, which is most clear in the case of the Nb$_3$(PO$_4$)$_5$ and Nb$_2$O$_5$ nanocomposites. This effect is related to the amount of LiNO$_3$ present in the samples. In the case of these two scaffolds, their pore volumes are small and therefore the relative amount of LiNO$_3$ at 130% pore fillings is small in the nanocomposites as well, causing less intense vibrations.
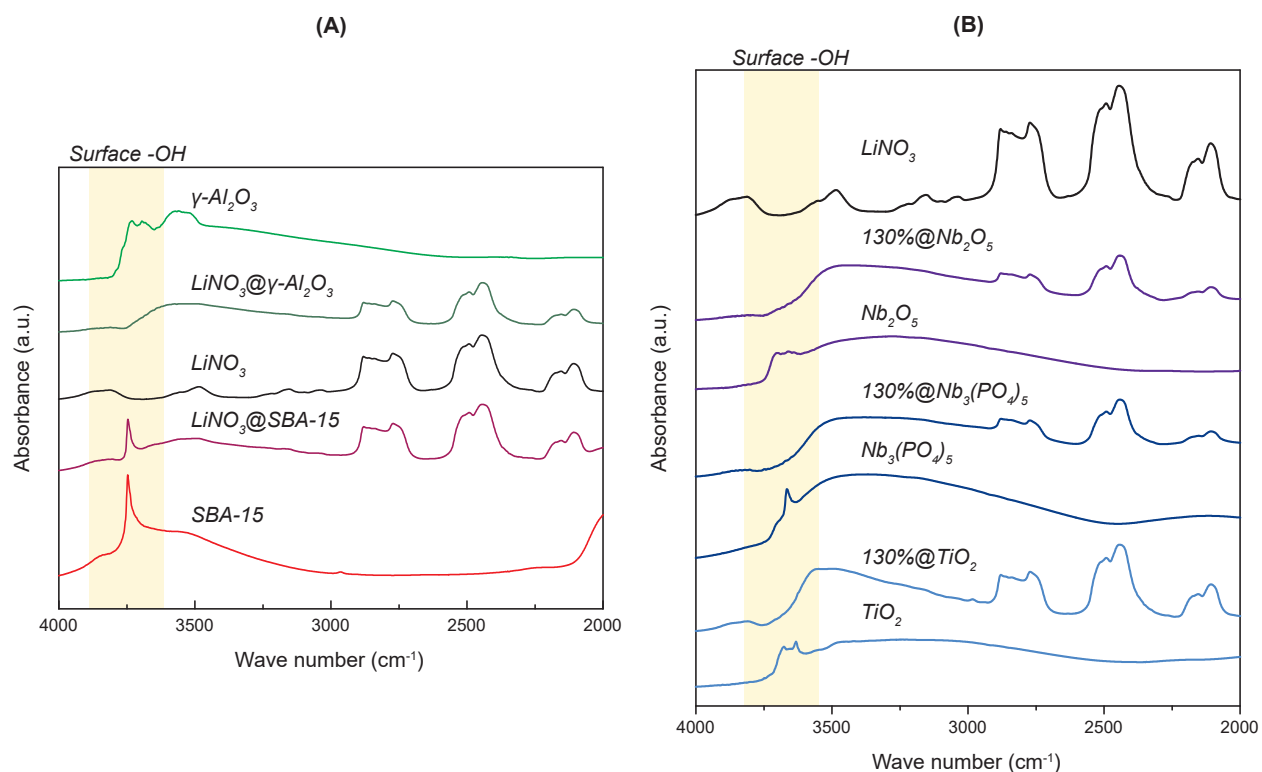
Figure 18: (A) Results obtained with DRIFTS on pure LiNO$_3$, SBA-15 and γ-Al$_2$O$_3$ and in between their combined nano-composites at 130% pore filling. Scaffold surface hydroxyl group vibrations disappear for LiNO$_3$ in γ-Al$_2$O$_3$, but not in SBA-15. (B) Similar results obtained for TiO$_2$ P90, Nb$_3$(PO$_4$)$_5$ and Nb$_2$O$_5$ scaffolds. Each of the nano-composites does not show vibrations between $3500 - 4000$ cm^{-1}, indicating complete pore filling.
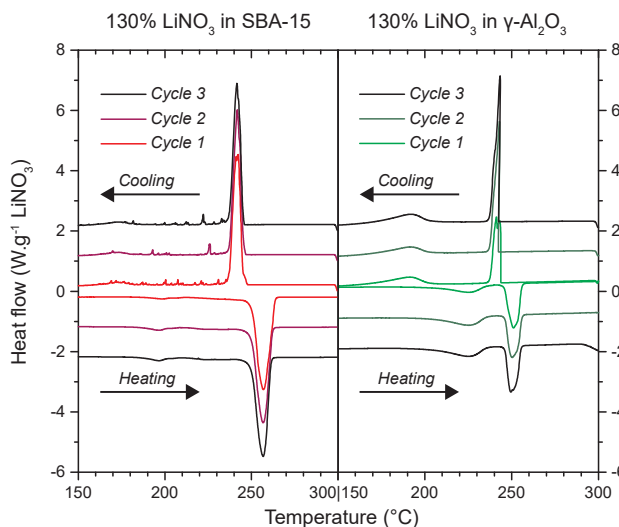
Figure 19: Three heating and cooling cycles of 130% LiNO$_3$ in SBA-15 (red) and in γ-Al$_2$O$_3$ (green) are shown with an offset of $\pm$ 0, 1 and 2, respectively. The γ-Al$_2$O$_3$ nano-composite displays a second peak at lowered temperature, and less bulk peak intensity than the SBA-15 one.

Scaffold	Onset (C)	Pores filled (%)	Inside : outside pores (%)
SBA-15	250	34	25 : 75
γ-Al$_2$O$_3$	246	104	70 : 30
TiO$_2$ P90	235	75	58 : 42
Nb$_3$(PO$_4$)$_5$	250	104	80 : 20
Nb$_2$O$_5$	246	73	56 : 44

Table 5: Degree of pore filling of LiNO$_3$ in all scaffolds, as determined quantitatively with DSC

When LiNO$_3$ has completely infiltrated the scaffold pores, the vibrations of hydroxyl groups ($-$OH, $3500 - 4000$ cm^{-1}) present on the scaffold surfaces will be blocked, causing the intensity of these bond vibrations to be quenched. Indeed bond vibrations in this spectral region can be observed for all bare scaffolds, confirming the presence of surface hydroxyl groups. Furthermore, these vibrations cannot be observed in the DRIFTS spectra of all nanocomposites, expect for the LiNO$_3$ in SBA-15 one. This suggests that complete pore filling of LiNO$_3$ was achieved in all scaffolds, expect for in SBA-15.

Although the DRIFTS results already suggest that melt infiltration of LiNO$_3$ was successful in all scaffolds, except for SBA-15, it is important to corroborate these results with a technique complementary to DRIFTS. For this purpose, the next section will describe results obtained with DSC measurements.

4.3.2 Investigation of pore filling and LiNO$_3$ stability with DSC

To obtain more information on the thermal stability of LiNO$_3$ and infiltration of the scaffold pores, DSC measurements were performed on all nanocomposites at 130% pore filling. With DSC, the melting behaviour of LiNO$_3$ is measured, which is affected by nanoconfinement. Therefore, with this technique it is possible to distinguish between LiNO$_3$ inside and outside of the scaffold pores. The results of DSC measurements are shown in figure 19 for SBA-15 and γ-Al$_2$O$_3$, and in figure 20 for the other nanocomposites. Table 5 provides the onset temperatures related to melting. In all graphs, no significant differences between each of the different heating and cooling cycles can be observed. This shows that LiNO$_3$ is stable upon heating, similar to what was found for pure LiNO$_3$ in the absence of any scaffolds.

The DSC results for the nanocomposites can be compared to the results shown in figure 14A for pure LiNO$_3$. Again, melting of bulk LiNO$_3$ occurs around 255 °C and recrystallization occurs at slightly lower temperatures for all nanocomposites. This bulk LiNO$_3$ is not nanoconfined, as nanoconfinement would effect
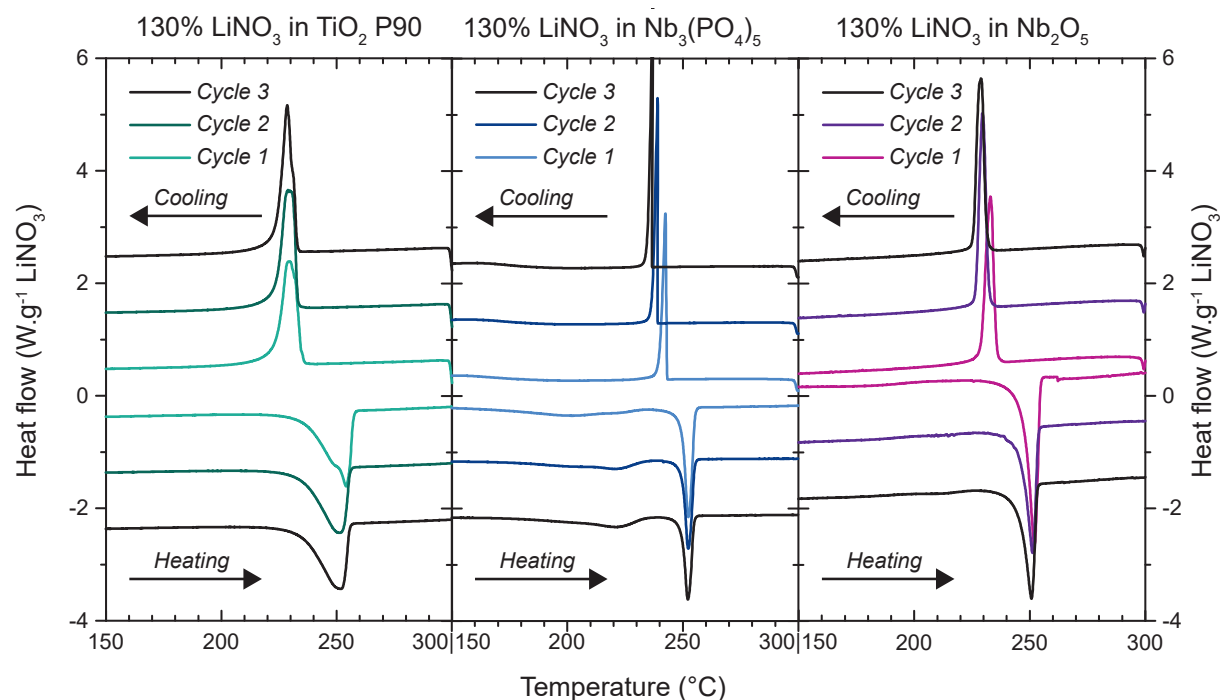
37

Figure 20: Three heating and cooling cycles of 130% $LiNO_3$ in TiO_2 P90 (green), $Nb_3(PO_4)_5$ (blue) and Nb_2O_5 (purple). Each next cycle is plotted with an offset of $\pm$ 1.

its melting behaviour, and therefore present outside the pores of the scaffolds.

Especially in the case of $LiNO_3$ in γ-Al_2O_3, secondary melting and crystallization events are visible at lower temperatures. These events can be related to intra-porous $LiNO_3$, which have a depressed melting point due to nanoconfinement. Such secondary peaks are present in the SBA-15 nanocomposite as well, but with much less intensity. This suggests some pore filling, but not as much as in γ-Al_2O_3.

Of the other three nanocomposites in figure 20, only the $LiNO_3$ in $Nb_3(PO_4)_5$ one clearly shows such a second peak, around 225 °C. This peak is broad and not intense, making it difficult to discern. For the $LiNO_3$ in Nb_2O_5 nanocomposite, no secondary melting peak which can be related to nanoconfined material can be observed at all. It is likely that these peaks are not clearly visible due to the relatively small amount of $LiNO_3$ present in the samples. It can be argued that melting point depression takes place in the $LiNO_3$ in TiO_2 P90 nanocomposite as well, since the onset temperatures related to melting are lowered with respect to that of pure $LiNO_3$. Furthermore, these three peaks seem to be broadened with respect to the other samples. This suggests two differing melting behaviours, which is clear from the first melting peak containing two minima. It is likely that melt infiltration has taken place here, but did not cause a strong enough melting point depression to clearly separate the nanoconfined and bulk $LiNO_3$ melting behaviours. This is probably caused by the relatively large pores of the TiO_2 P90 scaffold with a broad pore size distribution, as was shown in figure 16.

Beside these qualitative interpretations of the DSC results, it is possible to perform quantitative analysis on the negative peaks that correspond to melting of bulk $LiNO_3$. By integration of these peaks, together with the measured bulk enthalpy of -387 J g^{-1}, the amount of extra-porous or bulk-like $LiNO_3$ can be calculated. Subtracting this from the total amount of $LiNO_3$ present in the sample yields the amount of intra-porous $LiNO_3$. With this approach, it is possible to calculate how much of the pore volume is filled after melt infiltration. For $LiNO_3$ in TiO_2 P90, this was complicated by the overlap in bulk and nanoconfined $LiNO_3$ melting behaviours. Therefore, the peaks were deconvoluted by approximation with two Gaussian fits in the Origin9.1 program. The results are summarized in table 5.

From these quantitative results, it follows that in the SBA-15 nanocomposite, only 34% of the pores was filled, in contrast to the 104% obtained in the case of γ-Al_2O_3 and $Nb_3(PO_4)_5$. In the other two nanocomposites,
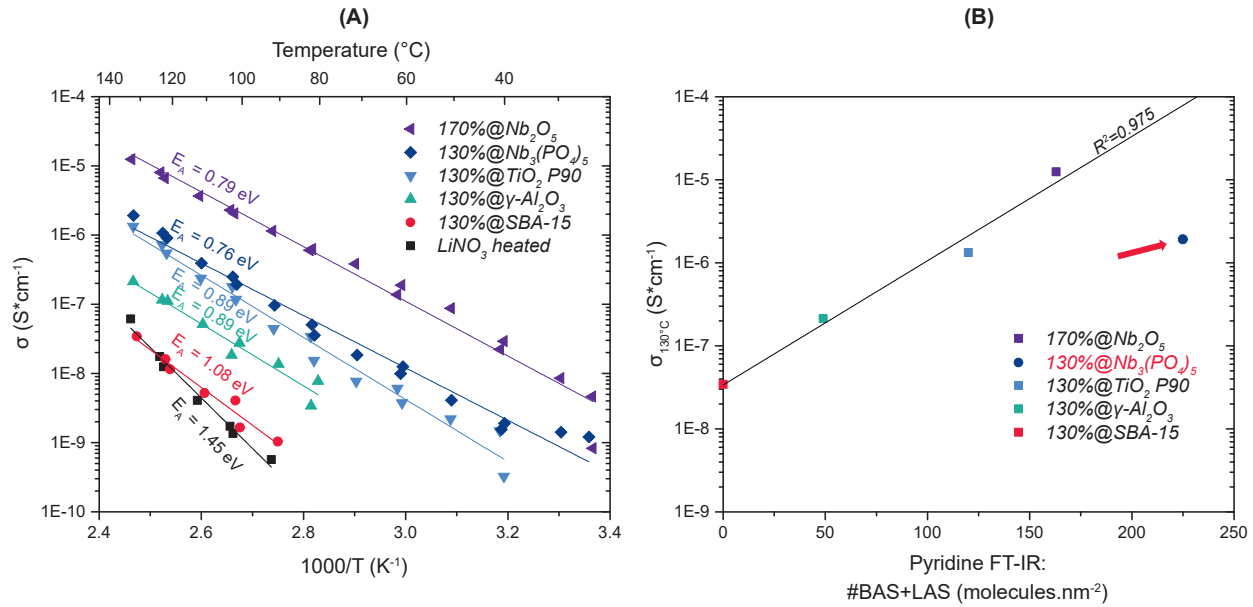
Figure 21: (A) Results of conductivity measurements on heated $LiNO_3$ and all nanocomposites at 130% pore filling (170% in Nb_2O_5). The scaffolds used are in order of increasing conductivity: SBA-15, γ-Al_2O_3, TiO_2 P90, $Nb_3(PO_4)_5$ and Nb_2O_5, accompanied by a decrease in activation energy. (B) The nanocomposite conductivities as function of the total amount of acid sites as determined with pyridine FT-IR.

only about 75% of the pores is filled. For TiO_2 P90, this determined value might be less than 100% due to the two overlapping melting peaks. Furthermore, it is probable that the measured degree of pore filling in TiO_2 P90 and Nb_2O_5 are lower than expected due to the presence of macropores in these scaffolds. When these macropores are too large to affect the melting behaviour of $LiNO_3$ due to nanoconfinement, intra-porous $LiNO_3$ will contribute to the observed bulk melting peak and causing an underestimation of the amount of intra-porous $LiNO_3$.

Upon combination of these DSC results with the DRIFTS results shown before, we conclude that $LiNO_3$ is stable upon heat treatment and successfully infiltrated the pores of all scaffolds at least to a significant amount, except for those of SBA-15.

4.3.3 Conductivity of LiNO₃ nanocomposites

The conductivity of all nanocomposites was determined with EIS. The results are shown in figure 21A, together with the conductivity of heated $LiNO_3$ for comparison. Both the height and slope of the graphs are important, giving the conductivities and related activation energies of the materials.

From figure 21A, it is clear that the conductivity of heated $LiNO_3$ at room temperature is lower than that of all nanocomposites. Therefore, melt infiltration successfully raises the conductivity of $LiNO_3$ in the case of all scaffolds. Together with this increase in conductivity, a decrease in activation energy is observed for all nanocomposites as compared to heated $LiNO_3$.

These effects of increasing conductivity and decreasing activation energy differ in magnitude for the various scaffolds used. The nanocomposite containing SBA-15 has the lowest conductivity and activation energy. This can be rationalized by the DRIFTS and DSC results presented before, which showed that $LiNO_3$ does not infiltrate into all SBA-15 pores. We can conclude that nanoconfinement of $LiNO_3$ is important for successfully enhancing its conductivity.

From figure 21A, it can be deduced that pore filling is not the only factor in conductivity enhancement of $LiNO_3$. Whereas pore filling was observed for $LiNO_3$ in γ-Al_2O_3, TiO_2 P90, $Nb_3(PO_4)_5$ and Nb_2O_5, these nanocomposites all have different conductivities. The order of increasing conductivity is approximately the same as that of decreasing activation energy: γ-Al_2O_3, TiO_2 P90, $Nb_3(PO_4)_5$ and Nb_2O_5.

To understand what causes these differences between the nanocomposites, the properties of the various

scaffolds should be evaluated. Two main differences can be appointed. The first is related to the porous properties of the scaffolds, which were discussed in section 4.2.1. From literature, it is known that the morphology and size of the pores indeed plays an important role.[24] However, this difference alone cannot explain why LiNO$_3$ does not enter the pores of SBA-15, whereas it does enter the pores of all other scaffolds. A second difference between the scaffolds is related to the chemical nature of their surfaces, which was discussed in section 4.2.2. Since the interaction between the infiltrate and the scaffold is important for successful melt infiltration and wetting,[24] as well as for LiBH$_4$ nanocomposite conductivity,[19] this was investigated further. In terms of chemical nature, an important difference between SBA-15 and the other scaffolds is the presence of Lewis acid sites on their surfaces, as was determined by pyridine FT-IR and NH$_3$-TPD in section 4.2.2. Indeed, the order of increasing Lewis acid sites on the scaffold surfaces, summarized in table 4, is similar to that of increasing conductivity of the nanocomposites: SBA-15 < γ-Al$_2$O$_3$ < TiO$_2$ P90. The other two scaffolds, Nb$_3$(PO$_4$)$_5$ and Nb$_2$O$_5$, deviate from this trend in the sense that their corresponding nanocomposites have higher conductivities. It is likely that these deviations are caused by the presence of Brønsted acid sites on their surfaces. Indeed, when the sum of Lewis and Brønsted acid sites is taken into account, a linear correlation is found between the number of acid sites of the scaffolds and the conductivities of their nanocomposites, as shown in figure 21B.

In figure 21B, the total amount of acid sites as determined with pyridine FT-IR are shown, whereas the results of NH$_3$-TPD are neglected since they show a worse correlation. This might indicate that the correlation between nanocomposite conductivity and amount of acid sites is less strong than what is suggested in figure 21B. Another explanation for the deviating NH$_3$-TPD results could be that these measurements were not performed accurately. However, it is most likely that these deviations are caused by the fact that the NH$_3$ molecule is smaller, and binds stronger and less specifically to acid sites on the scaffold surfaces. It is possible that the NH$_3$ molecule probes acid sites that are too weak to interact with the LiNO$_3$ infiltrate, and that these acid sites therefore do not have an effect on the nanocomposite conductivities.

Another discrepancy in figure 21B is the deviating conductivity of the Nb$_3$(PO$_4$)$_5$ nanocomposite, which is circa two orders of magnitude lower than expected from this linear correlation. One explanation is that the interaction between LiNO$_3$ and Nb$_3$(PO$_4$)$_5$ is too strong, and there is actually an optimum in amount of acid sites. Murayama et al. [33] report that indeed the Nb$_3$(PO$_4$)$_5$ scaffold contains more and stronger Brønsted acid sites than the Nb$_2$O$_5$ one. Another explanation could be related to the phosphate instead of oxide anions on the scaffold. Upon measuring the nanocomposite conductivity with EIS, a pellet is pressed in between two pieces of metallic Li foil. It is possible that this metallic Li reacts at the interface with the scaffolds. However, when TiO$_2$ P90 and Nb$_2$O$_5$ are (partially) reduced, a semiconducting compound is formed with electronic conductivity. This might actually help in establishing a good electric contact between the Li foil and the nanocomposite pellet. However, when Nb$_3$(PO$_4$)$_5$ is (partially) reduced, an interfacial layer of partially reduced phosphate anions might form, which can have a resistive or blocking effect. Perhaps such a layer is formed, and increases the pellet resistance, thereby decreasing the measured conductivity.

Irrespective of the cause for the lower conductivity of the Nb$_3$(PO$_4$)$_5$ nanocomposite than expected, a correlation between the LiNO$_3$ nanocomposite conductivities and the presence of both Lewis and Brønsted acid sites on the scaffold surfaces is clear. These acid sites help in establishing a favourable interaction between LiNO$_3$ and the scaffold, which is essential for wettability and successful successful pore infiltrations, as well as for enhancing conductivities. This illustrates the importance of tuning surface interactions when performing melt infiltrations as a way to increase the conductivity of LiNO$_3$.

5 Results and discussion: LiNH₂ nanocomposites

In this master thesis, the effect of nanoconfinement on the conductivity of two different lithium salts was tested: LiNO₃ and LiNH₂. This section will discuss the results obtained for LiNH₂ nanocomposites.

5.1 Heat treatment of LiNH₂

A LiNH₂ nanocomposite is obtained using melt infiltration of LiNH₂. This section will describe the stability of LiNH₂ in the absence of a scaffold during synthesis. Furthermore, the effect of melting and recrystallization on the conductivity of LiNH₂ will be discussed.

5.1.1 Stability of LiNH₂ under heat treatment

The stability of LiNH₂ upon heating up to its melting point was investigated with DSC measurements. The results are shown in figure 22A. No phase transition or reaction occurs up to about 340 °C, since a straight line is observed. However, a peak with an onset temperature of about 367 °C indicates melting of LiNH₂. These onset temperatures are provided in table 6, being lower than the melting point of 390 °C reported by the supplier and in literature.[70] This might indicate the onset of another endothermic event, like thermal decomposition of LiNH₂. Recrystallization upon cooling occurs at even lower temperatures, but this is related to a kinetic delay. A cooling rate lower than the applied 5 °C min⁻¹ might reduce this delay. Some noise is observed at temperatures above the melting point of LiNH₂. This is likely to be caused by a bad contact of the sample with the edges of the DSC cup. A possible explanation is either too much or
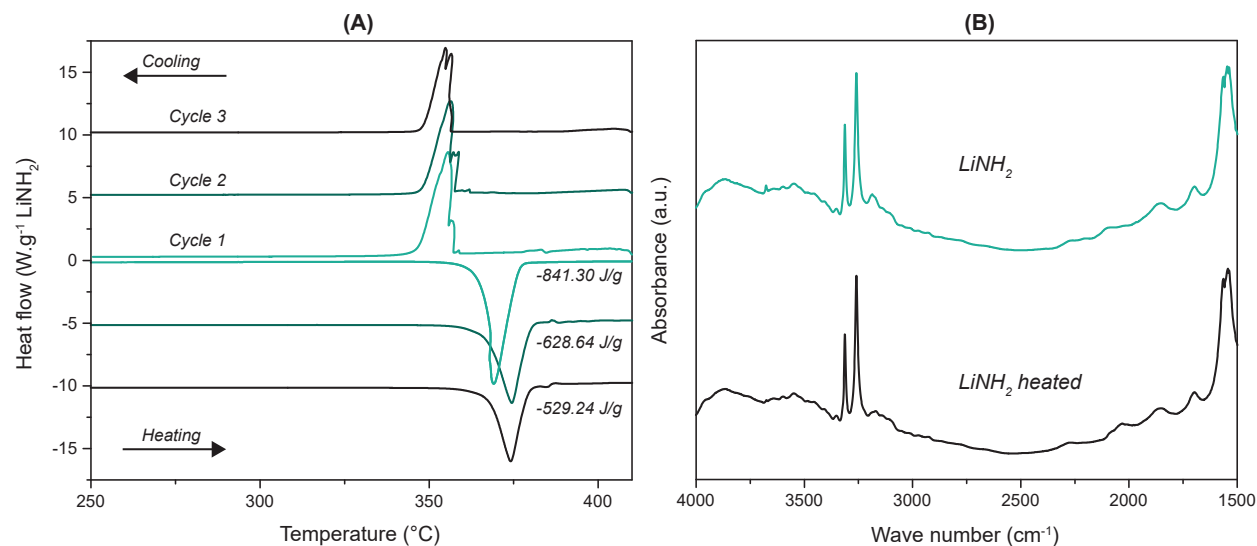
Figure 22: (A) Results from DSC measurements on pure LiNH₂, with three heating cycles from inside to outside (light green to black) plotted with respective offsets of 0, 5 and 10 W g⁻¹ LiNH₂ in the relevant temperature range. The second and third heating peaks were integrated, giving the enthalpy values shown in the graph. In (B), DRIFTS results are shown on LiNH₂ before and after heating.

Cycle	Onset (°C)	Enthalpy (J g⁻¹)
1	-	-841.3
2	366.9	-628.6
3	367.7	-529.2

Table 6: Tabulated results from DSC measurements on melting of pure LiNH₂. The melting peak of cycle 1 could not be integrated with the STARe software, and was integrated with Origin9.1 instead.

(A)

(B)
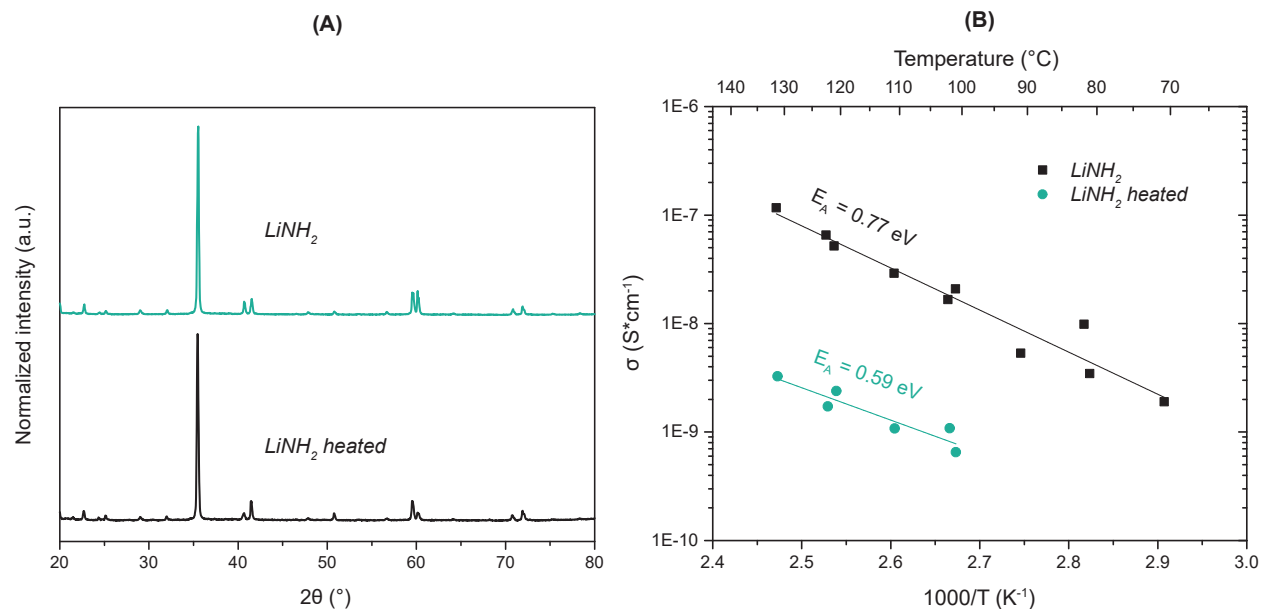
Figure 23: In (A), XRD results on $LiNH_2$ before and after heating are shown. Clear differences are only observed in the relative ratios between the two peaks at 41° and 42° and those at 60°. Conductivity results from EIS measurements are shown in (B), indicating a decrease both in conductivity and activation energy after melting and recrystallization.

too less sample in the cup, but in this case noise would be observed at lower temperatures as well. Another explanation is a chemical reaction of $LiNH_2$, which induces loss of sample and formation of NH_3 gas.[71] This was investigated by quantitative analysis of the three melting peaks. The corresponding enthalpies are listed in table 6. Their values decrease upon cycling, confirming a gradual loss of $LiNH_2$ in the sample. This thermal decomposition of $LiNH_2$ is in agreement with the articles by Zhang and Hu [71] and Bramwell et al. [72], who suggest a corresponding formation of Li_2NH and NH_3 gas:

$$2LiNH_2 \rightarrow Li_2NH + NH_3 \tag{16}$$

$$\Delta H = 84.1 \text{ kJ/mol } NH_3$$

5.1.2 Characterization of heated $LiNH_2$

Heat treatment of $LiNH_2$ was performed under NH_3 atmosphere in an effort to shift the chemical equilibrium and suppress thermal decomposition of $LiNH_2$. To establish whether thermal decomposition of $LiNH_2$ was successfully suppressed, the heated product was characterized with DRIFTS and XRD.

Figure 22B for $LiNH_2$ shows DRIFTS spectra of $LiNH_2$ before and after heat treatment. Both spectra are identical, indicating that the chemical structure of $LiNH_2$ is preserved and no new chemical compounds are formed. A doubly degenerate peak around 3300 cm^{-1} can be observed, which is related to the two N–H stretch vibrations which are slightly offset in energy due to Fermi resonances.[73] Furthermore, a doubly degenerate peak is visible around 1600 cm^{-1}, which can be related to N–H bending vibrations.[73] The ratios between the peaks are similar in both spectra, giving no indication that the suggested decomposition product Li_2NH is formed.[71]

Similarly, XRD patterns of $LiNH_2$ before and after heat treatment are shown in figure 23A. Both spectra are similar, each showing peaks at diffraction angles 2θ that correspond to the values of $LiNH_2$ reported in literature.[74] Furthermore, the peak at around 36° is most intense for both compounds, indicating a preferred orientation in this (hkl = 111) direction. However, ratios between the various diffraction peaks are different. For example the two adjacent peak pairs around 42° and 60° have similar intensities before heating $LiNH_2$, but a more intense right and left peak after heating, respectively. These intensity differences are actually

in line with the reference diffraction pattern reported by Yang et al. [74]. However, it is also possible that some Li$_2$NH was formed, since it has diffraction peaks at similar diffraction angles as LiNH$_2$. For this same reason, it is difficult to determine its presence with certainty.[74,75] However, peak broadening would be expected in this case, since the Li$_2$NH diffraction peaks at 42° and 60° are positioned exactly in between the diffraction peak pairs of LiNH$_2$. Since this is not the case, and combined with the identical DRIFTS spectra, we conclude that little to no decomposition of LiNH$_2$ has taken place, and applying NH$_3$ pressure suppresses its thermal decomposition.

5.1.3   Effect of heat treatment on conductivity LiNH$_2$

It was shown that LiNH$_2$ is stable during heat treatment under NH$_3$ pressure. To investigate whether the conductivity of LiNH$_2$ changes after melting and recrystallization, EIS measurements were performed. The results are shown in figure 23B.

Clear differences between LiNH$_2$ before and after heat treatment can be observed, with both the conductivity and activation energy decreasing upon heat treatment. This is true for extrapolation of these conductivities to room temperature as well, yielding values of $3.9 \cdot 10^{-11}$ S cm^{-1} and $7.3 \cdot 10^{-12}$ S cm^{-1} for LiNH$_2$ before and after heating, respectively. However, it should be taken into account that these activation energies and conductivities are not precise since few measurement points were taken, in the low sensitivity region of the EIS apparatus.

Note that these results are in contrast to the results obtained for LiNO$_3$, which showed both a conductivity and activation energy increase after heat treatment. A possible explanation for the change in conductivity upon heat treatment might be a structural change induced by melting and recrystallization, which can be viewed as an annealing process. As was discussed in theory section 2.1, the presence of solid-solid interfacial regions and defects are essential for improved conductivities. It is possible that this annealing removes defects and stress by restructuring the solid,[76] thereby lowering the amount of mobile charge carriers.[23] Further investigation with for example quantitative XRD should be performed to obtain more information on this effect.

5.2   Characterization of scaffolds used for LiNH₂ melt infiltrations

Melt infiltration of LiNH₂ was performed in the following scaffolds: SBA-15-NH₂, SBA-15, γ-Al₂O₃, γ-AlO(OH) and MgO. Note here that reducible scaffolds like TiO_2 P90, $Nb_3(PO_4)_5$ and Nb_2O_5 could not be used as LiNH₂ is a reducing agent. The porosity of these scaffolds was characterized using N₂-physisorption, whereas the presence of surface hydroxyl groups was confirmed using DRIFTS.

Scaffold porosities

Adsorption and desorption isotherms of the scaffolds are shown in figure 24A, with the single point adsorption at $p/p° = 0.995$ giving the total pore volume of the materials. These values are summarized in table 7. Figure 24B gives the BJH pore size distributions of the scaffolds, showing that the pore diameters are all smaller than 12 nm. These BJH pore size distributions were approximated with a Gaussian fit, giving the average values and standard deviations as given in table 7. SBA-15, MCM-41 and SBA-15-NH₂ have small pore size distributions due to their ordered mesoporosity, whereas the other scaffolds have larger pore size distributions. Table 7 provides the BET surface areas of the scaffolds as well. From these results, it follows that grafting of the SBA-15 surface with APTES molecules has significantly reduced the porosity of the scaffold. Lastly, table 7 again provides the PZC and surface group density values, which were discussed in theory section 2.3.
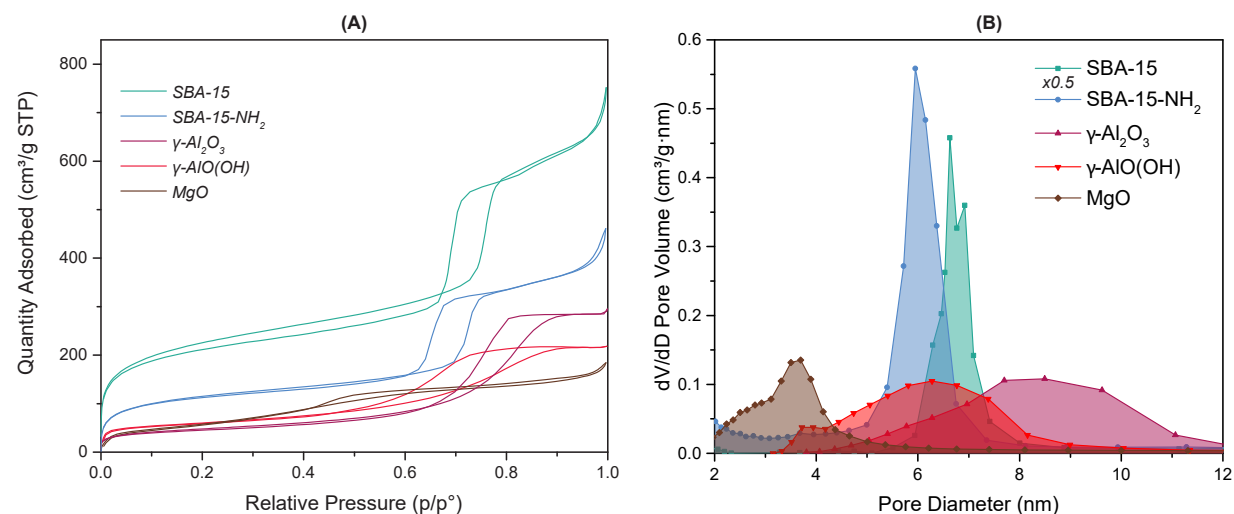
Figure 24: (A) Physisorption isotherms of all scaffolds used for LiNH₂ melt infiltrations. (B) BJH pore size distributions of the scaffolds. The values for SBA-15 are divided by a factor 2 for clarity.

Scaffold	Pore diameter (nm)	BET surface area (m² g⁻¹)	Pore volume (cm³ g⁻¹)	PZC	OH density (molecules nm⁻²)
SBA-15-NH₂	6.1 ± 0.3	401	0.63	8 - 9[27]	2.6[28]
SBA-15	6.7 ± 0.3	787	1.14	4 - 5[27]	7.7[28]
γ-Al₂O₃	8.7 ± 1.6	173	0.46	7 - 9[29]	11.5[28]
γ-AlO(OH)	6.5 ± 1.2	216	0.34	7 - 8[30]	-
MgO	3.6 ± 0.6	252	0.28	12 - 13[35]	16.9[28]

Table 7: Overview of porous properties of scaffolds used for LiNH₂ melt infiltrations as determined with N₂-physisorption. Furthermore, literature values for PZC and surface hydroxyl group densities are added.
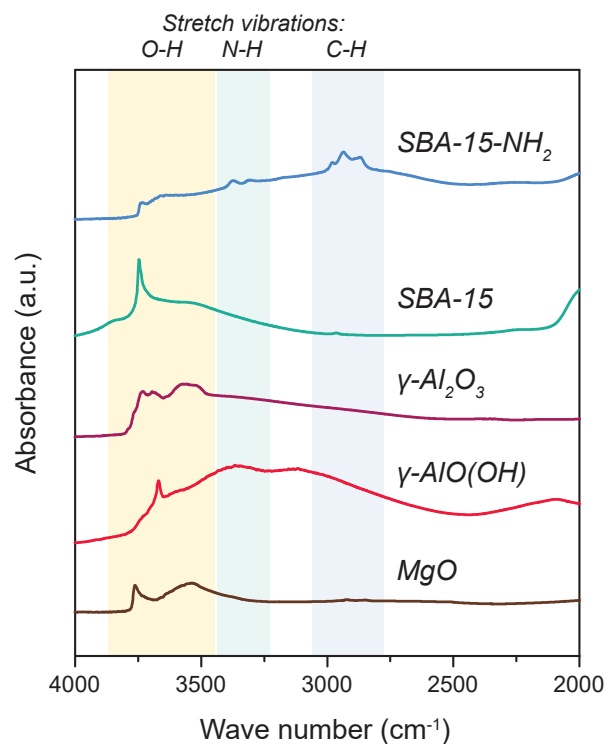
Figure 25: DRIFTS results on all scaffolds used for LiNH$_2$ melt infiltrations, showing the presence of surface hydroxyl groups. Only SBA-15-NH$_2$ does not have these groups, but instead aminopropyl-related vibration modes can be observed.

Scaffold surface groups

The presence of surface groups on the scaffolds was investigated with DRIFTS. The results are shown in figure 25. Except for SBA-15-NH$_2$, all scaffolds contain surface hydroxyl groups with characteristic O−H stretch vibrations around 3750 cm^{-1}. These vibrations can indeed be observed for MgO, γ-AlO(OH), γ-Al$_2$O$_3$ and SBA-15.

The scaffold SBA-15-NH$_2$ was obtained after grafting the SBA-15 surface hydroxyl groups with APTES, as was shown in figure 7. A small peak is present around 3750 cm^{-1}, indicating that not all hydroxyl groups were removed by this grafting reaction. Either more APTES should have been added, or the corresponding isolated silanol groups were not reactive enough to be removed. Either way, surface functionalization has occurred to some extent, since peaks related to the propylamine ligands can be observed. These include C−H stretch vibrations around 2900 cm^{-1} and N−H stretch vibrations around 3300 cm^{-1}.

The effects of these different surface groups on LiNH$_2$ melt infiltrations and nanocomposite conductivities will be investigated in the following sections.

5.3   LiNH₂ nanocomposites

Melt infiltrations of LiNH₂ were performed in all scaffolds mentioned previously. The results for LiNH₂ in SBA-15 will be discussed first, after which results for the other scaffolds will be discussed. Again, DRIFTS and XRD were employed to characterize the nanocomposites in terms of scaffold pore filling and infiltrate stability, followed by conductivity measurements using EIS.

5.3.1   Characterization of LiNH₂ nanoconfined in SBA-15 at different pore fillings

To verify whether LiNH₂ had completely infiltrated the pores of the SBA-15 scaffold, DRIFTS measurements were performed. The results for pure LiNH₂ and SBA-15, as well as their corresponding nanocomposites at various degrees of pore filling (PF), are shown in figure 26A. In the case of complete pore filling, the vibrations of the scaffold surface hydroxyl groups will be blocked, causing the $O-H$ stretch vibrations around 3750 cm^{-1} to disappear. It is clear from this graph that indeed these $O-H$ stretch vibrations gradually disappear with increasing PF, having almost disappeared for the 25% PF and completely disappeared for the 50% PF nanocomposites. The 75% PF nanocomposite also displays a small peak in this region, but this might be caused by an impurity in the pure LiNH₂ as well. Either way, these results indicate that after melt infiltration the scaffold pores are completely filled.

A gradual change can be observed in the two $N-H$ stretch vibrations of LiNH₂ around 3300 cm^{-1}. With decreasing PF, these peaks broaden and their features are lost. A possible explanation for this result is that nanoconfinement leads to different chemical environments for intra-porous and extra-porous LiNH₂, causing a larger spread in bond energies and a broadened peak. Additionally, a spectral shift to higher wave numbers can be observed for the $N-H$ stretch vibrations of the 25% and 50% PF samples. A shift to higher wave numbers corresponds with a shift to higher energies, implying a stronger $N-H$ bond. One explanation for this shift is a chemical reaction between LiNH₂ and the scaffold surface, thereby affecting the energies of the amide $N-H$ bonds. Another explanation could be related to the presence of hydrogen bonds, as is suggested by Long [73]. In his work, he shows that the amide $N-H$ bonds appear at 3350 cm^{-1} and 3200 cm^{-1} in the solid state and in the presence of hydrogen bonding. However, in a liquid state and in the absence of hydrogen bonds, they appear at 3500 cm^{-1} and 3400 cm^{-1}.[73] This suggests that at the interface with the scaffold a more liquid-like structure is formed, where interactions between the LiNH₂ molecules are weakened.

Peak broadening and spectral shifts are not observed for the $N-H$ bending vibrations around 1600 cm^{-1},
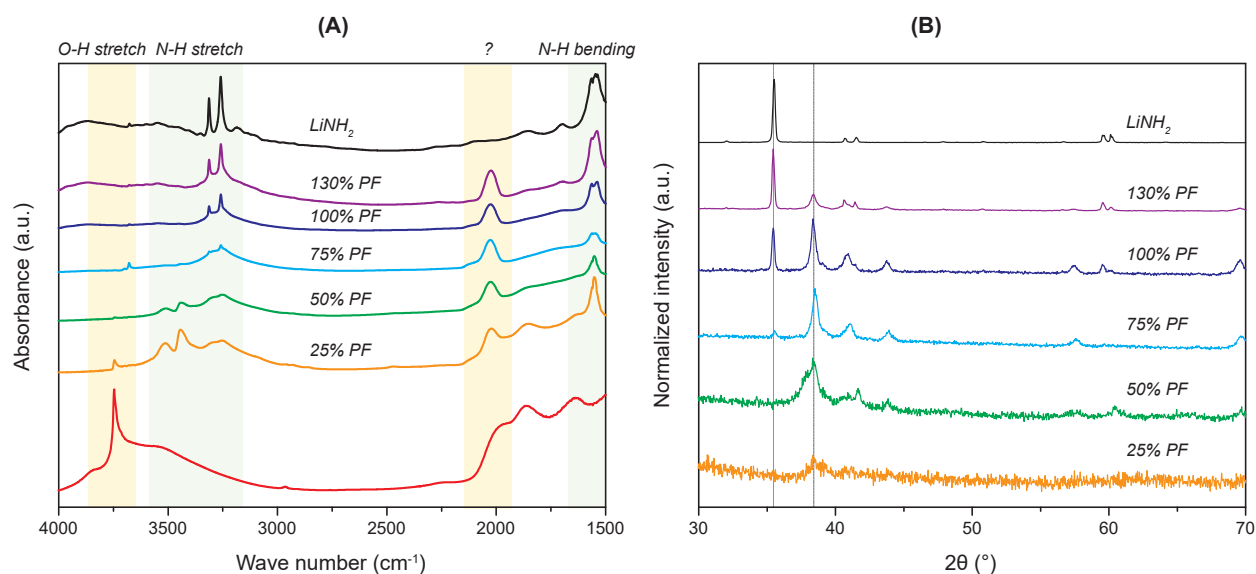

Figure 26: (A) Shows DRIFTS results and (B) shows diffraction peak patterns for the nanocomposites LiNH₂ in SBA-15 at increasing pore fillings.

since the energy of these vibrations is less sensitive to a change in state (~ 20 cm^{-1}).[73]

At 2000 cm^{-1}, a new peak appears in all nanocomposites. This peak cannot be related to the spectra of either pure LiNH$_2$ or pure SBA-15, suggesting that it is caused by the product of a chemical reaction between LiNH$_2$ and the SBA-15 scaffold. Given the simultaneous disappearance of surface hydroxyl group vibrations, it is likely that these groups are involved in the reaction. It should be noted that this reaction is not complete, since the N–H bending vibrations at 1600 cm^{-1} remain visible.

Assigning this peak at 2000 cm^{-1} to a certain chemical bond vibration or reaction product is not straightforward. In literature, few molecular vibrations have been reported to occur within this region.[73] One possibility is the formation of an N–O bond, since the LiNO$_3$ DRIFTS spectrum shows vibrations between $2000-3000$ cm^{-1}. However, this seems unlikely since N–O stretch vibrations are reported to lead to a sharp peak around 1500 cm^{-1}, which is not observed here beside the N–H bending vibrations.[73] Another possibility is the formation of an Si–H bond, which is reported to cause a peak around $2250-2100$ cm^{-1}.[73,77,78] Such silane compounds are prepared commercially by the reduction of gaseous SiO$_2$ with Al under high H$_2$ pressures, in a molten salt mixture of NaCl and AlCl$_3$.[79] Although the reduction of SiO$_2$ requires extreme reaction conditions, it might be possible that the reducing agent LiNH$_2$ does cause some reduction of the scaffold. More extensive characterization is required to confirm this hypothesis. Nevertheless, it is clear that a chemical reaction between LiNH$_2$ and the scaffold takes place.

More information on melt infiltration and the chemical reaction product observed with DRIFTS measurements can be derived from XRD. The XRD patterns of LiNH$_2$ in SBA-15 nanocomposites with various degrees of pore filling are shown in figure 26B. The XRD pattern of the pure SBA-15 scaffold is not shown because it contains only long-range ordering of the cylindrical pores, which is not relevant in this range of diffraction angles. In terms of pore filling, the crystallinity related to pure LiNH$_2$ disappears for pore fillings below 100%. This is in line with good wetting and pore infiltration, because LiNH$_2$ nanoconfined inside the SBA-15 mesopores is not expected to cause any diffraction peaks.

At all pore fillings, a peak unrelated to pure LiNH$_2$ is observed around 38.5°. This peak is broad, indicating small crystallites. Its formation already low pore fillings suggests that it is related to a reaction between LiNH$_2$ and the scaffold at the interface. This is corroborated by its intensity relative to the bulk LiNH$_2$ peak at 35.5°, which decreases with increasing PF. Other peaks unrelated to pure LiNH$_2$ can be observed as well, which are especially clear in the 75% and 100% PF samples. Upon comparing the 75% PF diffraction pattern with the XRD pattern database, a lithium silicon oxide nitride compound with chemical formula Li$_5$SiNO$_3$ seems most likely, as it explains all diffraction peaks at 38.7°, 41.4°, 44.3°, 57.9°, 61.1° and 70.1°. However, these diffraction peaks are not indexed and the quality of this diffraction pattern is low.[80]

These DRIFTS and XRD results show that LiNH$_2$ successfully infiltrates the pores of the SBA-15 scaffold. However, it is also evident that some chemical reaction occurs between the SiO$_2$ scaffold and LiNH$_2$ infiltrate. More extensive characterization with for example nuclear magnetic resonance (NMR) measurements are required to fully understand the exact chemical structure at the LiNH$_2$ and scaffold interface.

5.3.2 Characterization of other LiNH$_2$ nanocomposites

Melt infiltration of LiNH$_2$ was performed with other scaffolds to gain a better understanding on the chemical reaction of LiNH$_2$ and SBA-15. To investigate the effect of surface hydroxyl groups, SBA-15-NH$_2$ was synthesized by grafting the surface of SBA-15. To investigate the influence of the acidity of SBA-15, the basic scaffolds γ-Al$_2$O$_3$ and MgO were used. Boehmite (γ-AlO(OH)) was used to investigate the effect of surface hydroxyl groups as well. It is the uncalcined precursor for γ-Al$_2$O$_3$, and contains more surface hydroxyl groups. An overview of the different scaffolds was given in section 5.2, where the presence of surface hydroxyl or aminopropyl groups was established on all scaffolds.

To verify the success of pore infiltration, DRIFTS measurements were performed on the 130% PF nanocomposites. The results are shown in figure 27. From these graphs, it is clear that the surface hydroxyl group vibrations around 3750 cm^{-1} of γ-Al$_2$O$_3$, γ-AlO(OH) and MgO have disappeared in the nanocomposite spectra. Furthermore, the C–H stretch vibrations around 2900 cm^{-1}, related to aminopropyl surface groups on SBA-15-NH$_2$, have disappeared in the corresponding nanocomposite as well. The disappearance of all surface group vibrations indicates that wetting and complete pore infiltration have occurred in the case of all four nanocomposites.

The N–H stretch vibrations of LiNH$_2$, visible around 3300 cm^{-1}, cause different peak intensities and widths
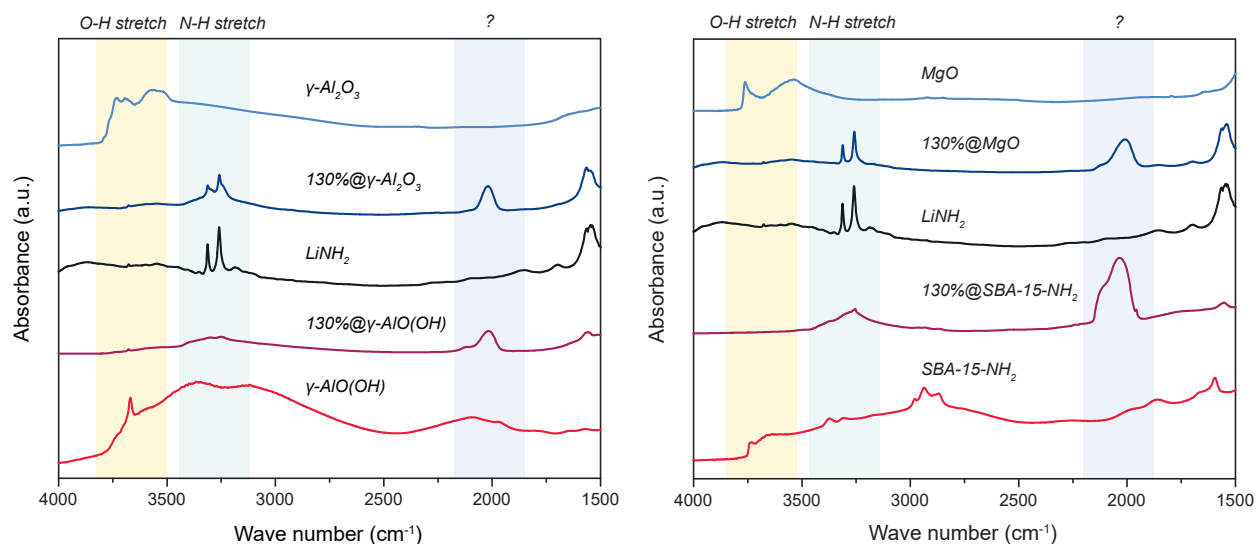
Figure 27: Characterization using DRIFTS of four different scaffolds and their nanocomposites with LiNH$_2$. Note the deviating 200% pore filling of LiNH$_2$ in MgO. It is clear from these results that

for every nanocomposite. In the case of γ-Al$_2$O$_3$ and MgO nanocomposites, these peaks are still clearly present. On the other hand, these peaks are significantly lower in intensity and broader in the case of the γ-AlO(OH) and SBA-15-NH$_2$ nanocomposites. The exact cause for this is as of yet unclear. It cannot be explained by a different amount of LiNH$_2$ present in each sample. Furthermore, it does not seem to be related to the amount of extra-porous LiNH$_2$. It is likely that these peaks are broadened and less intense due to some interaction with the scaffolds.

In the case of SBA-15, a chemical reaction took place between LiNH$_2$ and the scaffold. A similar reaction has taken place in these four nanocomposites, again giving rise to a peak around 2000 cm^{-1}. The intensities and widths of this peak are different for each of the nanocomposites, and in the case of γ-AlO(OH), MgO and SBA-15-NH$_2$ this peak is split in two. In the case of SBA-15-NH$_2$, the higher intensity and increased width are notable, since most surface hydroxyl groups were removed and therefore the reaction between LiNH$_2$ and the scaffold was expected to be suppressed. It is possible that the increased width is caused by the surface modification, which has altered the chemical environment of the surface Si atoms, leading to a larger variety in bond energies and therefore a broader peak. This explanation is in line with a partial reduction of the scaffold and formation of an Si−H bond. In the case of the other scaffolds, partial reduction might have occurred as well. To verify this hypothesis, more extensive characterization using for example NMR measurements are required.

We can conclude that LiNH$_2$ has successfully infiltrated the pores of all scaffolds, but that a reaction between LiNH$_2$ and the scaffolds has taken place as well. This is in line with the XRD patterns of the nanocomposites, which are shown in appendix C.1 and yielded results similar to the SBA-15 nanocomposites. The nature of this reaction and its implications are however still unclear. To establish the effect of melt infiltration on the conductivity of the nanocomposites, EIS measurements were performed.

5.3.3 Conductivity of LiNH$_2$ nanocomposites

The impact of LiNH$_2$ melt infiltration on its conductivity was measured with EIS. The results are shown for all nanocomposites in figure 28A, together with the conductivity of heated LiNH$_2$ for reference. Table 8 summarizes the respective activation energies and conductivities at 130℃ and room temperature.

From these results, it is clear that the conductivity of all nanocomposites increases compared to pure LiNH$_2$, although the differences vary for each nanocomposite. Establishing the effect of melt infiltration on the activation energy of LiNH$_2$ is complicated by the measurements taken in the low sensitivity region of the EIS apparatus ($< 10^{-8}$ S cm^{-1}), which make it difficult to determine the activation energy of heated LiNH$_2$ accurately. Nevertheless, these results show that melt infiltration is a successful method for increasing the
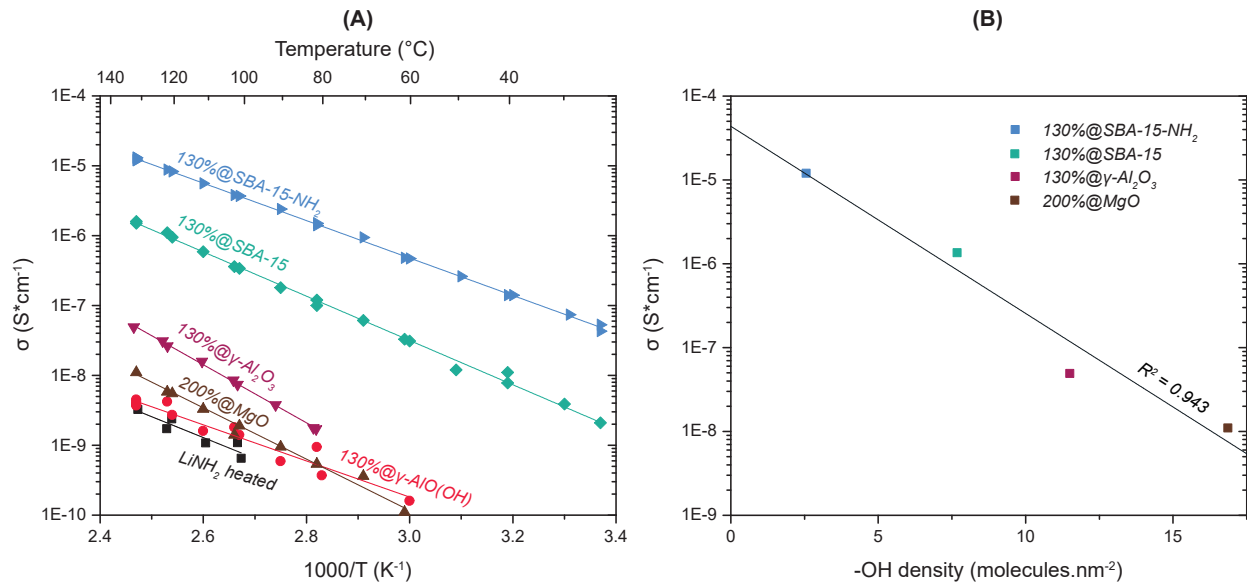
Figure 28: (A) Results of EIS measurements on all LiNH$_2$ nanocomposites. A correlation is visible for use of different scaffolds, where an increase in surface hydroxyl group density leads to a decrease in nanocomposite conductivity. (B) Nanocomposite conductivities at 130℃ as function of the surface hydroxyl group densities, as mentioned by Tamura et al. [28]. Note that this value was not reported for γ-AlO(OH), but is likely higher than that of MgO. The value used for SBA-15-NH$_2$ is one third of that of SBA-15, assuming the replacement of three surface $-$OH groups for one surface $-$NH$_2$ group with a similar chemical effect.

Scaffold	σ_{130} $(\mathrm{S\,cm^{-1}})$	σ_{RT} $(\mathrm{S\,cm^{-1}})$	$\mathbf{E}_A$ **(eV)**
LiNH$_2$ heated	$3.3 * 10^{-9}$	$7.3 * 10^{-12}$	0.59
γ-AlO(OH)	$4.5 * 10^{-9}$	$2.2 * 10^{-11}$	0.51
MgO	$1.1 * 10^{-8}$	$6.1 * 10^{-12}$	0.72
γ-Al$_2$O$_3$	$4.9 * 10^{-8}$	$1.0 * 10^{-11}$	0.82
SBA-15	$1.4 * 10^{-6}$	$2.1 * 10^{-9}$	0.62
SBA-15-NH$_2$	$1.2 * 10^{-5}$	$5.3 * 10^{-8}$	0.53

Table 8: Conductivities at 130℃ and RT, together with activation energies of all LiNH$_2$ nanocomposites.

conductivity of LiNH$_2$.

First of all, it is interesting to note that functionalization of SBA-15 with APTES leads to a conductivity increase of about one order of magnitude in the resulting nanocomposite. Apparently, surface functionalization has improved the interaction between LiNH$_2$ and the scaffold in some way. Possible explanations are a decrease in scaffold porosity, a change from acidic to basic (increase in PZC) upon surface functionalization, and a change in surface groups from hydroxyl to bulkier aminopropyl ligands. The effect of scaffold porosity is discussed in appendix C.2. A change in interaction between the scaffold and LiNH$_2$ is however more likely to explain these results, given the differences that are present in the DRIFTS spectra of the nanocomposites in figures 26A and 27.

To gain information on the effect of the point of zero charge (PZC) of the scaffolds, the conductivity of the SBA-15 and SBA-15-NH$_2$ nanocomposites can be compared to the conductivities of the γ-Al$_2$O$_3$ and MgO nanocomposites. As was mentioned in table 7, SBA-15 is an acidic scaffold, whereas the other three scaffolds are basic. If the increase in PZC upon surface functionalization would explain the corresponding increase in nanocomposite conductivity, the conductivity of the γ-Al$_2$O$_3$ and MgO nanocomposites is expected to be higher than that of SBA-15. In fact, the reverse is true, indicating that some other factor plays a more important role.

It seems likely that the amount of surface groups plays a more important role than their nature in nanocomposite conductivity. More information on this effect is found when comparing the results of the γ-AlO(OH) and γ-Al$_2$O$_3$ nanocomposites. The former has a lower conductivity than the latter one, which might be explained by the higher abundance of surface hydroxyl groups on the uncalcined γ-AlO(OH). It seems likely that these surface hydroxyl groups are detrimental to the conductivity of the nanocomposites. This is in line with the removal of surface hydroxyl groups upon grafting of the SBA-15 surface, together with a higher conductivity in the nanocomposite.

Literature values for the number of surface groups of each of the different scaffolds were summarized in table 7 (aminopropyl instead of hydroxyl groups in the case of SBA-15-NH$_2$). The conductivities of the nanocomposites at 130°C are shown as a function of the surface hydroxyl group density on their surfaces in figure 28B. We chose the conductivities at 130°C because those values could be determined most accurately for each of the nanocomposites. In this figure, indeed an exponential relation between the two quantities is observed, with a decrease in scaffold surface groups resulting in an increase in nanocomposite conductivity. The corresponding formula, with the number of surface groups given by x, is:

$$\log(\sigma) = -4.4 - 0.22x \tag{17}$$

In literature, the density of surface hydroxyl groups was shown to be important for LiBH$_4$ nanocomposites as well.[19] Ngene et al. [19] reported that drying of the scaffolds should remove all reactive surface groups (vicinal silanols) and physisorbed water, which form non-conductive phases near the LiBH$_4$/scaffold interface, but leave less reactive surface groups (free silanols) at the surface. If we compare these findings to the results presented in this work, including the formation of new phases in both DRIFTS and XRD and the nanocomposite conductivities depending on the scaffold surface group densities, it seems that LiNH$_2$ reacts with scaffold surface groups, thereby forming non-conductive phases at the interface that are detrimental to the conductivity of the nanocomposites. These non-conductive phases interfere with the more conductive interface layers that are formed in all nanocomposites, provided that the conductivity of LiNH$_2$ is improved in all nanocomposites. However, by interface engineering the formation of these non-conductive phases can be suppressed. Formula 17 suggests that the maximum attainable conductivity at 130 °C is equal to $10^{-4.4}$ for LiNH$_2$ nanocomposites. Compared to pure LiNH$_2$, this corresponds to a conductivity increase of four orders of magnitude at 130 °C!

6 Conclusions

Melt infiltration is an effective and straightforward method for increasing the conductivity of $LiBH_4$. However, little is known on the applicability of this method to other lithium salts. In this work, we have studied the effect of melt infiltration and nanoconfinement on the ion conduction properties of two Li-based electrolytes for all-solid-state battery applications: $LiNO_3$ and $LiNH_2$.

Melt infiltration of $LiNO_3$ was performed in a variety of scaffolds. With DRIFTS, DSC and XRD, it was demonstrated that $LiNO_3$ was stable during heat treatment and successfully infiltrated the pores of all scaffolds, except for SBA-15. Whether or not infiltration is successful, is determined by the interaction between the infiltrate $LiNO_3$ and the scaffolds. A favourable interaction occurs when acidic sites are present on the scaffold surface. Not only does this interaction have an effect on wettability and pore infiltration, it also affects the conductivity of the nanocomposites. Using EIS measurements, a correlation between the nanocomposite conductivity and the amount of acid sites on the scaffold surfaces was found. Compared to pure $LiNO_3$, this allowed an increase as high as a factor 10^6 in conductivity at room temperature to be obtained for $LiNO_3$ nanoconfined in Nb_2O_5.

Nanocomposites of $LiNH_2$ were prepared using melt infiltration in a wide range of scaffolds. From DRIFTS and XRD measurements, successful melt infiltration of $LiNH_2$ into all scaffold pores was established. However, these techniques also indicated the formation of a new, as of yet unidentified phase at the infiltrate/scaffold interface. A correlation between nanocomposite conductivity and surface group density was found using EIS measurements. These results indicate the formation of non-conductive phases, which interfere with the phases with enhanced mobility at the interface. Minimizing the amount of scaffold surface groups resulted in a conductivity increase of more than a factor 1000 at room temperature for $LiNH_2$ in $SBA-15-NH_2$ nanocomposites, as compared to pure $LiNH_2$.

In this work, the wide applicability of melt infiltration as a means of increasing the conductivity of two lithium salts was demonstrated. Even though both salts have completely different chemistries, increases in conductivity of $10^3 - 10^6$ were attained in both compounds after interface engineering. This demonstrates that this method is versatile and can be applied to a wide range of lithium salts. We can conclude that melt infiltration has an enormous potential for the development of solid electrolytes for all-solid-state Li-based batteries.

7 Outlook

As with every research, many questions remain on the nanocomposites synthesized in this work. Some suggestions on follow-up experiments are listed here.

First of all, the true surface hydroxyl group densities of the scaffolds could be measured, instead of using the values found in literature. Many methods can be employed for this purpose, including reaction with Grignard reagents, thermogravimetric analysis (TGA) and acid-base titrations.[28]

Solid-state nuclear magnetic resonance (NMR) measurements could be performed on these nanocomposites to measure the mobility of Li^+ ions. In this way, a distinction can be made between the mobilities of Li^+ ions at the infiltrate/scaffold interface and in the bulk. Upon doing so, it can be unambiguously demonstrated whether more or less conductive phases are present at the interface. Furthermore, this technique can provide information on the chemical structure which is formed at the interface. Especially in the case of $LiNH_2$ this is of interest, since DRIFTS and XRD measurements alone did not provide sufficient information in this regard.

Other electrochemical characterization methods beside EIS can provide additional information on the nanocomposites synthesized in this work. With cyclic voltammetry (CV), the electrochemical stability window of these electrolytes can be determined. With chronoamperometry (CA), the transference number can be measured, which will give the relative contribution of Li^+ ions to the overall conductivity. In that way, the contributions of mobile anions and possibly electrons can be ruled out.

It would be interesting to verify whether the chemical reaction between $LiNH_2$ and the scaffold surface groups can be suppressed in a way other than minimizing the amount of scaffold surface groups. One possibility is to apply more NH_3 pressure during melt infiltrations. This requires the use of other autoclaves that are suitable for high temperature synthesis.

Porosity in the nanocomposite pellet might have affected the conductivity measurements. To determine its effect, pellets can be pressed at systematically varied pressures. Furthermore, the void fractions can be determined more accurately by using N_2-physisorption measurements.

The acid sites of scaffolds used for $LiNO_3$ melt infiltrations were probed using pyridine FT-IR and NH_3-TPD. Additional information can be gained when the basic sites of all scaffolds are probed as well, for example by using CO_2 FT-IR.[68]

It might be interesting to see if a trend with number of scaffold surface hydroxyl groups on the conductivity of $LiNO_3$ can be found, similar to what was found for $LiNH_2$. However, in this case it seems likely that an increase in surface hydroxyl groups will lead to an increase in conductivity, given the higher conductivities of the $LiNO_3$ in γ-Al_2O_3 and TiO_2 P90 nanocomposites as compared to the SBA-15 one. To better answer this question, melt infiltration of $LiNO_3$ in MgO and AlO(OH) could be performed.

In this work, the effect of scaffold porosity seemed to be minimal as compared to the effects of scaffold surface groups. We have investigated this effect by performing $LiNH_2$ melt infiltrations in a variety of SBA-15 scaffolds. It is also possible to perform ball milling of both lithium salts. This synthesis method can be used independent of scaffold porosity. It will be interesting to see if similar trends can be found with ball milling as compared to melt infiltration.

Lastly, we hope that this research will eventually lead to the implementation of all-solid-state batteries. This requires the testing of solid electrolytes in actual batteries, in terms of for example capacity, cycling stability and compatibility with anode and cathode materials.

Acknowledgements

Appendix

A   List of samples

Sample name	Infiltrate	Scaffold	PF (%)	Sacrificial agent	T (°C)
MP01	$LiNO_3$	MCM-41 (old)	130	-	275
MP02	$LiNO_3$	γ-Al_2O_3	130	-	275
MP03	$LiNO_3$	MCM-41 (old)	130	-	275
MP04	$LiNO_3$	SBA-15	130	-	275
MP05	$LiNO_3$	TiO_2 P90	130	-	275
MP06	$LiNO_3$	Reduced TiO_2	130	-	275
MP07	$LiNO_3$	Reduced TiO_2	170	-	275
MP08	$LiNH_2$	γ-Al_2O_3	130	$SrCl_2$	350
MP09	$LiNH_2$	MCM-41	130	$SrCl_2$	350
MP10	$LiNO_3$	Reduced TiO_2	170	-	275
MP11	$LiNO_3$	Reduced TiO_2	130	-	275
MP12	$LiNH_2$	γ-Al_2O_3	130	$NaNH_2$	390
MP13	$LiNH_2$	SBA-15	130	$NaNH_2$	390
MP14	$LiNH_2$	-	-	$NaNH_2$	410
MP15	$LiNH_2$	γ-Al_2O_3	170	$NaNH_2$	410
MP16	$LiNH_2$	γ-Al_2O_3	200	$NaNH_2$	410
MP17	$LiNH_2$	SBA-15	170	$NaNH_2$	410
MP18	-	γ-Al_2O_3	-	$NaNH_2$	410
MP19	$LiNH_2$	MCM-41	200	$NaNH_2$	410
MP20	$LiNH_2$	-	-	-	410
MP21	$LiNH_2$	SBA-15	200	$NaNH_2$	410
MP22	$LiNH_2$	SBA-15	50	$NaNH_2$	410
MP23	$LiNH_2$	SBA-15	25	$NaNH_2$	410
MP24	$LiNH_2$	γ-Al_2O_3	130	$NaNH_2$	410
MP25	$LiNH_2$	SBA-15	130	$NaNH_2$	410
MP26	$LiNH_2$	γ-Al_2O_3_400°C	200	$NaNH_2$	410
MP27	$LiNO_3$	TiO_2 P90	130	-	275
MP28	$LiNO_3$	γ-Al_2O_3_400°C	130	-	275
MP29	$LiNO_3$	-	-	-	275
MP30	$LiNO_3$	γ-Al_2O_3_600°C	130	-	275
MP31	$LiNH_2$	SBA-15-NH_2 (old)	200	$NaNH_2$	410
MP32	$LiNH_2$	γ-Al_2O_3_200°C	200	$NaNH_2$	410
MP33	$LiNH_2$	γ-Al_2O_3_600°C	200	$NaNH_2$	410
MP34	$LiNO_3$	γ-Al_2O_3_300°C	130	-	275
MP35	$LiNO_3$	γ-Al_2O_3_500°C	130	-	275
MP36	$LiNH_2$	SBA-15-NH_2 (old)	130	$NaNH_2$	410
MP37	$LiNH_2$	SBA-15-CH_3 (old)	200	$NaNH_2$	410
MP38	$LiNH_2$	γ-Al_2O_3_300°C	200	$NaNH_2$	410
MP39	$LiNH_2$	γ-Al_2O_3_500°C	200	$NaNH_2$	410
MP40	$LiNH_2$	MCM-41	200	$NaNH_2$	410
MP41	LiI	$LiNO_3$	10 mol%	-	-
MP42	$LiNO_3$	γ-Al_2O_3_200°C	130	-	275
MP43	LiI	$LiNO_3$	10 mol%	-	275
MP44	$LiNO_3$	Nb_2O_5	130	-	275
MP45	$LiNO_3$	$Nb_3(PO_4)_5$	130	-	275
MP46	LiOH	SBA-15	50	-	480
MP47	LiOH	SBA-15	130	-	480
MP48	LiOH	TiO_2 P90	130	-	480
MP49	$LiNO_3$	γ-Al_2O_3_200°C	130	-	275

Table 9 continued from previous page

Sample name	Infiltrate	Scaffold	PF (%)	Sacrificial agent	T (°C)
MP50	$LiNO_3$	MCM-41	130	-	275
MP51	$LiIO_3$	$LiNO_3$	10 mol%	-	275
MP52	$LiNH_2$	SBA-15_60	130	$NaNH_2$	275
MP53	$LiNH_2$	SBA-15_75	130	$NaNH_2$	275
MP54	$LiNH_2$	SBA-15_90	130	$NaNH_2$	275
MP55	$LiNH_2$	SBA-15_120	130	$NaNH_2$	275
MP56	$LiNO_3$	Nb_2O_5	170	-	275
MP57	$LiNO_3$	γ-Al_2O_3	$\sim$150	-	275
MP58	$LiNO_3$	γ-Al_2O_3	10	-	275
MP59	$LiNO_3$	γ-Al_2O_3	25	-	275
MP60	$LiNO_3$	γ-Al_2O_3	50	-	275
MP61	$LiNO_3$	γ-Al_2O_3	75	-	275
MP62	$LiIO_3$	$LiNO_3$	20 mol%	-	275
MP63	$LiNO_3$	Nb_2O_5	200	-	275
MP64	$LiNO_3$	γ-Al_2O_3	$\sim$150	-	275
MP65	$LiNO_3$	TiO_2 P90	130	-	275
MP66	$LiNO_3$	γ-Al_2O_3	100	-	275
MP67	$LiNO_3$	Nb_2O_5	50	-	275
MP68	$LiNO_3$	$Nb_3(PO_4)_5$	50	-	275
MP69	$LiNO_3$	TiO_2 P90	25	-	275
MP70	LiOH	γ-Al_2O_3	130	-	480
MP71	$LiNH_2$	MCM-41	130	$NaNH_2$	410
MP72	$LiNH_2$	SBA-15	75	$NaNH_2$	410
MP73	$LiNH_2$	SBA-15	100	$NaNH_2$	410
MP74	$LiNH_2$	MgO	130	$NaNH_2$	410
MP75	$LiNH_2$	γ-AlO(OH)	130	$NaNH_2$	410
MP76	$LiNH_2$	MgO	200	$NaNH_2$	410
MP77	$LiNH_2$	CaO	200	$NaNH_2$	410
MP78	$LiNH_2$	SBA-15-NH_2	25	$NaNH_2$	410
MP79	$LiNH_2$	SBA-15-NH_2	130	$NaNH_2$	410
MP80	$LiNO_3$	SBA-15-NH_2	130	-	275
MP81	$LiNO_3$	TiO_2 P90	170	-	275
MP82	$LiNO_3$	γ-AlO(OH)	130	-	275
MP83	$LiNO_3$	MgO	130	-	275

Table 9: Overview of all samples prepared in this work.

B Supporting information LiNO$_3$ nanocomposites

In this section, experimental data complementary to the results discussed in section 4 on LiNO$_3$ nanocomposites are shown.

B.1 Characterization of LiNO$_3$ nanoconfined in γ-Al$_2$O$_3$

In figure 29, DRIFTS and XRD data on LiNO$_3$ in γ-Al$_2$O$_3$ nanocomposites are shown at increasing degrees of pore filling, ranging from 10% to 170%. Only changes in intensity can be observed for each of the different samples, and no changes in peak positions. Therefore, there is no indication on any chemical reaction between LiNO$_3$ and the scaffold surface and successful pore infiltration is confirmed.
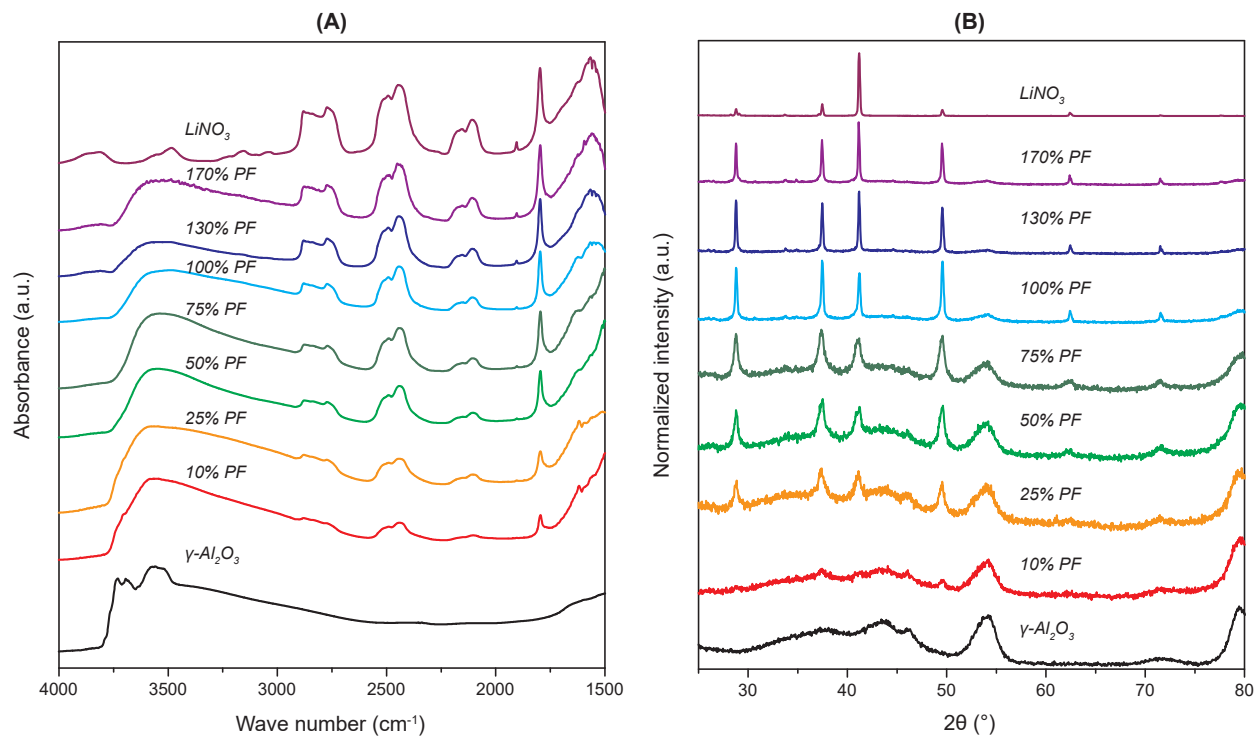

Figure 29: Characterization of LiNO$_3$ nanocomposites in γ-Al$_2$O$_3$ at varying degrees of pore filling using (A) DRIFTS and (B) XRD

B.2 Characterization of LiNO$_3$ nanoconfined in other scaffolds

Lower pore filling samples were synthesized for LiNO$_3$ nanocomposites in combination with TiO$_2$ P90, Nb$_3$(PO$_4$)$_5$ and Nb$_2$O$_5$ scaffolds. Figure 30 shows the characterization results from DRIFTS and XRD mesaurements on these samples. No formation of new peaks can be observed, giving no indication of a chemical reaction between LiNO$_3$ and the scaffold surfaces. Disappearance of surface hydroxyl group vibrations in figure 30A with increasing PF, and disappearance of crystallinity in figure 30 with decreasing PF both indicate successful pore infiltration. Only in the case of TiO$_2$ P90, LiNO$_3$ crystallinity is observed at 25% PF. This can be explained by the macropores of TiO$_2$ P90, which are large enough for LiNO$_3$ crystallites to form.
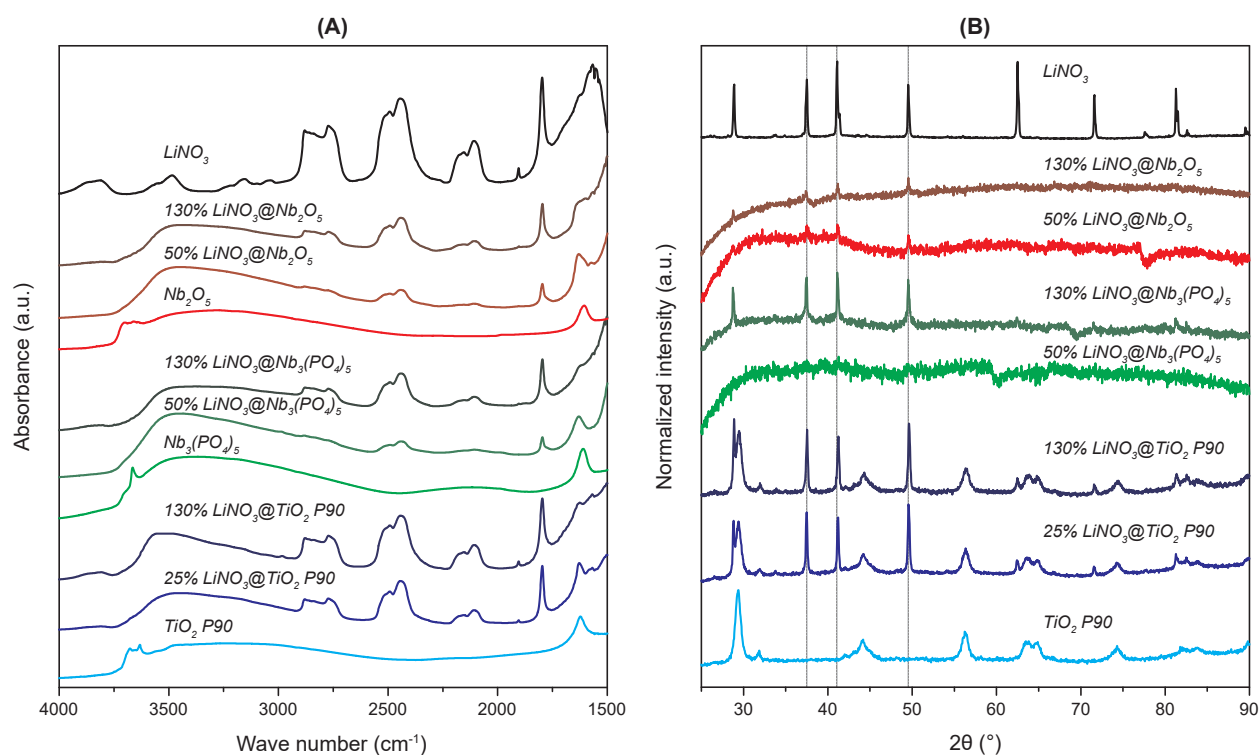

Figure 30: Characterization of LiNO$_3$ nanocomposites in TiO$_2$ P90, Nb$_3$(PO$_4$)$_5$ and Nb$_2$O$_5$ at different degrees of pore filling using (A) DRIFTS and (B) XRD

C Supporting information LiNH₂ nanocomposites

This section provides supporting information on the LiNH$_2$ nanocomposites that were discussed in section 5.

C.1 XRD patterns of LiNH₂ nanocomposites

Figure 31 shows XRD patterns of all LiNH$_2$ nanocomposites which were characterized with DRIFTS and EIS in section 5. The peaks related to pure LiNH$_2$ differ in intensity for each nanocomposite, which is related to the amount of extra-porous LiNH$_2$.
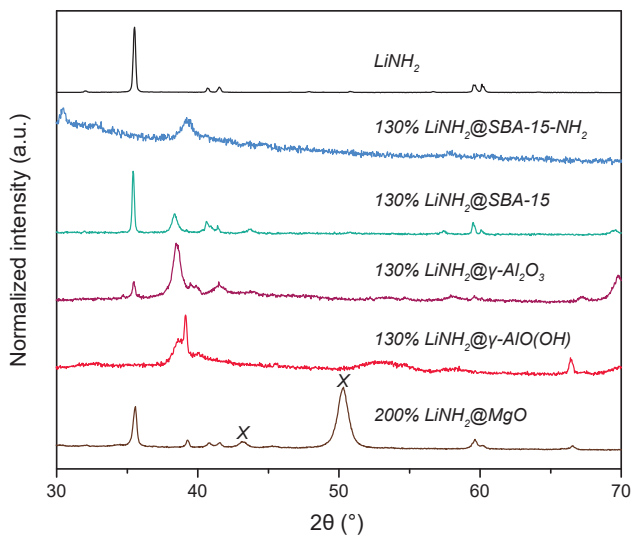

Figure 31: XRD peak patterns for LiNH$_2$ in all scaffolds. X indicates peaks related to crystallinity of MgO.

C.2 Investigation of the effect of scaffold porosity on LiNH$_2$ conductivity

To determine the effect of the porosity of the scaffold on the conductivity of the corresponding LiNH$_2$ nanocomposites, different SBA-15 scaffolds were prepared with systematically varied condensation temperatures of 60 °C, 75 °C, 90 °C and 120 °C. Furthermore, an MCM-41 scaffold was synthesized according to the procedure as described by Cheng et al. [81], in accordance with the procedure of Beck et al. [82].

Firstly, 296 mL deionized water, 40.85 g CTAB and 28 mL TMAOH (25 wt% in H$_2$O) were weighed and added to a 1000 mL round-bottomed flask. The mixture was stirred at 300 rpm in an oil bath of 30 °C. Thereafter, 25.42 g SiO$_2$ (Aerosil380) was added to the mixture, resulting in a gel mixture with aimed molar composition 1.00 SiO$_2$: 0.19 TMAOH : 0.27 CTAB : 40 H$_2$O. Stirring was switched off after 2 hours, while the mixture was left to age at 30 °C for 24 hours. The slurry was allowed to react in a Teflon-lined stainless steel autoclave at 140 °C for 40 hours. The MCM-41 was washed and filtered with distilled water. The solid was dried in static air at 120 °C for 7 hours. Lastly, the MCM-41 was calcined at 550 °C for 12 hours. After drying for 24 hours at 120 °C under vacuum (1 mbar) and magnetic stirring, the final product was obtained and stored under inert Ar atmosphere.

The scaffold porosities were characterized using N$_2$-physisorption. The corresponding pore size distributions are shown in figure 32A, and the other quantities related to porosity are summarized in table 10. It is believed that increasing the condensation temperature in SBA-15 synthesis will increase the mobility of the template surfactants, thereby resulting in larger pore sizes and higher porosity [81]. However, such a clear trend is not observed. For the purpose of this research however, it is sufficient to mention that the various

(A)   **(B)**
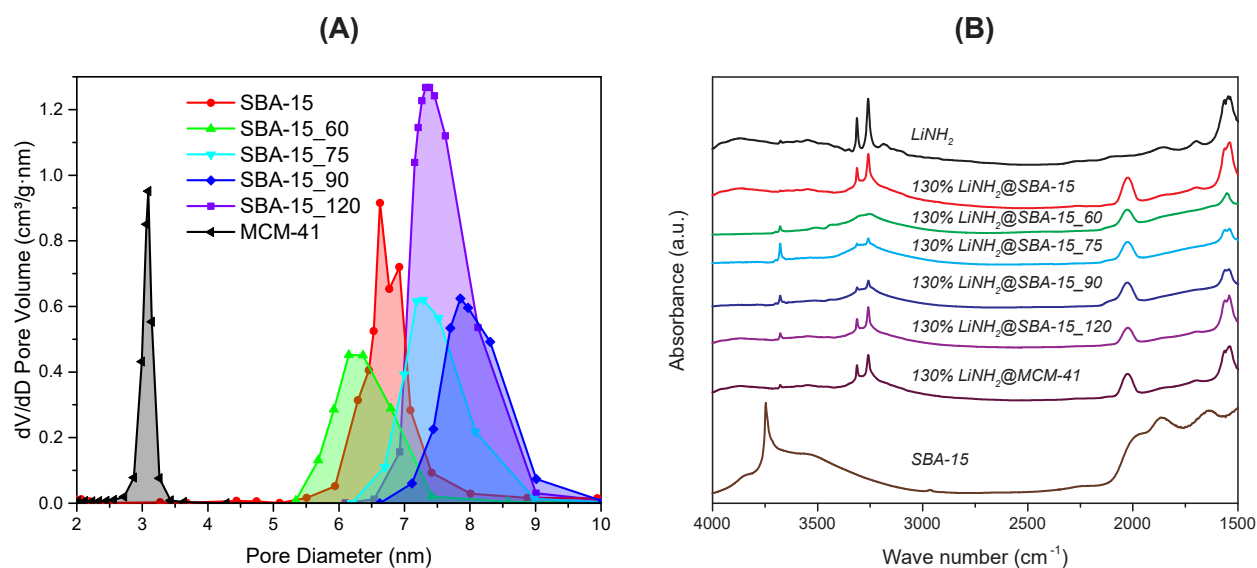
Figure 32: (A) Pore size distributions for various SBA-15 scaffolds. The numbers 60, 75, 90 and 120 indicate their respective systematically varied condensation temperatures. (B) DRIFTS results for LiNH$_2$ nanoconfined in these scaffolds

Scaffold	Pore diameter (nm)	BET surface area (m^2 g^{-1})	Pore volume (cm^3 g^{-1})
SBA-15	6.7	787	1.14
SBA-15_60	6.4	610	0.51
SBA-15_75	7.4	834	0.74
SBA-15_90	8.0	721	0.71
SBA-15_120	7.5	627	1.10
MCM-41	3.1	1089	1.28

Table 10: Tabuled physisorption data on all SiO$_2$ scaffolds used for LiNH$_2$ melt infiltrations

SBA-15 and MCM-41 scaffolds each have different porosities, which allows a systematic investigation on the effect of scaffold porosity on the conductivity of the corresponding LiNH$_2$ nanocomposites.

The 130% LiNH$_2$ in SiO$_2$ nanocomposites were characterized using DRIFTS and XRD. The DRIFTS results are shown in figure 32B. The results are similar to the ones observed before for LiNH$_2$ nanoconfined in SBA-15, as was shown in figure 26. The N–H stretch vibrations around 3300 cm^{-1} broaden due to interactions with the scaffold, and a peak around 2000 cm^{-1} appears, related to a chemical reaction between LiNH$_2$ and the scaffolds. One important difference with the nanocomposite synthesized before is that O–H stretch vibrations can be observed in the nanocomposites at 3750 cm^{-1}. Perhaps no complete pore filling has occurred. Another possibility is that this peak is related to an impurity in the pure LiNH$_2$, since this compound also shows a small peak in this region. Nevertheless, pore filling at least to a considerate amount is suggested by these results.

The XRD patterns in figure 33A show diffraction peaks at equal diffraction angles 2θ as the XRD patterns shown before for LiNH$_2$ in SBA-15. However, clear differences are visible with respect to the intensities of the two peaks at 35.5° and 38.5°. The former peak relates to LiNH$_2$, but decreases in intensity for the SBA-15_75 and SBA-15_90 nanocomposites, and even disappears completely in the case of the SBA-15_60 nanocomposite. This might be related to the pore volume of the scaffolds. SBA-15, SBA-15_120 and MCM-
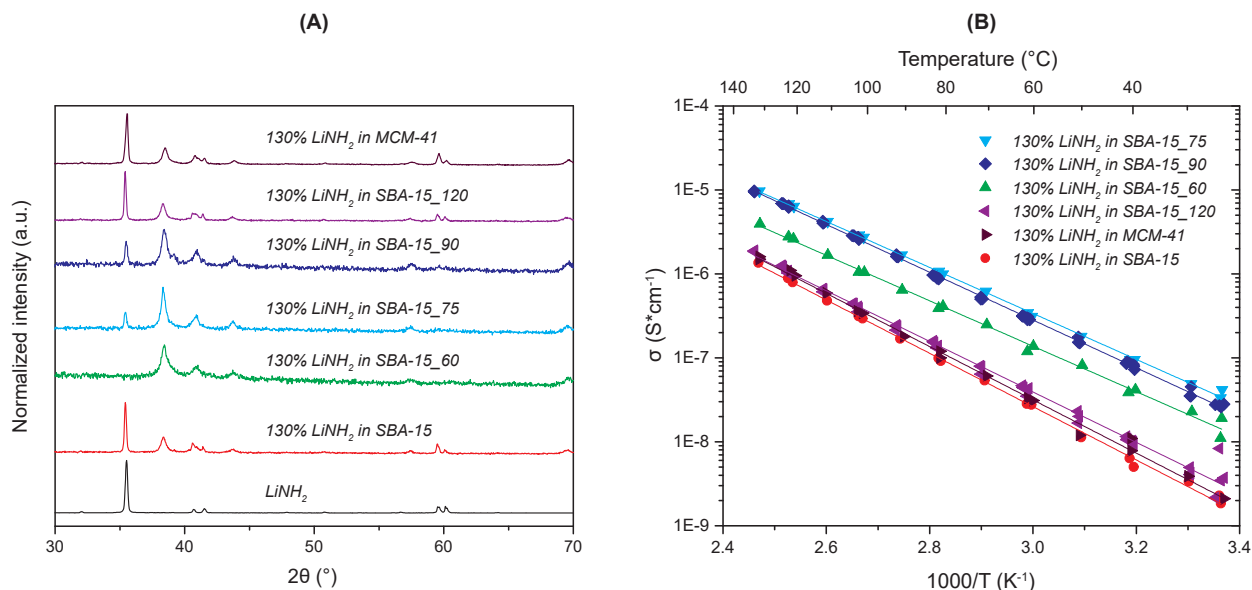

Figure 33: (A) XRD peak patterns for LiNH$_2$ in all SiO$_2$ scaffolds, and (B) their respective conductivities as determined by EIS measurements
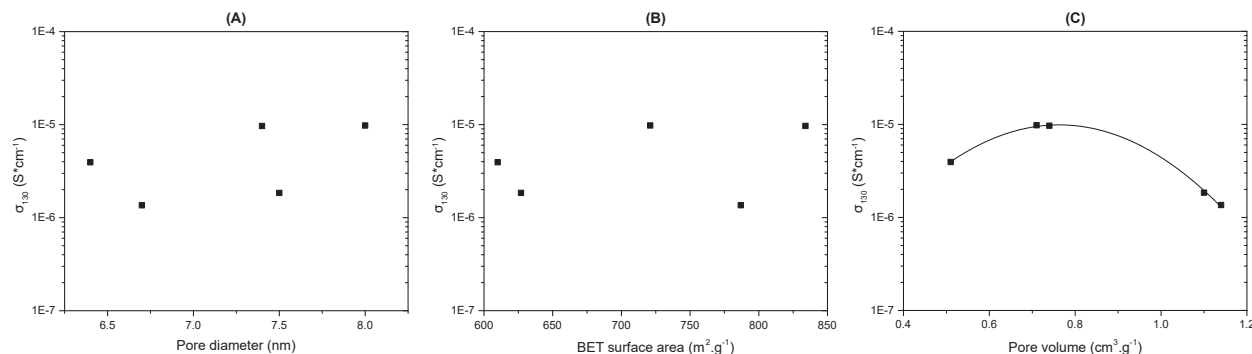

Figure 34: Conductivities of all SBA-15 nanocomposites as function of (A) Pore diameter, (B) BET surface area and (C) Pore volume.

41 have the highest pore volumes, and therefore the most extra-porous LiNH$_2$ and the most intense peaks at 35.5°C. SBA-15_60 has the lowest pore volume, the least extra-porous LiNH$_2$ and therefore the least intensity at 35.5°. Apparently, not enough extra-porous LiNH$_2$ is present in this nanocomposite to give rise to clear diffraction peaks.

The conductivities of the various nanocomposites are shown in figure 33B. Although differences between the various SiO$_2$ nanocomposites can be observed, the different conductivities deviate only within one order of magnitude. Upon comparing these results with the scaffold porosities in table 10, no correlation between the conductivity of the nanocomposites and the pore diameters or surface areas of the scaffolds can be found, as is visualized in figures 34A and 34B. However, an optimum in conductivity can be found with respect to the scaffold pore volumes, as is visualized in figure 34. This is in line with the XRD patterns, which depended on the scaffold pore volume as well. The decrease in conductivity at high pore volumes can be rationalized by a larger amount of less conductive extra-porous LiNH$_2$, since for all scaffolds a 130% pore filling was used. The decrease in conductivity at low pore volumes might be caused by a relatively larger amount of non-conductive SiO$_2$ scaffold with respect to conductive LiNH$_2$.

We can conclude that an optimum ratio between scaffold and LiNH$_2$ is important for obtaining high nanocomposite conductivities.

D   Complementary results

The effect of the drying temperature of the scaffolds on nanocomposite conductivities was investigated by drying γ-Al$_2$O$_3$ at 200 °C, 300 °C, 400 °C, 500 °C and 600 °C.

D.1   Effect of drying temperature of γ-Al$_2$O$_3$ on scaffold acid sites

In figure 35, pyridine FT-IR and NH$_3$-TPD results on γ-Al$_2$O$_3$ are shown. The quantitative results are summarized in table 11. Whereas the nature of acid sites on both scaffolds is similar, their quantities are different. Pyridine FT-IR shows that slightly more Lewis acid sites are present on γ-Al$_2$O$_3$_600, while NH$_3$-TPD shows more acid sites on γ-Al$_2$O$_3$_200, related to Brønsted acid sites that are too weak to interact with pyridine.
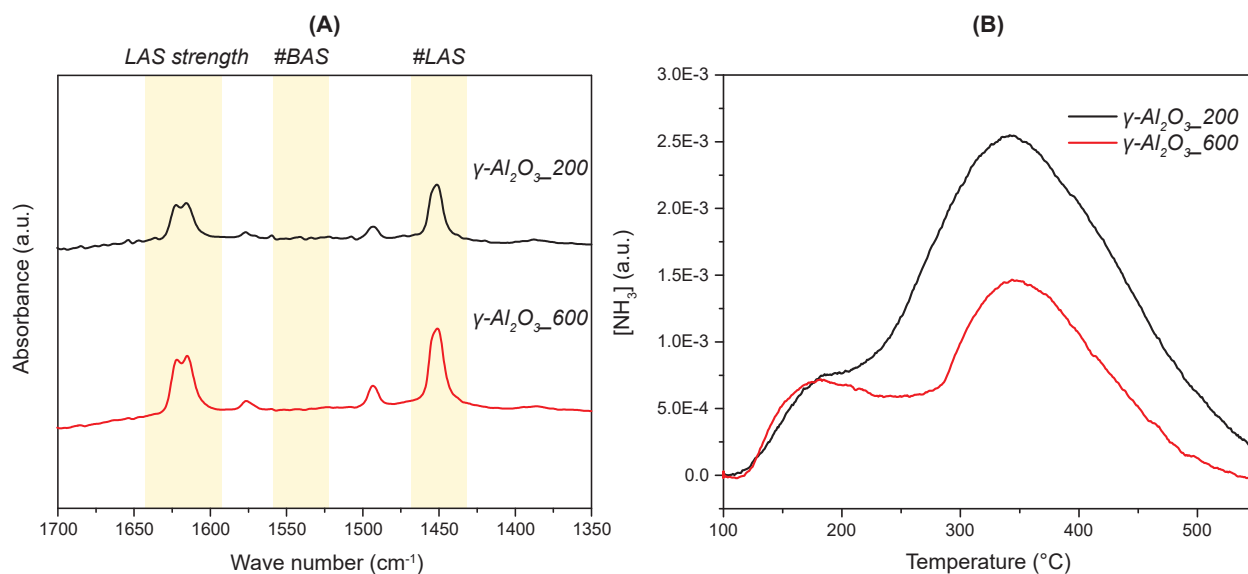

Figure 35: (A) Pyridine FT-IR spectra ranging from $1350 - 1700$ cm^{-1} of γ-Al$_2$O$_3$ scaffolds dried at 200 °C and 600 °C. Absorbance values are corrected for the weight (mg) of sample in each wafer. (B) Results from NH$_3$-TPD measurements on γ-Al$_2$O$_3$ scaffolds dried at 200 °C and 600 °C. The amount of adsorbed NH$_3$ is corrected for the weight of sample (mg) after a baseline subtraction.

Scaffold	Pyridine FT-IR		NH$_3$-TPD		
	BAS (µmol/g)	LAS (µmol/g)	BAS+LAS (µmol/g)	T$_1$ (°C)	T$_2$ (°C)
γ-Al$_2$O$_3$_200	-	49	624	174 ± 23	350 ± 86
γ-Al$_2$O$_3$_600	-	68	348	159 ± 51	358 ± 99

Table 11: Amounts of acid sites on γ-Al$_2$O$_3$ dried at 200 °C and 600 °C, as determined with pyridine FT-IR and NH$_3$-TPD.

D.2   Effect of drying temperature of γ-Al$_2$O$_3$ on nanocomposite conductivities

Conductivities of LiNO$_3$ and LiNH$_2$ nanocomposites in γ-Al$_2$O$_3$ dried at 200 °C, 300 °C, 400 °C, 500 °C and 600 °C are shown in figure 36. Some differences are present between the different scaffolds, but no clear trend can be observed. Perhaps longer drying times would have resulted in larger differences between the scaffolds and therefore larger differences in nanocomposite conductivities.
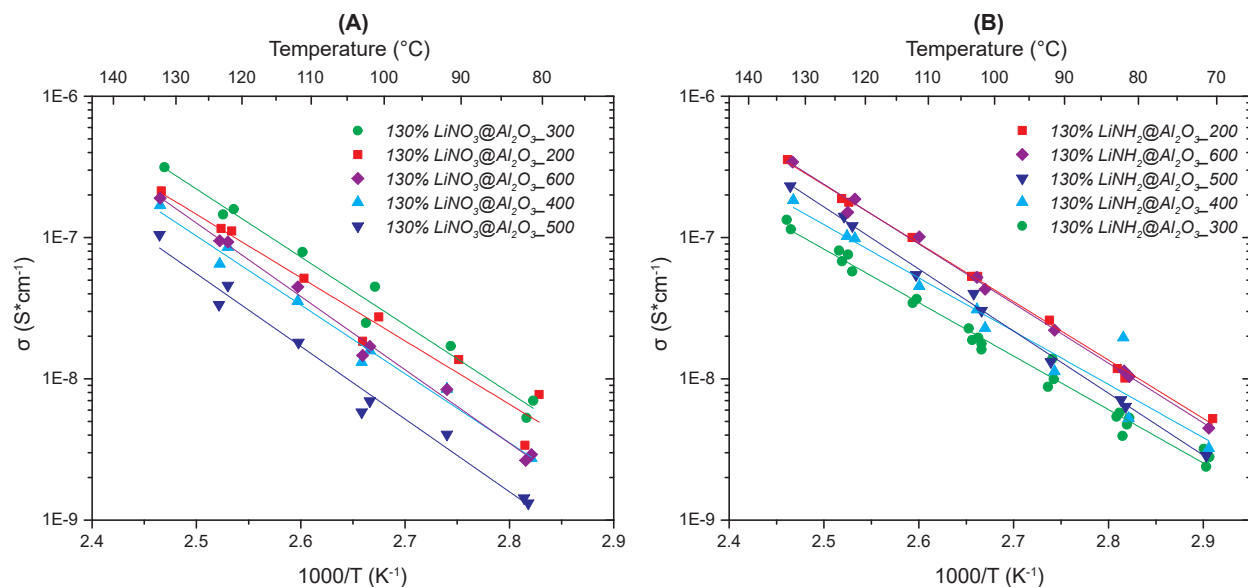

Figure 36: Conductivities of LiNO$_3$ and LiNH$_2$ nanoconfined in γ-Al$_2$O$_3$ dried at 200 °C, 300 °C, 400 °C, 500 °C and 600 °C

References

[1] IEA. *Global EV Outlook 2019*. Tech. rep. Paris, 2019.

[2] Nobel Media AB 2020. *The Nobel Prize in Chemistry 2019*. 2020.

[3] John B. Goodenough and Kyu Sung Park. "The Li-ion rechargeable battery: A perspective". In: *Journal of the American Chemical Society* 135.4 (2013), pp. 1167–1176.

[4] Yong-Sheng Hu. "Batteries: Getting solid". In: *Nature Energy* 1.4 (2016), p. 16042.

[5] Claude Delmas. *Sodium and Sodium-Ion Batteries: 50 Years of Research*. 2018.

[6] Didier Blanchard et al. "Nanoconfined LiBH4 as a fast lithium ion conductor". In: *Advanced Functional Materials* 25.2 (2015), pp. 184–192.

[7] Marlena Uitz et al. "Ion dynamics in solid electrolytes for lithium batteries: Probing jump rates and activation energies through time-domain Li NMR". In: *Journal of Electroceramics* 38.2-4 (2017), pp. 142–156.

[8] Supti Das et al. "All-Solid-State Lithium-Sulfur Battery Based on a Nanoconfined LiBH4 Electrolyte". In: *Journal of The Electrochemical Society* 163.9 (2016), A2029–A2034.

[9] Noriaki Kamaya et al. "A lithium superionic conductor". In: *Nature Materials* 10.9 (2011), pp. 682–686.

[10] Lili Wang et al. "Development and Challenges of Functional Electrolytes for High-Performance LithiumSulfur Batteries". In: *Advanced Functional Materials* 28.38 (2018), pp. 1–23.

[11] Yuki Kato et al. "High-power all-solid-state batteries using sulfide superionic conductors". In: *Nature Energy* 1.4 (2016), pp. 1–7.

[12] Philippe Knauth. *Inorganic solid Li ion conductors: An overview*. 2009.

[13] Koji Yoshida et al. "Fast sodium ionic conduction in Na2B10H10-Na2B12H12 pseudo-binary complex hydride and application to a bulk-type all-solid-state battery". In: *Applied Physics Letters* 110.10 (2017), p. 103901.

[14] Margriet H.W. Verkuijlen et al. "Nanoconfined LiBH4 and enhanced mobility of Li+ and BH4- studied by solid-state NMR". In: *Journal of Physical Chemistry C* 116.42 (2012), pp. 22169–22178.

[15] Motoaki Matsuo et al. "Lithium superionic conduction in lithium borohydride accompanied by structural transition". In: *Applied Physics Letters* 91.22 (2007), pp. 2–5.

[16] Atsushi Unemoto, Motoaki Matsuo, and Shin Ichi Orimo. "Complex hydrides for electrochemical energy storage". In: *Advanced Functional Materials* 24.16 (2014), pp. 2267–2279.

[17] P. E. de Jongh et al. "Complex hydrides as room-temperature solid electrolytes for rechargeable batteries". In: *Applied Physics A* 122.3 (2016), p. 251.

[18] Suwarno et al. "Confinement Effects for Lithium Borohydride: Comparing Silica and Carbon Scaffolds". In: *Journal of Physical Chemistry C* 121.8 (2017), pp. 4197–4205.

[19] Peter Ngene et al. "The influence of silica surface groups on the Li-ion conductivity of LiBH4 /SiO2 nanocomposites". In: *Physical Chemistry Chemical Physics* 21.40 (2019), pp. 22456–22466.

[20] Yigang Yan et al. "A Lithium Amide-Borohydride Solid-State Electrolyte with Lithium-Ion Conductivities Comparable to Liquid Electrolytes". In: *Advanced Energy Materials* 7.19 (2017), pp. 1–7.

[21] Valerio Gulino et al. "Phase Stability and Fast Ion Conductivity in the Hexagonal LiBH4-LiBr-LiCl Solid Solution". In: *Chemistry of Materials* 31.14 (2019), pp. 5133–5144.

[22] S. Breuer et al. "Dispersed Solid Conductors: Fast Interfacial Li-Ion Dynamics in Nanostructured LiF and LiF γ-Al2O3 Composites". In: *Journal of Physical Chemistry C* 123.9 (2019), pp. 5222–5230.

[23] R. C. Agrawal and R. K. Gupta. "Superionic solids: composite electrolyte phase - an overview". In: *Journal of Materials Science* 34.6 (1999), pp. 1131–1162.

[24] Petra E. de Jongh and Tamara M. Eggenhuisen. "Melt Infiltration: an Emerging Technique for the Preparation of Novel Functional Nanostructured Materials". In: *Advanced Materials* 25.46 (2013), pp. 6672–6690.

[25] Stephen Brunauer, D. L. Kantro, and C. H. Weise. "The surface energies of amorphous silica and hydrous amorphous silica". In: *Canadian Journal of Chemistry* 34.10 (1956), pp. 1483–1496.

[26] M Guzmán-Castillo. "The surface energy of quasi-amorphous gamma-alumina calculated from the temperature of the gamma −> alpha transition". In: *Journal of Non-Crystalline Solids* 329.1-3 (2003), pp. 53–56.

References

[27] Syed Salman Shafqat et al. "Development of amino-functionalized silica nanoparticles for efficient and rapid removal of COD from pre-treated palm oil effluent". In: *Journal of Materials Research and Technology* 8.1 (2019), pp. 385–395.

[28] Hiroki Tamura et al. "Mechanism of hydroxylation of metal oxide surfaces". In: *Journal of Colloid and Interface Science* 243.1 (2001), pp. 202–207.

[29] J.A Schwarz, C.T Driscoll, and A.K Bhanot. "The zero point of charge of silicaalumina oxide suspensions". In: *Journal of Colloid and Interface Science* 97.1 (1984), pp. 55–61.

[30] Marek Kosmulski. "pH-dependent surface charging and points of zero charge. IV. Update and new approach". In: *Journal of Colloid and Interface Science* 337.2 (2009), pp. 439–448.

[31] Hengzhong Zhang, Bin Chen, and Jillian F. Banfield. "The size dependence of the surface free energy of titania nanocrystals". In: *Physical Chemistry Chemical Physics* 11.14 (2009), pp. 2553–2558.

[32] Min Zeng. "Influence of TiO2 surface properties on water pollution treatment and photocatalytic activity". In: *Bulletin of the Korean Chemical Society* 34.3 (2013), pp. 953–956.

[33] Toru Murayama et al. "Hydrothermal synthesis of octahedra-based layered niobium oxide and its catalytic activity as a solid acid". In: *Catalysis Science and Technology* 4.12 (2014), pp. 4250–4257.

[34] George Jura and Carl W. Garland. "The Experimental Determination of the Surface Tension of Magnesium Oxide". In: *Journal of the American Chemical Society* 74.23 (1952), pp. 6033–6034.

[35] J H Adair, E Suvaci, and J Sindel. "Surface and Colloid Chemistry". In: *Encyclopedia of Materials: Science and Technology*. Ed. by K H Jürgen Buschow et al. Oxford: Elsevier, 2001, pp. 1–10.

[36] I. Chorkendorff and J. W. Niemantsverdriet. *Concepts of Modern Catalysis and Kinetics*. Wiley, 2013, p. 505.

[37] Christophe Lahousse et al. "Acidic and basic properties of titania-alumina mixed oxides; Active sites for propan-2-ol dehydration". In: *Journal of the Chemical Society, Faraday Transactions* 91.17 (1995), pp. 2907–2912.

[38] Aliya N. Mukhamed'yarova et al. "Influence of the obtaining method on the properties of amorphous aluminum compounds". In: *Coatings* 9.1 (2019).

[39] Akira Taguchi and Ferdi Schüth. *Ordered mesoporous materials in catalysis*. 2005.

[40] Hyung Ik Lee et al. "Morphology-selective synthesis of mesoporous SBA-15 particles over micrometer, submicrometer and nanometer scales". In: *Journal of Materials Chemistry* 20.39 (2010), pp. 8483–8487.

[41] Nazila Masoud et al. "Superior Stability of Au/SiO2 Compared to Au/TiO2 Catalysts for the Selective Hydrogenation of Butadiene". In: *ACS Catalysis* 7.9 (2017), pp. 5594–5603.

[42] Yu-Shan Chi, Hong-Ping Lin, and Chung-Yuan Mou. "CO oxidation over gold nanocatalyst confined in mesoporous silica". In: *Applied Catalysis A: General* 284.1-2 (2005), pp. 199–206.

[43] Laura Munguía-Cortés et al. "APTES-Functionalization of SBA-15 Using Ethanol or Toluene: Textural Characterization and Sorption Performance of Carbon Dioxide". In: *Journal of the Mexican Chemical Society* 61.4 (2018), pp. 273–281.

[44] Xiaoyan Liu et al. "Synthesis of Thermally Stable and Highly Active Bimetallic AuAg Nanoparticles on Inert Supports". In: *Chemistry of Materials* 21.2 (2009), pp. 410–418.

[45] Fengcheng Wu et al. "New short-channel SBA-15 mesoporous silicas functionalized with polyazamacrocyclic ligands for selective capturing of palladium ions in HNO3 media". In: *RSC Advances* 6.71 (2016), pp. 66537–66547.

[46] Akbar Mahdavi-Shakib et al. "Titania surface chemistry and its influence on supported metal catalysts". In: *Polyhedron* 170.0277-5387 (2019), pp. 41–50.

[47] C. Hernández Mejía et al. "Crystalline niobia with tailored porosity as support for cobalt catalysts for the FischerTropsch synthesis". In: *Applied Catalysis A: General* 548.May (2017), pp. 143–149.

[48] Mark E. Orazem and Bernard Tribollet. *Electrochemical Impedance Spectroscopy*. Hoboken, NJ, USA: John Wiley & Sons, Inc., 2008, pp. 108–128.

[49] Su-Il Pyun et al. *Electrochemistry of Insertion Materials for Hydrogen and Lithium*. Monographs in Electrochemistry. Berlin, Heidelberg: Springer Berlin Heidelberg, 2012, p. 22.

[50] Ben Erné. *Lecture notes on Colloidal Analysis Techniques*. Utrecht, 2018.

[51] Digby D. Macdonald. "Reflections on the history of electrochemical impedance spectroscopy". In: *Electrochimica Acta* 51.8-9 (2006), pp. 1376–1388.

[52] Olfa Kanoun. "Impedance spectroscopy advances and future trends: A comprehensive review". In: *Impedance Spectroscopy*. Ed. by Olfa Kanoun. Berlin, Boston: De Gruyter, 2018, pp. 1–22.

[53] Pooria Gill, Tahereh Tohidi Moghadam, and Bijan Ranjbar. "Differential scanning calorimetry techniques: applications in biology and nanoscience." In: *Journal of biomolecular techniques : JBT* 21.4 (2010), pp. 167–93.

[54] Tamara M. Eggenhuisen et al. "Fundamentals of Melt Infiltration for the Preparation of Supported Metal Catalysts. The Case of Co/SiO2 for FischerTropsch Synthesis". In: *Journal of the American Chemical Society* 132.51 (2010), pp. 18318–18325.

[55] Marjolein E. Z. Velthoen et al. "The Multifaceted Role of Methylaluminoxane in Metallocene-Based Olefin Polymerization Catalysis". In: *Macromolecules* 51.2 (2018), pp. 343–355.

[56] Arnaud Travert et al. "Use of pyridine CH(D) vibrations for the study of Lewis acidity of metal oxides". In: *Applied Catalysis A: General* 307.1 (2006), pp. 98–107.

[57] E Parry. "An infrared study of pyridine adsorbed on acidic solids. Characterization of surface acidity". In: *Journal of Catalysis* 2.5 (1963), pp. 371–379.

[58] C.A. Emeis. "Determination of Integrated Molar Extinction Coefficients for Infrared Absorption Bands of Pyridine Adsorbed on Solid Acid Catalysts". In: *Journal of Catalysis* 141.2 (1993), pp. 347–354.

[59] J. Datka and K. Góra-Marek. "IR studies of the formation of ammonia dimers in zeolites TON". In: *Catalysis Today* 114.2-3 (2006), pp. 205–210.

[60] Aline Auroux. *Springer Series in Materials Science 154 Calorimetry and Thermal Methods in Catalysis*. 2013, pp. 81 –98, 132 –162, 175 –186.

[61] Miki Niwa et al. "Temperature-Programmed Desorption of Ammonia with Readsorption Based on the Derived Theoretical Equation". In: *The Journal of Physical Chemistry* 99.21 (1995), pp. 8812–8816.

[62] Lars H. Jepsen et al. "Thermal decomposition of sodium amide, NaNH2 , and sodium amide hydroxide composites, NaNH2 NaOH". In: *Physical Chemistry Chemical Physics* 18.36 (2016), pp. 25257–25264.

[63] A I Zaitsev, N E Shelkova, and B M Mogutnov. "Thermodynamics of Na2O-SiO2 melts". In: *Inorganic Materials* 36.6 (2000), pp. 529–543.

[64] Y I Ostroushko and U S Atomic Energy Commission. Division of Technical Information. *Lithium, Its Chemistry and Technology*. AEC-tr. U.S. Atomic Energy Commission, Division of Technical Information, 1962.

[65] Joseph G Cordaro et al. "Thermodynamic properties of molten nitrate salts". In: *Granada (Spain): SolarPACES* 1.925 (2011), p. 2011.

[66] Xiao Wu, Frank R. Fronczek, and Leslie G. Butler. "Structure of LiNO3: Point Charge Model and Sign of the 7Li Quadrupole Coupling Constant". In: *Inorganic Chemistry* 33.7 (1994), pp. 1363–1365.

[67] Edson R. Leite et al. "Synthesis of niobia nanocrystals with controlled morphology". In: *Journal of Physical Chemistry B* 110.37 (2006), pp. 18088–18090.

[68] Olga V. Manoilova et al. "Surface Acidity and Basicity of La2O3 , LaOCl, and LaCl3 Characterized by IR Spectroscopy, TPD, and DFT Calculations". In: *The Journal of Physical Chemistry B* 108.40 (2004), pp. 15770–15781.

[69] Marjolein E.Z. Velthoen, Sophie Nab, and Bert M. Weckhuysen. "Probing acid sites in solid catalysts with pyridine UV-Vis spectroscopy". In: *Physical Chemistry Chemical Physics* 20.33 (2018), pp. 21647–21659.

[70] Dasari L V K Prasad, N. W. Ashcroft, and Roald Hoffmann. "Lithium amide (LiNH2) under pressure". In: *Journal of Physical Chemistry A* 116.40 (2012), pp. 10027–10036.

[71] Junqing Zhang and Yun Hang Hu. "Decomposition of Lithium Amide and Lithium Imide with and without Anion Promoter". In: *Industrial & Engineering Chemistry Research* 50.13 (2011), pp. 8058–8064.

[72] Peter L. Bramwell et al. "Effect of Pore Confinement of LiNH2 on Ammonia Decomposition Catalysis and the Storage of Hydrogen and Ammonia". In: *The Journal of Physical Chemistry C* 120.48 (2016), pp. 27212–27220.

[73] D. A. Long. "Infrared and Raman characteristic group frequencies. Tables and chartsGeorge Socrates John Wiley and Sons, Ltd, Chichester, Third Edition, 2001. Price £135". In: *Journal of Raman Spectroscopy* 35.10 (2004), pp. 905–905.

[74] J. B. Yang et al. "Crystal and electronic structures of LiNH2". In: *Applied Physics Letters* 88.4 (2006), pp. 1–3.

[75]   Kenji Ohoyama et al. "Revised Crystal Structure Model of Li2NH by Neutron Powder Diffraction". In: *Journal of the Physical Society of Japan* 74.1 (2005), pp. 483–487.

[76]   Xuhang Tong, Hao Zhang, and D. Y. Li. "Effect of Annealing Treatment on Mechanical Properties of Nanocrystalline α-iron: An Atomistic Study". In: *Scientific Reports* 5 (2015), pp. 1–7.

[77]   A.Lee Smith. "Infrared spectra-structure correlations for organosilicon compounds". In: *Spectrochimica Acta* 16.1-2 (1960), pp. 87–105.

[78]   Philip J. Launer. "Infrared analysis of organosilicon compounds: spectra-structure correlations". In: *Silicone Compounds Register and Review* January 2013 (1987), pp. 100–103.

[79]   M Weller et al. *Inorganic Chemistry*. 6th ed. Oxford: OUP Oxford, 2014.

[80]   S Podsiadło. "Formation and thermal decomposition of silicon oxynitride compounds II". In: *Journal of thermal analysis* 32.2 (1987), pp. 445–449.

[81]   Chi Feng Cheng et al. "Controlling the channel diameter of the mesoporous molecular sieve MCM-41". In: *Journal of the Chemical Society - Faraday Transactions* 93.2 (1997), pp. 359–363.

[82]   J. S. Beck et al. "A new family of mesoporous molecular sieves prepared with liquid crystal templates". In: *Journal of the American Chemical Society* 114.27 (1992), pp. 10834–10843.